Time-Optimal Path Planning in the Portugal-Azores-Madeira Ocean Region

by

Clara Dahill

Submitted to the Department of Mechanical Engineering
in partial fulfillment of the requirements for the degree of

Master of Science in Ocean Engineering

at the

MASSACHUSETTS INSTITUTE OF TECHNOLOGY

May 2022

© Massachusetts Institute of Technology 2022. All rights reserved.

Author . . . . . .
Department of Mechanical Engineering
May 6, 2022

Certified by . . . . . .
Pierre F.J. Lermusiaux
Professor of Mechanical Engineering and Ocean Science and Engineering
Thesis Supervisor

Accepted by . . . . . .
Nicolas Hadjiconstantinou
Chairman, Department Committee on Graduate Theses

Time-Optimal Path Planning in the Portugal-Azores-Madeira Ocean Region

by

Clara Dahill

Submitted to the Department of Mechanical Engineering
on May 6, 2022, in partial fulfillment of the
requirements for the degree of
Master of Science in Ocean Engineering

Abstract

For intelligent ocean exploration and sustainable ocean utilization, the need for smart autonomous underwater vehicles (AUVs), surface craft, and small aircraft is rapidly increasing. The challenge of creating time-optimal navigation routes for these vehicles has many applications, including ocean data collection, transportation and distribution of goods, naval operations, search and rescue, detecting marine pollution, ocean cleanup, conservation, and solar-wind-wave energy harvesting, among others. In this thesis, we employ the Massachusetts Institute of Technology - Multidisciplinary Simulation, Estimation, and Assimilation Systems (MIT-MSEAS) time-optimal path planning theory and schemes based on exact Hamilton–Jacobi partial differential equation (PDE) and Level Set methods to predict and study the sensitivity of reachable sets and time-optimal trajectories in the Portugal–Azores–Madeira region of the Northern Atlantic, for several types of missions and autonomous ocean vehicles. Specifically, using the MIT-MSEAS multi-resolution ocean modeling and data assimilation system to provide four-dimensional ocean currents in the region, we compute time-reachable sets and time-optimal paths for several missions, and examine the sensitivity to variations in vehicle type, speed, start time, voyage direction, and operating depths. Our real-data-driven multi-resolution simulation study illustrates how navigational paths vary with these parameters, and how ocean dynamics and variability in the Portuguese ocean regions affect the time optimization, as compared to direct voyages in the absence of any ocean currents. We also highlight effects of the Azores and Madeira archipelagos, differences between surface and bottom path planning, interception routes between vehicles of different speeds, and the utilization of arrival time fields in planning. Results showcase how principled path planning, integrating data-driven multi-resolution ocean modeling with exact reachability theory and numerical schemes, can assess the capabilities of ocean vehicles in the Portugal–Azores–Madeira ocean region, by predicting the fastest travel time, expected range, and optimal headings, for varied types of ocean missions.

Thesis Supervisor: Pierre F.J. Lermusiaux
Title: Professor of Mechanical Engineering and Ocean Science and Engineering

Acknowledgments

I am very grateful to my advisor, Professor Pierre Lermusiaux, for his constant support and mentorship during my academic experience at MIT. Your professional guidance, as well as your compassionate leadership during a challenging academic period, was truly inspiring. I'm thankful for the help and support from our MSEAS family, specifically from Pat and Chris who completed a myriad of ocean forecasts for the Portugal ocean region. Manan and Manny, you are the academic big brothers I needed, and your constant help and encouragement, as well as technical skill building, allowed me to get to where I am.

To the "MechE 2020 Cohort", our close bond during 2 years of remote, hybrid, and in-person learning during a pandemic is what sustained my motivation, and I know you will all thrive in your next chapters.

I am grateful for the professional and financial support from the US Coast Guard, specifically CDR Kate Brown, LTJG Zach Brigham and LTJG Allen McDonald from the Office of Civil Engineering for providing me with the opportunity to pursue an advanced degree while completing my military service. To the Coast Guard Academy professors: Dr. Tarhini, CDR Fleischmann, and LCDR Nakagawa, thank you for teaching me the foundations of civil engineering. Thank you to my engineering mentor, CDR Heering, for inspiring me to pursue a ocean engineering graduate degree.

We are grateful to the MIT Portugal Program (MPP) for research support under a MPP seed project (grant MIT-Port MPP2030-Y3-Seeds) and the Flagship project "Knowledge and Data from the Deep to Space" (K2D – grant MIT-Port Mpp2030-Rsrch-Flag-K2D), each to the Massachusetts Institute of Technology. Thank you to our MIT Portugal collaborators: Profs. D. Hart, J. Leonard, D. Newman, and J. Peraire from MIT, and Prof. J. Tasso de Figueiredo Borges de Sousa from Porto University, and all our other Portuguese colleagues. Agradecido!

Lastly, and most importantly, I would like to thank my sister Aoife and mother Bridget for their unconditional love and support. All of this was only possible because of you!

Contents

1 Introduction **21**

2 Purpose **23**

3 Background **25**

3.1 Environment 25

3.1.1 Ocean region and domains for modeling and planning 25

3.1.2 Ocean Conditions of Portugal 27

3.2 Multi-Resolution Ocean Modeling 30

3.2.1 Modelling Set Up 30

3.2.2 Comparison and Forecast Skill 32

3.2.3 Multiscale Ocean Currents and Circulations at Surface 34

3.2.4 Multiscale Ocean Currents and Circulations at Depth 44

3.3 Autonomous Ocean Vehicles 60

3.3.1 Applications and types of AUVs 60

3.3.2 AUV utilization in the Portugal-Azores-Madeira region 61

3.3.3 AUVs Simulated 63

4 Theory & Methods **67**

4.1 Prior Path Planning Results 67

4.1.1 Path Planning of Autonomous Marine Vessels 67

4.1.2 Path Planning Methods 68

4.2 Time-Optimal Path Planning: Governing Equations and Numerical Schemes . . . 70
4.2.1 Reachability . . . 73
4.2.2 Forward Solve with Level Sets . . . 74
4.2.3 Backtracking . . . 76
4.2.4 Implementation . . . 78

5 Portugal-Azores-Madeira Applications 79
5.1 Summary of Mission Types . . . 79
5.2 Zero Flow-Field . . . 80
5.3 Individual point-to-point . . . 84
5.4 Comparisons within Individual Cases . . . 89
5.4.1 Vehicle Speed . . . 89
5.4.2 Path Direction . . . 92
5.4.3 Start Time . . . 94
5.5 Multi-end points, one start point . . . 97
5.6 Multi-start points, one end point . . . 101
5.7 Bottom paths . . . 104
5.8 Interceptions . . . 111
5.9 Arrival Time Fields . . . 114

6 Conclusion and Future work 119

List of Figures

3-1 Portugal-Azores-Madeira Ocean Region [76] 26

3-2 Locations of interest within domain (Google MyMaps) 27

3-3 General near-surface circulation of the Northern Atlantic Ocean [4] . 28

3-4 Portugal Current System [9] 29

3-5 Bathymetry (m) of Portugal-Azores-Madeira modeling domain 32

3-6 Locations of independent profile-based data of opportunity by type in modeling domain. 32

3-7 MSEAS Predictive Skill: red lines represent data observations, and the black lines represent the model forecasts. The MSEAS-PE model consistently beats persistence for 2 weeks. 33

3-8 Surface velocity in the 4.5 km domain and implicitly nested 1.5 km domain. The magnitude of the velocity is shown in the colorbar, and the direction of the velocity is shown by the vector arrows. 34

3-9 Surface velocity field in magnitude (cm/s) and direction is shown every two days for the duration of our MIT-MSEAS multi-resolution 34 day ocean forecast simulation in the 4.5 km resolution domain. The magnitude of the velocity is shown in the colorbar, and the direction of the velocity is shown by the vector arrows (Figure Continued). . . 36

3-9 Continued: Surface velocity field in magnitude (cm/s) and direction is shown every two days for the duration of our MIT-MSEAS multi-resolution 34 day ocean forecast simulation in the 4.5 km resolution domain. The magnitude of the velocity is shown in the colorbar, and the direction of the velocity is shown by the vector arrows. 37

3-10 Surface velocity field in magnitude (cm/s) and direction is shown every two days for the duration of our MIT-MSEAS multi-resolution 34 day ocean forecast simulation in the 1.5 km resolution domain. The magnitude of the velocity is shown in the colorbar, and the direction of the velocity is shown by the vector arrows (Figure Continued). . . 38

3-10 Continued: Surface velocity field in magnitude (cm/s) and direction is shown every two days for the duration of our MIT-MSEAS multi-resolution 34 day ocean forecast simulation in the 1.5 km resolution domain. The magnitude of the velocity is shown in the colorbar, and the direction of the velocity is shown by the vector arrows. 39

3-11 Surface scaled vorticity in the 4.5 km domain and nested 1.5 km domain. The magnitude of the scaled vorticity is unitless, and is shown in the colorbar. 40

3-12 Surface scaled vorticity field in magnitude every two days for the duration of our MIT-MSEAS multi-resolution 34 day ocean forecast simulation in the 4.5 km resolution domain. The magnitude of the scaled vorticity is unitless, and is shown in the colorbar (Figure Continued). 41

3-12 Continued: Surface scaled vorticity field in magnitude every two days for the duration of our MIT-MSEAS multi-resolution 34 day ocean forecast simulation in the 4.5 km resolution domain. The magnitude of the scaled vorticity is unitless, and is shown in the colorbar. 42

3-13 Surface scaled vorticity field in magnitude every two days for the duration of our MIT-MSEAS multi-resolution 34 day ocean forecast simulation in the 1.5 km resolution domain. The magnitude of the scaled vorticity is unitless, and is shown in the colorbar (Figure Continued). 43

3-13 Continued: Surface scaled vorticity field in magnitude every two days for the duration of our MIT-MSEAS multi-resolution 34 day ocean forecast simulation in the 1.5 km resolution domain. The magnitude of the scaled vorticity is unitless, and is shown in the colorbar. 44

3-14 Location of vertical sections of along-section and across-section velocity (cm/s), as predicted from our data-driven MIT-MSEAS ocean simulations. 45

3-15 Select figures of vertical sections of along-section velocity (cm/s) from Lisbon to Nordeste, Sao Miguel. Velocity magnitude is shown in the colorbar, and the direction is tangent to the slice. 46

3-16 Select figures of vertical sections of across-section velocity (cm/s) from Lisbon to Nordeste, Sao Miguel. Velocity magnitude is shown in the colorbar, and the direction is orthogonal to the slice. 47

3-17 Velocity field at 3000 m of depth in magnitude (cm/s) and direction is shown every two days for the duration of our MIT-MSEAS multi-resolution 34 day ocean forecast simulation in the 4.5 km resolution domain. The magnitude of the velocity is shown in the colorbar, and the direction of the velocity is shown by the vector arrows (Figure Continued). 48

3-17 Continued: Velocity field at 3000 m of depth in magnitude (cm/s) and direction is shown every two days for the duration of our MIT-MSEAS multi-resolution 34 day ocean forecast simulation in the 4.5 km resolution domain. The magnitude of the velocity is shown in the colorbar, and the direction of the velocity is shown by the vector arrows. 49

3-18 Bottom velocity in the 4.5 km domain and nested 1.5 km domain (velocity vectors overlaid on velocity magnitude shown in colorbar). . . . 50

3-19 Bottom velocity field in magnitude (cm/s) and direction is shown every two days for the duration of our MIT-MSEAS multi-resolution 34 day ocean forecast simulation in the 4.5 km resolution domain. The magnitude of the velocity is shown in the colorbar, and the direction of the velocity is shown by the vector arrows (Figure Continued). . . 51

3-19 Continued: Bottom velocity field in magnitude (cm/s) and direction is shown every two days for the duration of our MIT-MSEAS multi-resolution 34 day ocean forecast simulation in the 4.5 km resolution domain. The magnitude of the velocity is shown in the colorbar, and the direction of the velocity is shown by the vector arrows. 52

3-20 Bottom velocity field in magnitude (cm/s) and direction is shown every two days for the duration of our MIT-MSEAS multi-resolution 34 day ocean forecast simulation in the 1.5 km resolution domain. The magnitude of the velocity is shown in the colorbar, and the direction of the velocity is shown by the vector arrows (Figure Continued). . . 53

3-20 Continued: Bottom velocity field in magnitude (cm/s) and direction is shown every two days for the duration of our MIT-MSEAS multi-resolution 34 day ocean forecast simulation in the 1.5 km resolution domain. The magnitude of the velocity is shown in the colorbar, and the direction of the velocity is shown by the vector arrows. 54

3-21 Bottom scaled vorticity in the 4.5 km domain and nested 1.5 km domain 55

3-22 Bottom scaled vorticity field in magnitude every two days for the duration of our MIT-MSEAS multi-resolution 34 day ocean forecast simulation in the 4.5 km resolution domain. The magnitude of the scaled vorticity is unitless, and is shown in the colorbar (Figure Continued). 56

3-22 Continued: Bottom scaled vorticity field in magnitude every two days for the duration of our MIT-MSEAS multi-resolution 34 day ocean forecast simulation in the 4.5 km resolution domain. The magnitude of the scaled vorticity is unitless, and is shown in the colorbar. 57

3-23 Bottom scaled vorticity field in magnitude every two days for the duration of our MIT-MSEAS multi-resolution 34 day ocean forecast simulation in the 1.5 km resolution domain. The magnitude of the scaled vorticity is unitless, and is shown in the colorbar (Figure Continued). 58

3-23 Continued: Bottom scaled vorticity field in magnitude every two days for the duration of our MIT-MSEAS multi-resolution 34 day ocean forecast simulation in the 1.5 km resolution domain. The magnitude of the scaled vorticity is unitless, and is shown in the colorbar. 59
3-24 Autonomous Air and Ocean Vehicles used in Portugal and ocean regions worldwide [19]. 62
3-25 MARES AUV [15] 62
3-26 ISURUS AUV [84] 62
3-27 Surface craft: REMUS 600 [32]. 64
3-28 Bottom craft: MBARI Dorado AUV [73] 64

4-1 RRT from a start point at the center of the domain, through three stages of growth (adapted from [41, 8]) 69
4-2 Uniform discretization of a continuous robot workspace into cells, where the robot can travel to any empty cell on its path from start to finish, avoiding the obstacles represented by the black cells [58] 69
4-3 Visualization of the time-optimal path planning problem (adapted from [68]) 71
4-4 Reachable set, $\mathcal{R}$, Reachability Front, and infinite possible vehicle heading directions (adapted from [66]). 73
4-5 Reachable set, without ocean flows. 75
4-6 Reachable set, with ocean flows. 75
4-7 Level sets, expanding from Lisbon towards final destination of Azores. Thick black curve is reachability front, plotted against scaled vorticity of surface flow. 76
4-8 Level sets from Lisbon to Azores, final destination reached. Thick black curve is reachability front, plotted against scaled vorticity of surface flow. 76
4-9 Backtracking to from final destination to start point to yield optimal path. 77

5-1 Time to reach destination vs vehicle speed for zero flow-field case . . 81

5-2 Zero flow-field case, final reachability Level Set for run from Lisbon to Azores. The plot background is the unitless surface scaled vorticity. The magnitude of the vorticity is shown in the colorbar, and is zero since there is no flow-field present. 82

5-3 Zero flow-field case, final reachability Level Set for run from Lisbon to Azores. The plot background is the unitless surface scaled vorticity. The magnitude of the vorticity is shown in the colorbar, and is zero since there is no flow-field present. 82

5-4 Zero flow vs Ocean Dynamics present, vehicles traveling at 0.5 m/s from the Azores to various end points. The plot background is the unitless surface scaled vorticity. The magnitude of the surface vorticity is shown in the colorbar, and is zero when no ocean dynamics are present. 83

5-5 Evolving level sets of reachability front for AUV travelling at 0.5 m/s from Lisbon to Azores. The plot background is the unitless surface scaled vorticity. The magnitude of the vorticity is shown in the colorbar. 85

5-6 Final level set of reachability front for AUV travelling at 0.5 m/s from Lisbon to Azores. The plot background is the unitless surface scaled vorticity. The magnitude of the vorticity is shown in the colorbar. . . 85

5-7 Final backtracking for AUV travelling at 0.5 m/s from Lisbon to Azores. The plot background is the unitless surface scaled vorticity. The magnitude of the vorticity is shown in the colorbar. 85

5-8 Final time-optimal path for AUV travelling at 0.5 m/s from Lisbon to Azores. The plot background is the unitless surface scaled vorticity. The magnitude of the vorticity is shown in the colorbar. 85

5-9 Vehicle propulsion speed (m/sec) against total time of the path. The Vehicle propulsion speed remains constant throughout journey. 86

5-10 Final time-optimal path for individual point-to-point runs throughout the domain for various start and end points, for AUVs travelling at 0.5 m/s. The plot background is the unitless surface scaled vorticity. The magnitude of the vorticity is shown in the colorbar. 87

5-11 Comparison of time-optimal paths of point-to-point case with flow-field vs zero flow-field case. Vehicles travelling from Lisbon to Azores at 0.5 m/s. The plot background is the unitless surface scaled vorticity. The magnitude of the vorticity is shown in the colorbar, and applies to the case with ocean dynamics present. 88

5-12 Comparison of time-optimal paths of multiple point-to-point case with flow-field vs zero flow-field case for various start and end points, for AUVs travelling at 0.5 m/s. The plot background is the unitless surface scaled vorticity. The magnitude of the vorticity is shown in the colorbar. The time Δ between the ocean dynamics vs no ocean dynamics case will be positive when the no flow-field case is faster. 89

5-13 Speed comparison of time-optimal paths for AUVs travelling from Lisbon to Azores at 0.5 m/s (green) vs 1/5 m/s (pink). The plot background is the unitless surface scaled vorticity. The magnitude of the vorticity is shown in the colorbar. 91

5-14 Direction comparison of time-optimal paths of AUVs travelling from Lisbon to Azores (green) vs Azores to Lisbon (pink) at 0.5 m/s. The plot background is the unitless surface scaled vorticity. The magnitude of the vorticity is shown in the colorbar. 94

5-15 Start time comparison of time-optimal paths for multiple AUVs travelling from Lisbon to Madeira, Day 1 to Day 10 t_i, at 0.5 m/s. The plot background is the unitless surface scaled vorticity. The magnitude of the vorticity is shown in the colorbar. 96

5-16 Final time-optimal paths for case with multiple end points, one common start point at Lisbon, for an AUV travelling 0.5 m/s. The plot background is the unitless surface scaled vorticity. The magnitude of the vorticity shown in the colorbar. 99

5-17 Final time-optimal paths for case with multiple end points, one common start point at Madeira for an AUV travelling 0.5 m/s. The plot background is the unitless surface scaled vorticity. The magnitude of the vorticity shown in the colorbar. 100

5-18 Final time-optimal paths for case with multiple end points, one common start point at Porto for an AUV travelling 0.5 m/s. The plot background is the unitless surface scaled vorticity. The magnitude of the vorticity shown in the colorbar. 101

5-19 Final time-optimal paths for case with multiple start points, one common end point at Lisbon for an AUV travelling 0.5 m/s. The plot background is the unitless surface scaled vorticity. The magnitude of the vorticity shown in the colorbar. 103

5-20 Final time-optimal paths for case with multiple start points, one common end point at Azores for an AUV travelling 0.5 m/s. The plot background is the unitless surface scaled vorticity. The magnitude of the vorticity shown in the colorbar. 104

5-21 Level sets and final backtracking for surface craft travelling from Lisbon to Azores at 0.5 m/s. The plot background is the unitless surface scaled vorticity. The magnitude of the vorticity shown in the colorbar. . . . 106

5-22 Level sets and final backtracking for bottom craft travelling from Lisbon to Azores at 0.5 m/s. The plot background is the unitless bottom scaled vorticity. The magnitude of the vorticity shown in the colorbar. 106

5-23 Final time-optimal path for bottom craft, traveling at 0.5 m/s from Lisbon to Azores. The plot background is the unitless bottom scaled vorticity. The magnitude of the vorticity shown in the colorbar. . . . 107

5-24 Final time-optimal paths for bottom vs surface Craft, travelling from Lisbon to Azores at 0.5 m/s. The plot background is the unitless bottom scaled vorticity. The magnitude of the vorticity shown in the colorbar. 108
5-25 Final time-optimal path for bottom craft, traveling at 0.5 m/s from Madeira to Porto. The plot background is the unitless bottom scaled vorticity. The magnitude of the vorticity shown in the colorbar. . . . 109
5-26 Final time-optimal paths for bottom vs surface craft, travelling from Madeira to Porto at 0.5 m/s. The plot background is the unitless bottom scaled vorticity. The magnitude of the vorticity shown in the colorbar. 110
5-27 Level Sets for time-optimal path outline for target vehicle (vehicle 1). The plot background is the unitless surface scaled vorticity. The magnitude of the vorticity shown in the colorbar. 112
5-28 Final backtracking for target vehicle (vehicle 1). The plot background is the unitless surface scaled vorticity. The magnitude of the vorticity shown in the colorbar. 112
5-29 Final time-optimal path outline for vehicle 1. 112
5-30 Vehicle 1 halfway through executing time-optimal path. 112
5-31 Vehicle 2 level sets begin. The plot background is the unitless surface scaled vorticity. The magnitude of the vorticity shown in the colorbar. 113
5-32 Vehicle 2 level sets continue. The plot background is the unitless surface scaled vorticity. The magnitude of the vorticity shown in the colorbar. 113
5-33 Vehicle 2 level sets end when they intercepted vehicle 1 travelling along its time-optimal path. The plot background is the unitless surface scaled vorticity. The magnitude of the vorticity shown in the colorbar. 113
5-34 Final time-optimal interception paths for vehicle 1 and 2. The plot background is the unitless surface scaled vorticity. The magnitude of the vorticity shown in the colorbar. 113

5-35 All reachable points within time gradient from 0 to 10 days, for a vehicle travelling at 0.5 m/s from São Miguel Island. The plot background is reachable area, measured in days. 115
5-36 Final time-optimal paths to similar points for vehicles travelling at 0.5 m/s from São Miguel Island. The plot background is reachable area, measured in days. 116

List of Tables

3.1 Locations of interest 26

4.1 Notation Definitions 71

4.2 Input Parameters 78

5.1 Zero flow-field case input parameters 81

5.2 Lisbon to Azores run input parameters 84

5.3 0.5 run input parameters 90

5.4 1.5 m/s run input parameters 90

5.5 Lisbon to Azores parameters 93

5.6 Azores to Lisbon parameters 93

5.7 Start time variation run input parameters 95

5.8 Final path total time from varying start time 97

5.9 Multi-end points, Lisbon start point run input parameters 98

5.10 Multi-end points, Madeira start point run input parameters 100

5.11 Multi-end points, Porto start point run input parameters 101

5.12 Multi-start points, Lisbon end point run input parameters 102

5.13 Multi-start points, Azores end point run input parameters 104

5.14 Input parameters for bottom vehicle, traveling at 0.5 m/s from Lisbon to Azores 105

5.15 Input parameters for bottom vehicle, traveling at 0.5 m/s from Madeira to Porto 109

Chapter 1

Introduction

For intelligent ocean exploration and sustainable ocean utilization, the need for smart autonomous underwater vehicles, surface craft, and small aircrafts is rapidly increasing. Applications include scientific studies, solar-wind-wave energy harvesting, transportation and distribution of goods, naval operations, security, acoustic surveillance, communication, search and rescue, detecting marine pollution, ocean cleanup, conservation, fisheries, aquaculture, mining, and monitoring and forecasting [52]. Designing optimal paths leads to cost savings, longer operational time, and environmental protection [68, 51, 54, 7, 83, 22]. Autonomous vehicles and unmanned sea surface craft (such as propelled underwater vehicles, AUVs, ocean gliders, solar-vehicles, wave-gliders, floats, etc.) operate with minimal human interaction, as there is little to no human supervision, which makes path planning critical to their function. Widely applicable in long-term mission scenarios that use exploitation and/or exploration with sensing such as the ones previously mentioned, these autonomous underwater and ocean surface vehicles can increase their range and decrease their energy need by following time-optimal paths. The goal of this thesis is to apply optimal planning theory and methodology to simulate and study the time-optimality of surface craft and underwater vehicles operating in the Portugal-Azores-Madeira ocean region. Specifically, we combine realistic data-assimilative ocean modeling [30, 28] with the partial-differential-equations (PDEs) for exact reachability and path planning [66, 60, 21].

Since the need for AUV use is increasing, this research is important to define and exercise the path planning piece of the AUV operation puzzle. In marine operations, ocean and weather sensing and forecasting should be used as inputs to autonomous missions. For long-term missions, long endurance and low energy cost are crucial requirements. Specifically, there is a need to increase the capability of vehicles to operate for long periods at sea, by planning efficient time-optimal routes, which leads to conserving fuel by designing efficient paths that lead to cost savings, longer operational time, and environmental protection [54].

A specific objective of this thesis is to investigate the sensitivity of quantitative time-optimal planning to the type of mission and the properties of vehicles that operate in realistic ocean environments. It applies the fundamental partial differential equation (PDE) path planning theory to data-driven ocean applications relevant to Portugal [74], for a scope of planning cases and vehicle parameters.

Traditionally, path planning has been developed for robots in static environments. However, the ocean contains dynamic currents, waves, and winds that significantly affect the motion of many vehicles. Traditional algorithms then provide incorrect solutions or are too expensive for real-time use. In the past years, our Multidisciplinary Simulation, Estimation, and Assimilation Systems (MSEAS) lab has derived and applied new theory and level-set methods that solve for the time-optimal paths in such dynamic environments exactly and efficiently [66, 60, 55, 96, 67]. The main method is based on Hamilton-Jacobi equations that govern the reachability front for vehicles in strong dynamic flows [21]. From this reachability front, we backtrack to calculate the final time-optimal path solution. This thesis will discuss how the use of time-optimal path planning methodology is implemented in the Portugal region for a scope of planning cases and vehicle parameters.

Chapter 2

Purpose

The purpose of this thesis is to explore the sensitivity of time-optimal path planning in the Portugal ocean region, for a range of mission types, vehicle types, vehicle operating parameters, and local dynamics and geography of the region. There are many applications for autonomous marine vehicles in the Portugal region, with a myriad of islands used for scientific, economic, and cultural exchange [19, 84, 15, 4]. Designing time-optimal paths leads to cost savings, longer operational time, and environmental protection. It also increases the ability of these autonomous ocean vehicles to successfully complete long endurance operations and missions within their time, range, and power budgets. In the longer term, the motivation of this work is to develop and apply our optimal planning theory and methodology to increase the efficiency of surface craft and underwater vehicles operating in the dynamic conditions in the region.

This thesis is part of two research programs sponsored by MIT Portugal, a seed project and the K2D project. For the present thesis, we emphasize the following specific objectives, as part of these two projects:

1. Further develop and apply the MSEAS exact PDE-based path planning theory and data-driven ocean modeling methodology to optimize the efficiency and endurance of ocean autonomous vehicles.

2. Set-up and validate multi-resolution 4D ocean modeling and forecasting in the

domain of the Portuguese Eastern North Atlantic, which encompasses the Portugal coast and the Madeira and Azores archipelago islands.

3. Implement our rigorous theory and schemes for time-optimal path planning and risk minimization under realistic ocean conditions, apply schemes for surface and bottom craft autonomous vehicles, and compare results based on vehicle speed, travel direction, and start time.

4. Study the dynamic ocean flow-field effects on different vehicle journeys, to include travel from individual point-to-point, multiple start points and a common end point, and multiple end points and a common start point, as well as comparing these paths to the direct, zero flow-field path trajectory.

5. Predict interception courses and minimum arrival times for all surface points in a dynamic flow-field containing land masses.

In what follows, we will review the known ocean dynamics and circulation features of the region, the utilization of AUVs and other ocean platforms in the region, and a description of our MSEAS multi-resolution ocean modeling. We then review existing path planning theories, and our theory and methodology for time-optimal path planning using level set methods. We then apply our methodology for different missions and vehicles in the Portugal-Azores-Madeira region.

Chapter 3

Background

This chapter discusses the ocean conditions of the region, the importance of AUVs for many key areas and their use in Portugal, and the ocean modelling system that we employed to model the ocean circulation and currents in the region.

3.1 Environment

We now describe the geography, physical features, and processes occurring in the Portugal-Azores-Madeira region, as well as the properties of our ocean modeling system. We emphasize the features of the ocean domain that are key areas for path planning.

3.1.1 Ocean region and domains for modeling and planning

This research focuses on the Eastern Northeastern Atlantic Ocean region off the coast of Portugal, which contains the archipelago islands of Madeira and Azores. The domain area is 2,700 km x 1,600 km, ranging in latitude from 28.88° N to 43.39° N, and in longitude from 6.00°W to 35.93°W. Figure 3-1 shows a chart of the domain, and Figure 3-2 shows a map with the main locations of interest that will be used for creating optimal paths.

Table 3.1 shows all of the important locations that will be used as start and

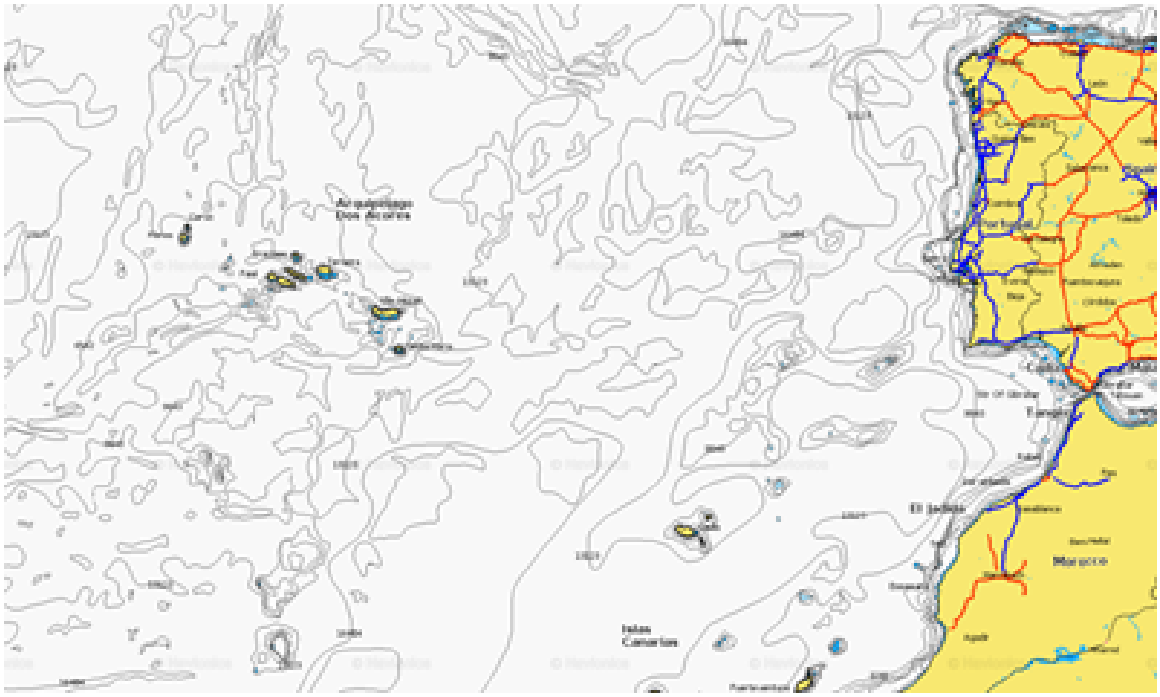

Figure 3-1: Portugal-Azores-Madeira Ocean Region [76]

destinations points for path planning. The locations of these points, also shown in Figure 3-2, are important because they are directly offshore from major destinations within the Portugal ocean region, to include the major islands of Madeira and Azores, the main ports of Lisbon and Porto, and a mid-domain point in the ocean to capture far offshore activity. These specific points would be practical for long range AUV and other ocean platforms operating between major ports, as well as coastal sampling or monitoring close to shore where a research vessel could launch, monitor, and collect the AUVs.

Point	Location
Lisbon	38.0°N 10.0°W
Porto	41.0°N 9.0°W
Azores	37.5°N 24.0°W
Madeira	33.5°N 17.0°W
Ocean (mid-domain)	40.0°N 18.0°W

Table 3.1: Locations of interest

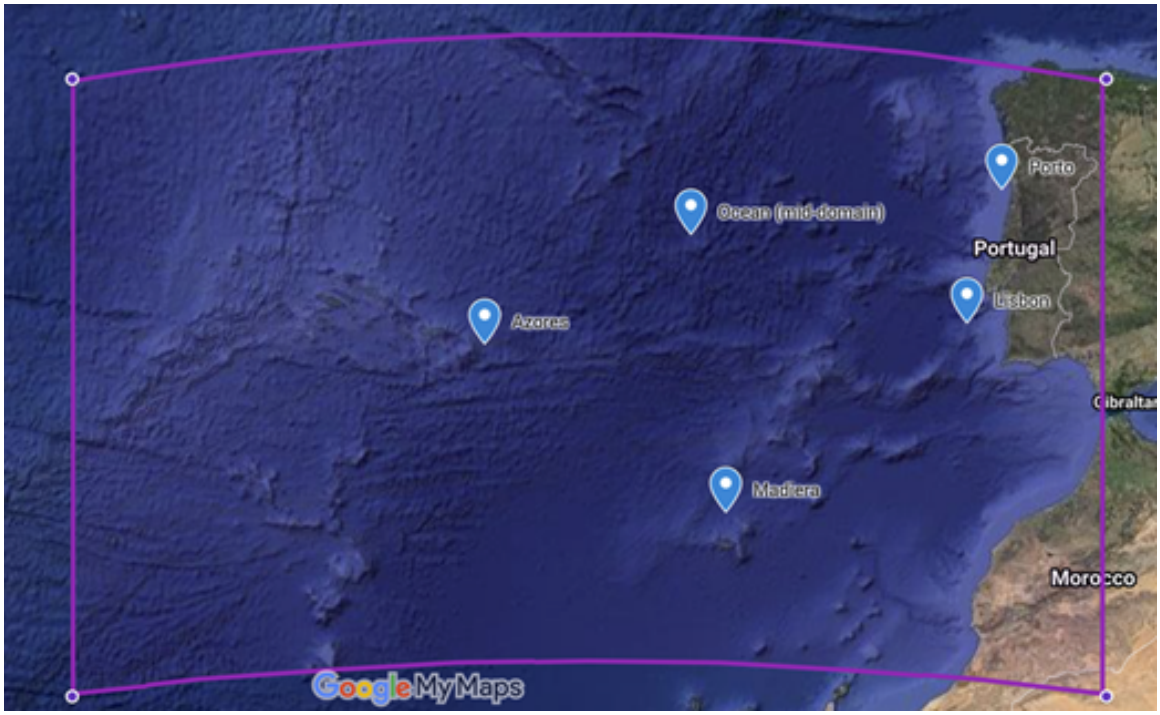

Figure 3-2: Locations of interest within domain (Google MyMaps)

3.1.2 Ocean Conditions of Portugal

The major ocean currents in this domain come from a weak current system convergence in the Northeastern Atlantic Ocean [10]. The Gulf Stream feeds into the Northern Atlantic subtropical gyre, which splits off in its eastern reach into currents called the *Canary* and *Azores* currents. These currents travel west to east, as well as the *Portugal Current System*, which travels along the Atlantic coast of the Iberian Peninsula, which contains Spain and Portugal. The Canary current is fed by the Azores current, as they both branch off from the clockwise Northern Atlantic gyre [4]. Figure 3-3 shows the circulation of these currents.

The Portugal Current System contains both the Portugal Current and the Portugal Coastal Countercurrent. The Portugal Current travels south from continental Portugal towards the Azores archipelago. The Portugal Coastal Countercurrent travels poleward along the west and north coasts of the Iberian Peninsula [70].

The western coast of the Iberian Peninsula experiences upwelling that affects these currents seasonally. Seasonal upwelling cools the coastal waters between the

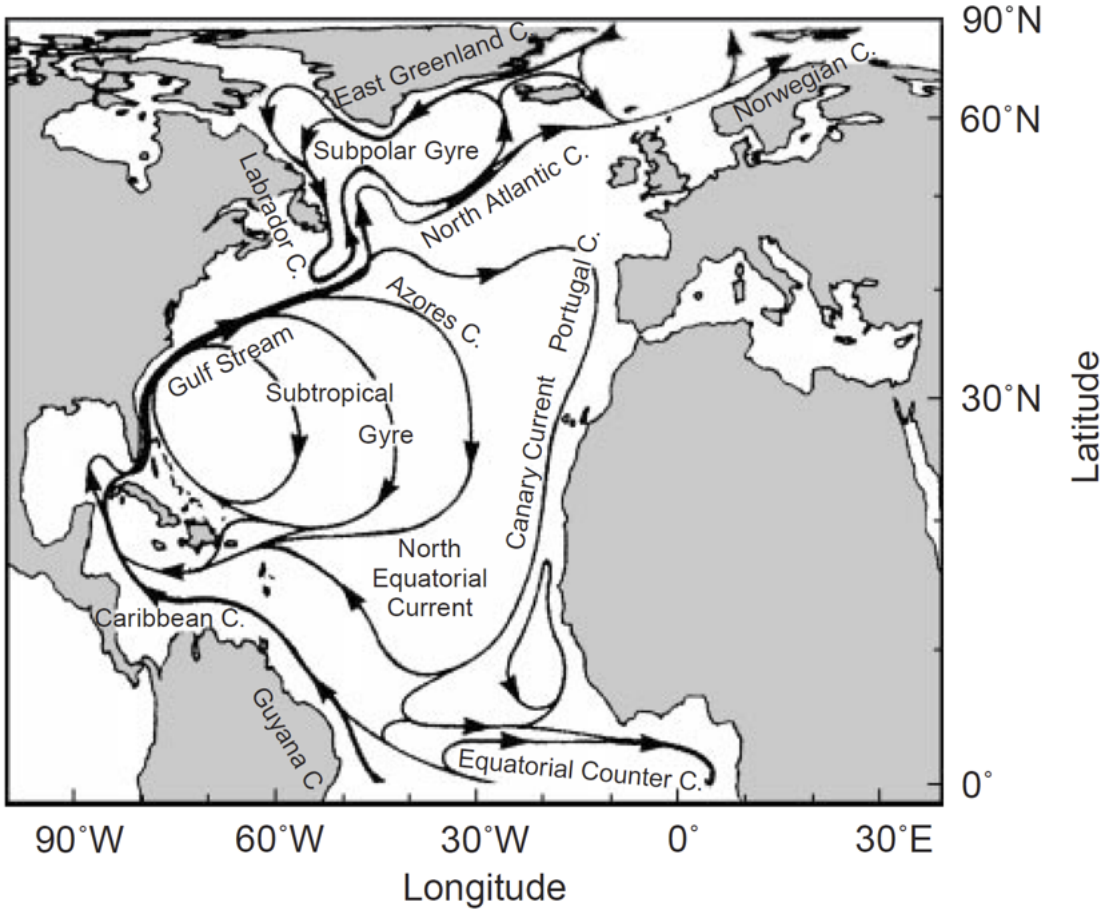

Figure 3-3: General near-surface circulation of the Northern Atlantic Ocean [4]

late spring and early fall [6]. During this time, the northeast trade winds flow over the subtropical eastern boundary currents, creating Ekman transport in the offshore surface layer, and creating alongshore upwelling. This upwelling also leads to equatorward flow that dominates the continental shelf and slope along the Iberian Peninsula [4]. This upwelling creates the poleward subsurface flow that makes up the Portugal Coastal Countercurrent. In Figure 3-4, the red arrows show the Portugal Current System along the Iberian Peninsula Coast during the spring, when upwelling begins [4].

In this upwelling region within the continental shelf and the coast, the undercurrent has a vertical extent of several hundred meters, where current meters have indicated that most of the water column indeed flows poleward [13]. Interaction of

this poleward current with the coastal topography also leads to flow separation and eddy shedding along the coast [81]. Mediterranean water will also flow north from the Strait of Gibraltar along the continental slope to form part of this undercurrent, extending from 1,500 m to the ocean bottom of the surface mixed layer [13].

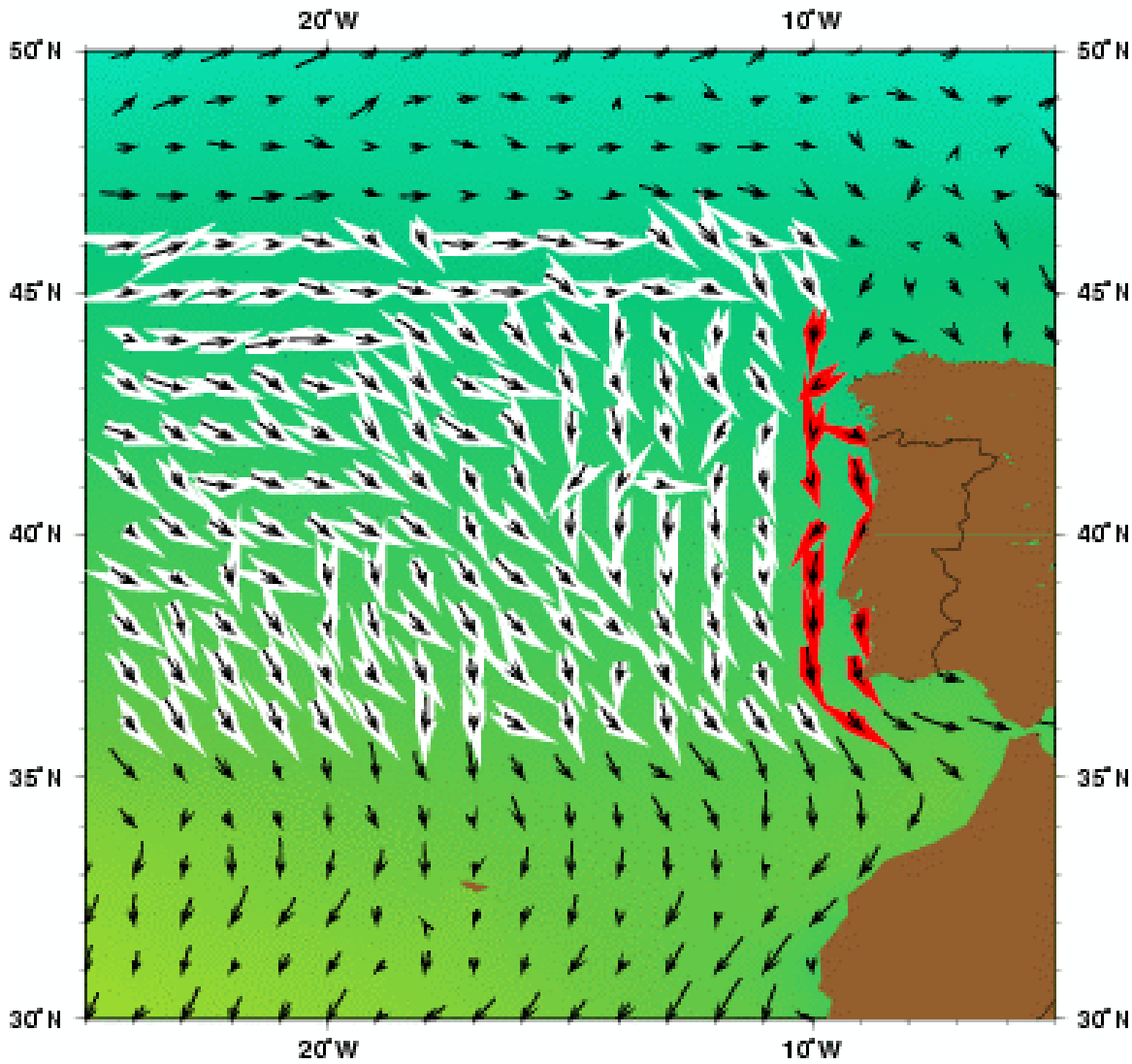

Figure 3-4: Portugal Current System [9]

These seasonal changes in the currents from upwelling are caused by changes in wind patterns throughout the year. The Azores High, a semi-permanent subtropical high-pressure system, migrates seasonally and will have a 1 mbar difference from mainland Portugal in the winter, and an 8 mbar difference in the summer. In the

summer, this creates dominant north and northwesterly winds, which compound with the upwelling of colder, deep ocean water along the continental shelf. In the winter, the north/northwesterly wind weakens and can even reverse, leading to a reversal of the surface flow [13].

3.2 Multi-Resolution Ocean Modeling

We now describe the ocean modeling system and simulations used to characterize the dynamic ocean circulations that we employed in our time-optimal path planning study.

3.2.1 Modelling Set Up

To model the dynamic ocean environment, we employ the MIT Multidisciplinary Simulation Estimation and Assimilation System (MSEAS) Primitive-Equation model [30, 50, 28]. This is an advanced ocean dynamics and real-time modeling and prediction software system. It solves the nonlinear free-surface hydrostatic primitive-equations (PE) and provides a multi-scale flow, temperature, and salinity fields to study and quantify tidal-to-mesoscale processes in any regional ocean domains [30, 28]. Its modelling capabilities include telescoping domains interconnected by implicit two-way nesting for hydrostatic PE dynamics, second order structured finite volumes, and a high-order finite element code on unstructured grids for non-hydrostatic processes [30, 79, 103, 104].

This MSEAS software has been used and validated for fundamental research and for realistic simulations in varied regions throughout the ocean [56, 77, 36, 27, 26, 85, 14, 95], and has been adapted in individual present work to include initialization schemes [28], fast-marching coastal objective analysis [1], advanced data assimilation [90, 44, 45, 88, 91, 49, 48, 5, 89, 47, 29, 92, 93, 63, 62], nested data-assimilative tidal prediction and inversion [57], and subgrid-scale models [46].

This modelling system software was set up for time-optimal path planning in the Portugal ocean region. The ocean fields covered the ocean region spanning 2700 km

× 1600 km, aligned to contain the coastline of Portugal, the Azores and Madeira archipelagos, the northwestern coast of Africa, and the Mediterranean outflow at the Strait of Gibraltar, as shown in Figure 3-1. The simulated fields were time-dependent, and spanned a 34-day hindcast from 1200 UTC 17 March 2019 to 1200 UTC April 20 2019. The MSEAS PE model provides a realistic tidal-to-mesoscale multiresolution simulation with complex geometries and varied interactions, which can be used to predict the multiscale ocean flow dynamics of the domain [60, 30, 28, 36].

We set up and developed implicit two-way nested ocean simulations, with an overall horizontal grid resolution of 4.5 km for the larger domain, and smaller nested domains of horizontal resolution 1.5 km for the areas of interest, and a half kilometer domain on the coast between the cities of Porto and Lisbon, as shown in Figure 3-5 below. These telescoping modelling domains employ high-resolution vertical bathymetry and a vertical resolution of 100 optimized vertical levels. The barotropic tides are based on the TPXO8-Atlas tidal forcing [24], and adjusted for our higher resolution bathymetry, as well as Rayleigh bottom and coastal friction [57]. Tidal forcing is also adjusted for specific quadratic bottom drag, where the drag coefficient depends on the thickness of the bottom level, which is a function of topography [34, 31]. Temperature and salinity based feature models were utilized to model the continental shelf and Mediterranean outflow [45, 26]. Atmospheric forcing was applied at the free surface and was obtained from the 1/5 ° NCEP Climate Forecast System atmospheric fluxes [75]. The initial and open boundary conditions for the 4.5 km domain were scaled from the 1/12 ° HYbrid Coordinate Ocean Model (HYCOM) data [16], and data assimilation used for optimization for higher resolution bathymetry and coastlines [28]. The boundary conditions for the smaller 1.5 and 0.5 km nested domains were derived from the 4.5 km domain.

From our high-resolution MIT-MSEAS simulations, we provide 4-dimensional (longitude, latitude, depth, time) ocean fields that include currents, temperature, salinity, and biogeochemical field simulations incorporating the higher resolution domain around the Portuguese coast.

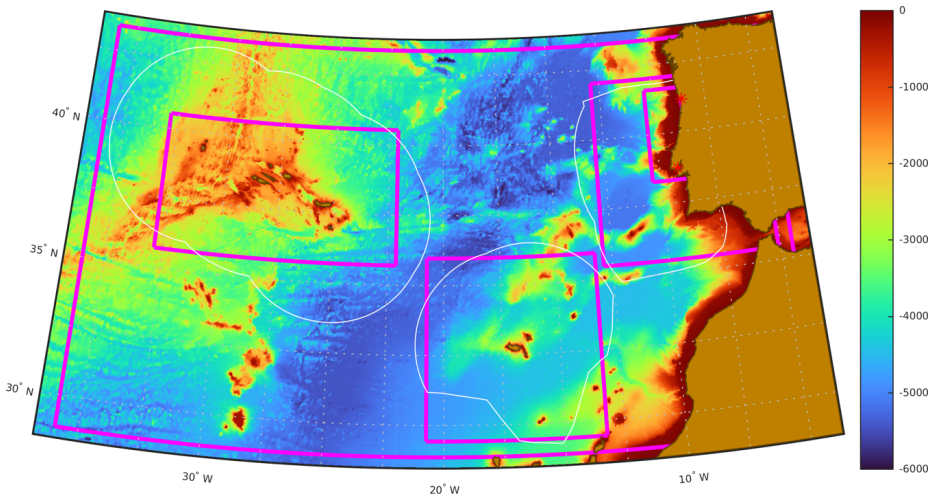

Figure 3-5: Bathymetry (m) of Portugal-Azores-Madeira modeling domain

3.2.2 Comparison and Forecast Skill

The MSEAS ocean simulations were hindcast simulations, that is, forecast simulations completed for past dates. These simulations were compared to ocean observations, and validated by comparing against independent profile-based data sets from ARGO floats, BioGeoARGO floats, and glider data, the locations of which are shown in Figure 3-6 below. This allowed us to evaluate the predictive skill of our multi-resolution ocean model system set-up.

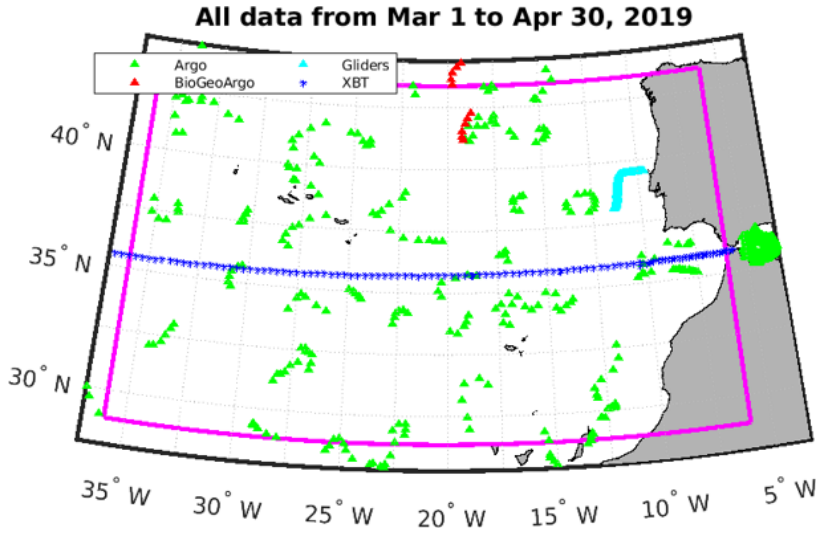

Figure 3-6: Locations of independent profile-based data of opportunity by type in modeling domain.

In Figure 3-7, we compare persistence forecast (the imaginary forecast that keeps the initial conditions constant to forecast out) to our MSEAS-PE modeling system predictions. Temperature (top row) and salinity (bottom row) hindcast fields and the original HYCOM model fields are compared to independent profile data. The results show a 20% improvement for a 7-day forecast, and an 8% improvement for a 14-day forecast. Since this forecast was completed for past dates using our MSEAS-PE modeling system, it is a hindcast. The results highlight that our MIT-MSEAS simulations beat persistence for these two weeks in the open ocean without data assimilation. Similar skill was seen for other variables.

Our MIT-MSEAS multi-resolution 34 day ocean hindcast simulation in the two-way nested 4.5 km resolution domain and 1.5 km resolution domains will be used to represent the ocean environment that vehicles operates in. In what follows, we illustrate these fields, in the upper layers, in the 3D volume, at depth, and near the seabed.

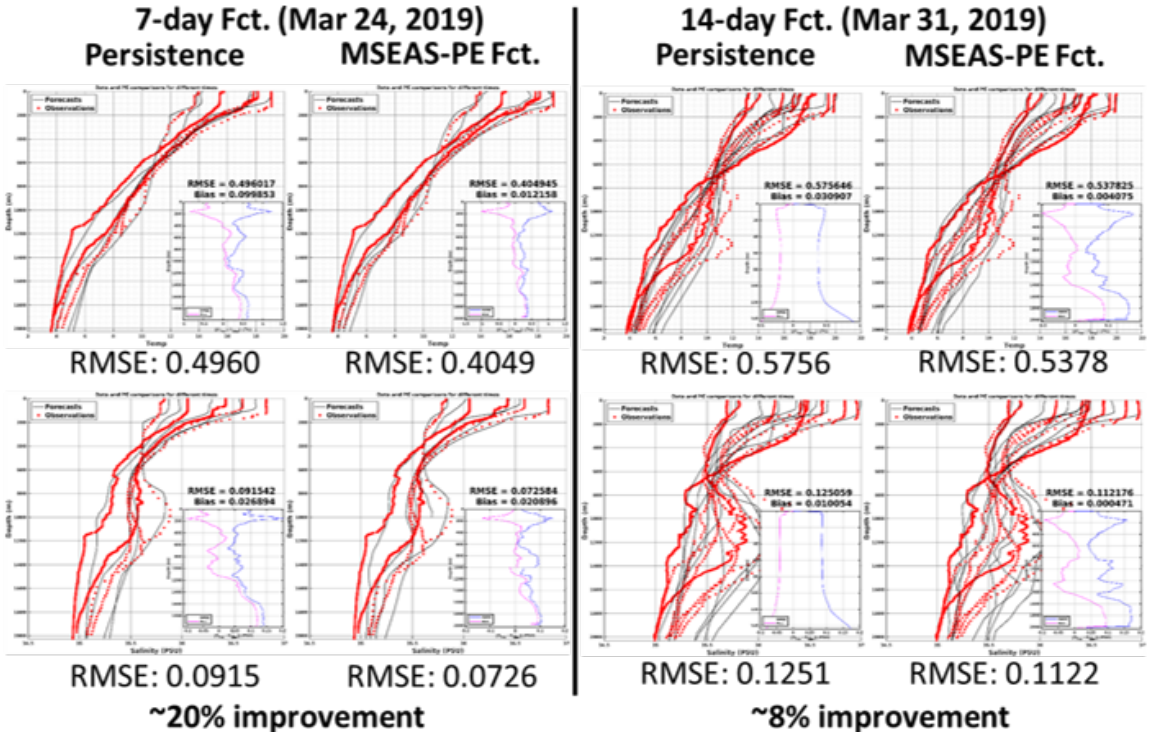

Figure 3-7: MSEAS Predictive Skill: red lines represent data observations, and the black lines represent the model forecasts. The MSEAS-PE model consistently beats persistence for 2 weeks.

3.2.3 Multiscale Ocean Currents and Circulations at Surface

We now illustrate the surface circulation features, using velocity and vorticity fields, just below the surface at 2 m depth.

Surface Velocity

In Figure 3-8, the surface velocity is shown in the 4.5 km and 1.5 km domains of our implicit nested simulations. The smaller domain provides higher-resolution near the Portuguese coast. Additionally, larger scales in atmospheric forcing somewhat inhibit smaller ocean scales at the surface. The higher-resolution domain is better able to capture the fine-scale structure that does survive.

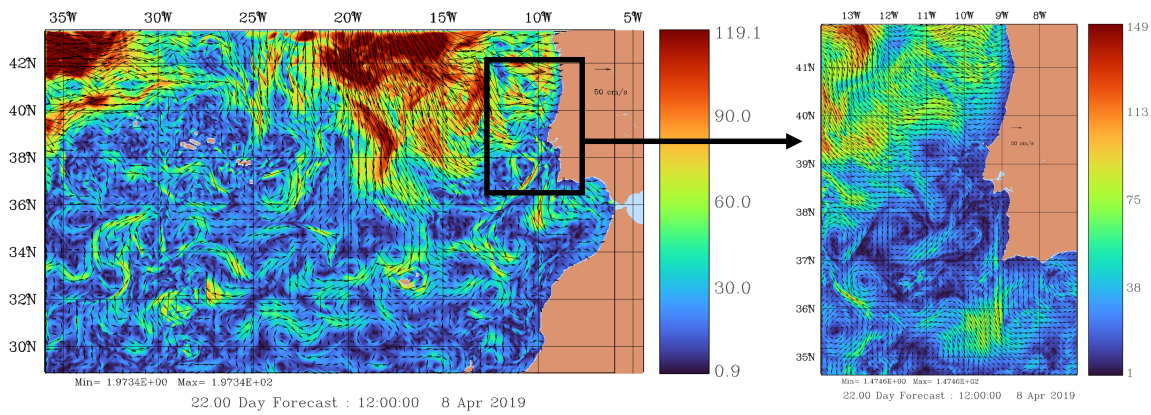

Figure 3-8: Surface velocity in the 4.5 km domain and implicitly nested 1.5 km domain. The magnitude of the velocity is shown in the colorbar, and the direction of the velocity is shown by the vector arrows.

Surface velocity is the most relevant factor for surface vehicle path planning, since vehicle trajectories are heavily affected by surface currents. In Figure 3-9, the surface velocity field (cm/s) magnitude and direction is shown for the duration of our MIT-MSEAS multi-resolution 34-day ocean forecast simulation in the 4.5 km resolution domain. On average, these surface velocities reflect the clockwise circulation of the Azores and Canary Currents along with the Portugal Current System (section 3.1.2). This general clockwise circulation is modulated by eddies, filaments and other smaller scale features. Episodically, atmospheric forcing overrides this background state,

locally changing directions and increasing speed. A prime example of this is the wind-induced high surface velocity that sweeps through the domain on April 16.

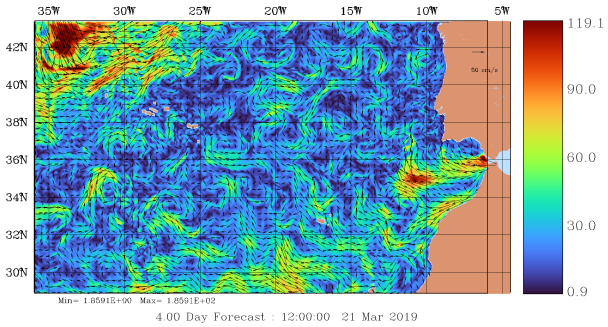

(a) March 21, 2019

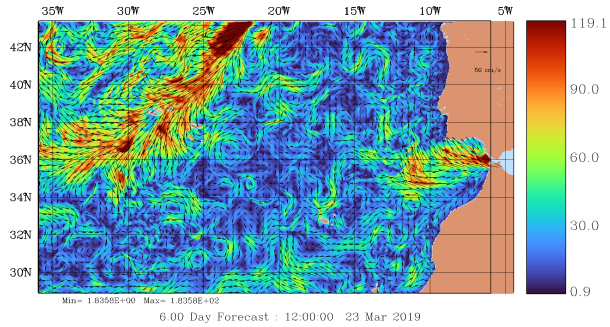

(b) March 23, 2019

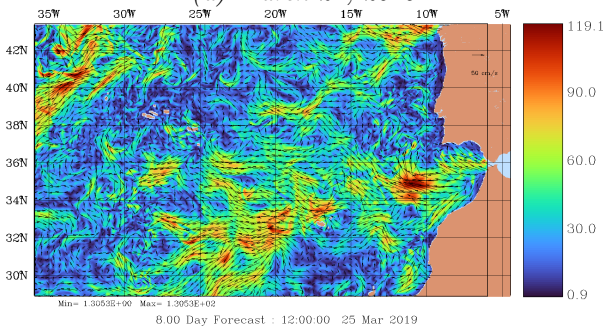

(c) March 25, 2019

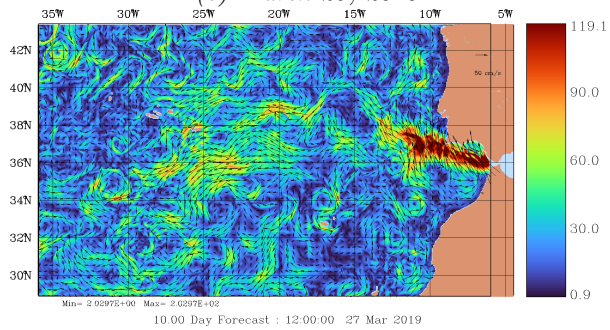

(d) March 27, 2019

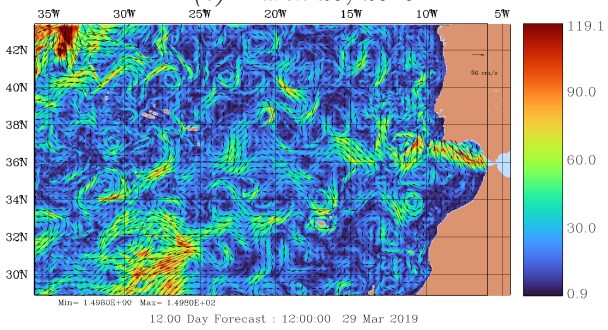

(e) March 29, 2019

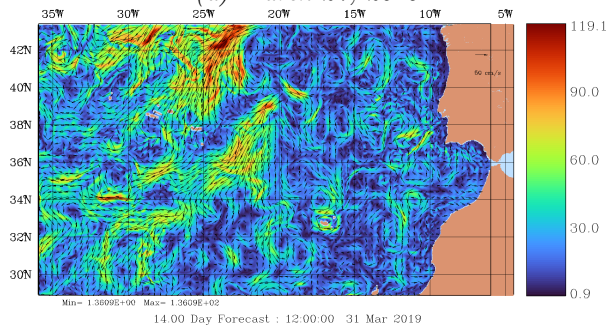

(f) March 31, 2019

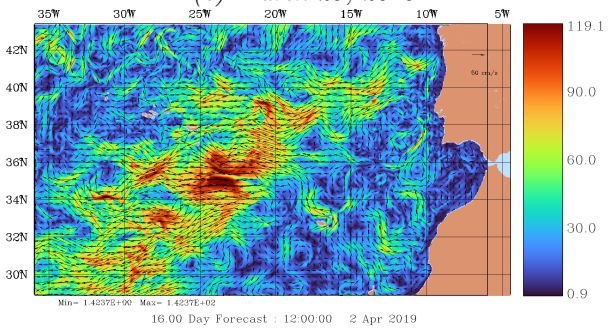

(g) April 2, 2019

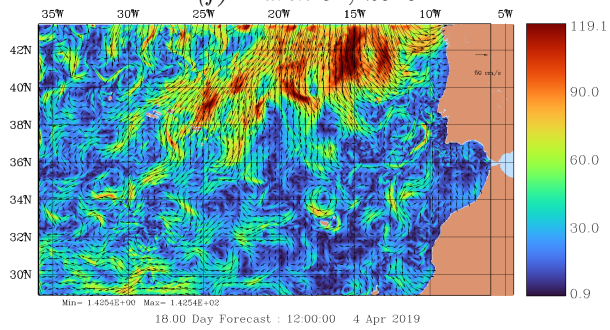

(h) April 4, 2019

Figure 3-9: Surface velocity field in magnitude (cm/s) and direction is shown every two days for the duration of our MIT-MSEAS multi-resolution 34 day ocean forecast simulation in the 4.5 km resolution domain. The magnitude of the velocity is shown in the colorbar, and the direction of the velocity is shown by the vector arrows (Figure Continued).

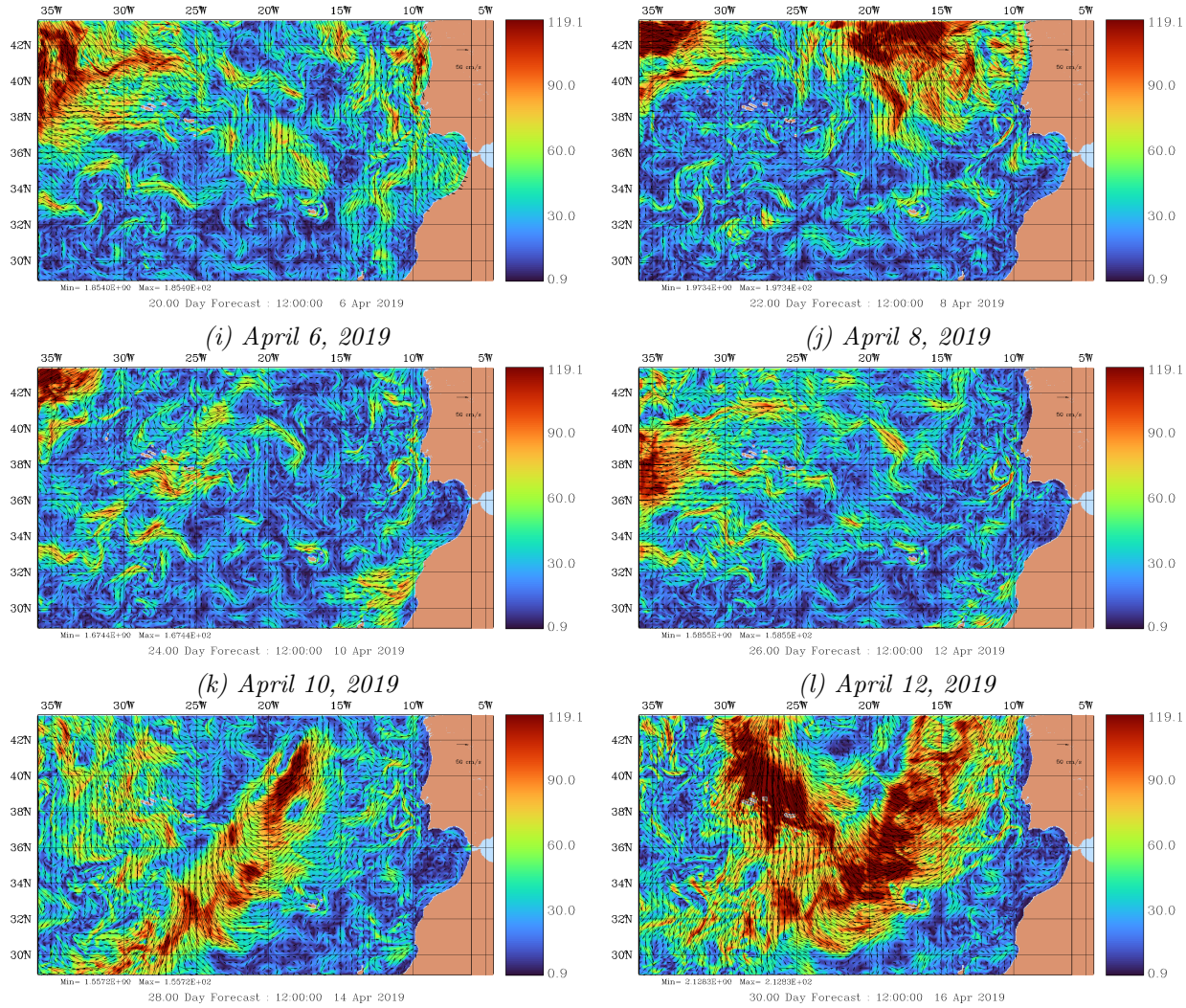

(i) April 6, 2019 *(j) April 8, 2019*

(k) April 10, 2019 *(l) April 12, 2019*

(m) April 14, 2019 *(n) April 16, 2019*

Figure 3-9: Continued: Surface velocity field in magnitude (cm/s) and direction is shown every two days for the duration of our MIT-MSEAS multi-resolution 34 day ocean forecast simulation in the 4.5 km resolution domain. The magnitude of the velocity is shown in the colorbar, and the direction of the velocity is shown by the vector arrows.

The surface velocity of the 1.5 km nested domain along the coast of Portugal is shown in Figure 3-10. While there is variation in the direction and magnitude of the surface velocity along the coast, the surface flow tends to flow in a clockwise direction and south along the Iberian Peninsula, which was described in Section 3.1.2 on ocean conditions in Portugal.

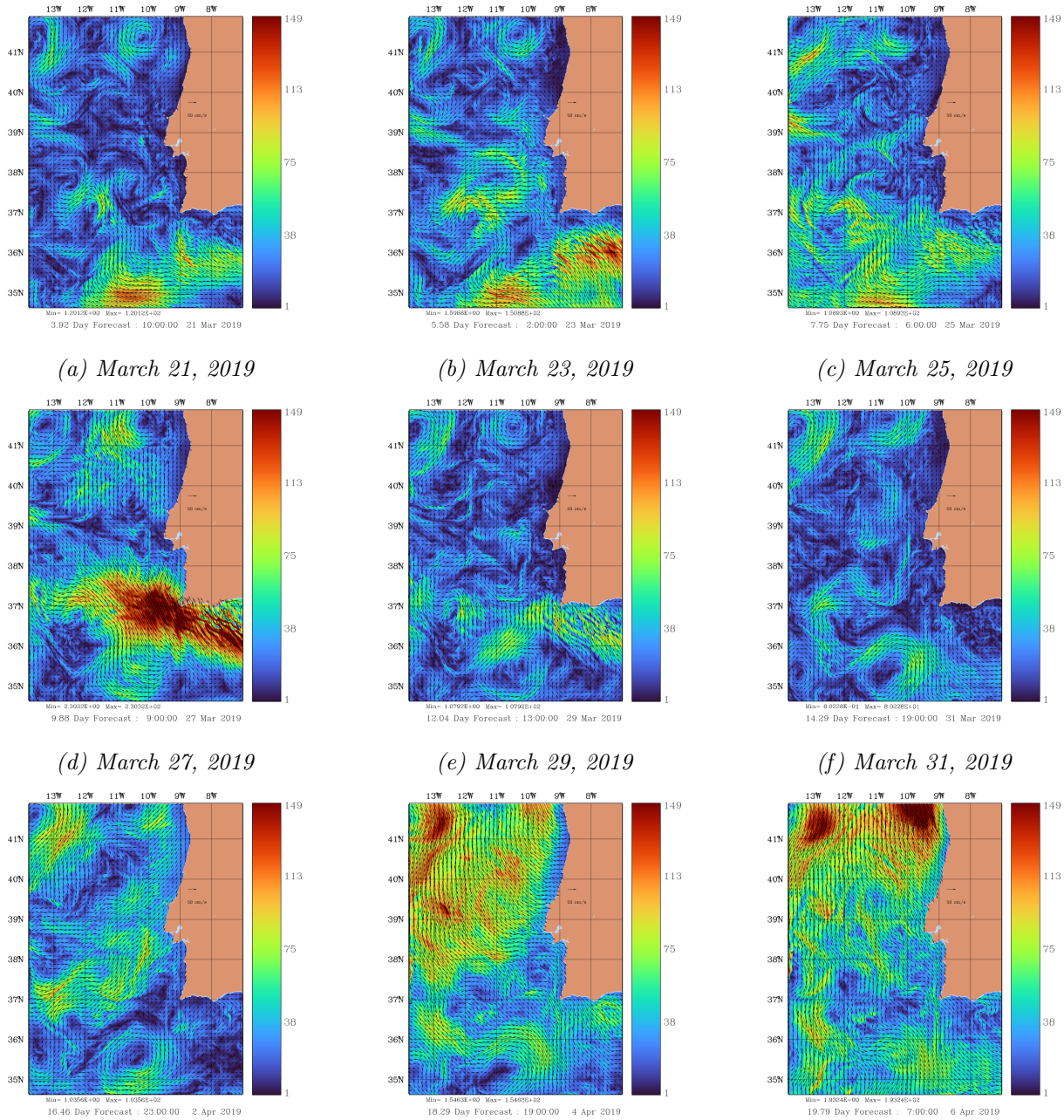

(a) March 21, 2019 *(b) March 23, 2019* *(c) March 25, 2019*

(d) March 27, 2019 *(e) March 29, 2019* *(f) March 31, 2019*

(g) April 2, 2019 *(h) April 4, 2019* *(i) April 6, 2019*

Figure 3-10: Surface velocity field in magnitude (cm/s) and direction is shown every two days for the duration of our MIT-MSEAS multi-resolution 34 day ocean forecast simulation in the 1.5 km resolution domain. The magnitude of the velocity is shown in the colorbar, and the direction of the velocity is shown by the vector arrows (Figure Continued).

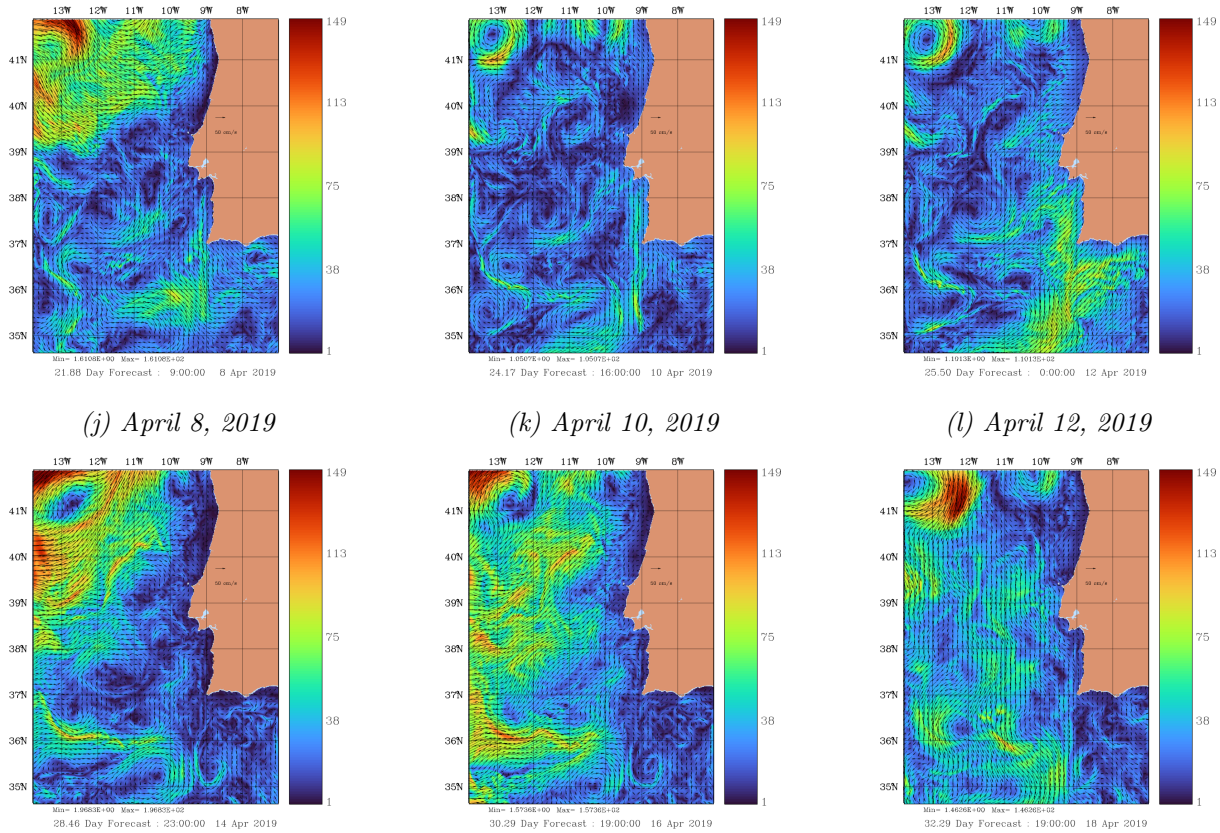

(j) April 8, 2019 *(k) April 10, 2019* *(l) April 12, 2019*

(m) April 14, 2019 *(n) April 16, 2019* *(o) April 18, 2019*

Figure 3-10: Continued: Surface velocity field in magnitude (cm/s) and direction is shown every two days for the duration of our MIT-MSEAS multi-resolution 34 day ocean forecast simulation in the 1.5 km resolution domain. The magnitude of the velocity is shown in the colorbar, and the direction of the velocity is shown by the vector arrows.

Surface Vorticity

Vorticity is relevant for vehicle path planning as it highlights the circulation features, such as eddies and jets, and includes the finer scales that are affected by the coastline and bathymetry. The scaled vorticity is unitless, as it is scaled by the Coriolis factor [17].

In Figure 3-11), the surface scaled vorticity is shown in the 4.5 km and 1.5 km domains of our implicit two-way nested simulations. The smaller domains permit higher-resolution simulations near the coast and around the islands.

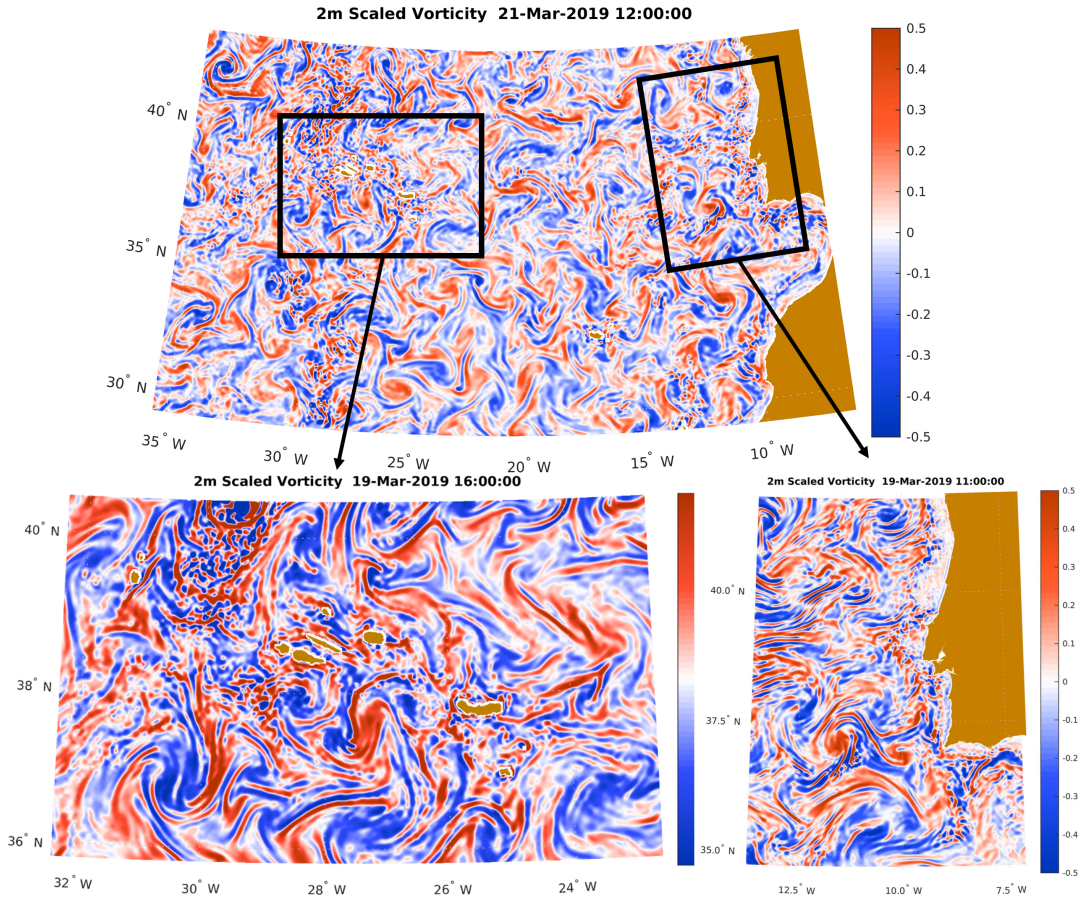

Figure 3-11: Surface scaled vorticity in the 4.5 km domain and nested 1.5 km domain. The magnitude of the scaled vorticity is unitless, and is shown in the colorbar.

In Figure 3-12, the scaled surface vorticity is shown on a timescale from our MIT-MSEAS multi-resolution 34 day ocean forecast simulation in the 4.5 km resolution domain. The magnitude of the scaled surface vorticity is shown in the colorbar. Vorticity is a relevant measurement for vehicle path planning, as smaller scale features, such as eddies, are easier to see and shows patterns and movement as the surface velocity interacts with the coastline and bathymetry of the domain. Vorticity is unitless, as it is scaled by the Coriolis factor at 2m, highlighting the finer scales generated by our higher resolution simulation [17]. As is illustrated in Figure 3-12, there is increased vorticity that sweeps through the domain on April 14th-16th.

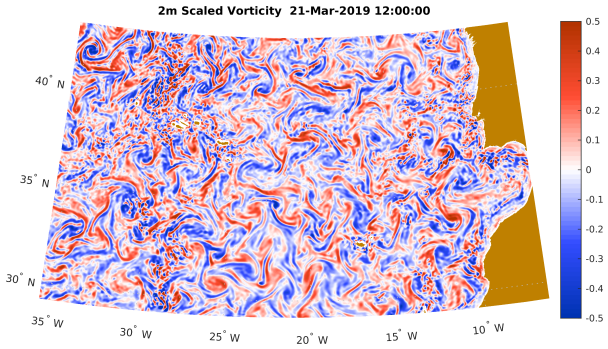

(a) March 21, 2019

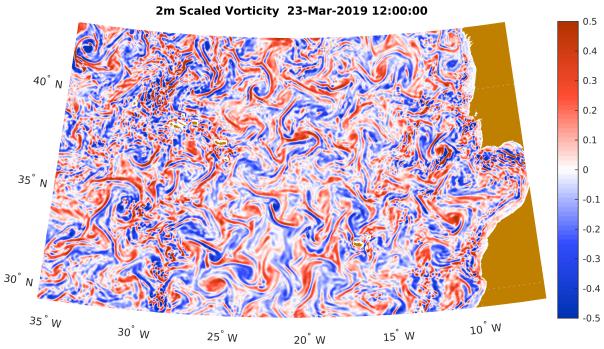

(b) March 23, 2019

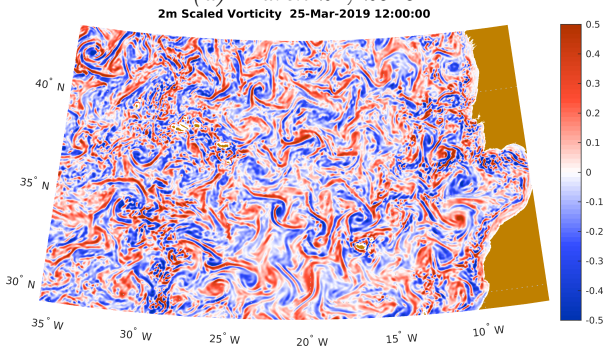

(c) March 25, 2019

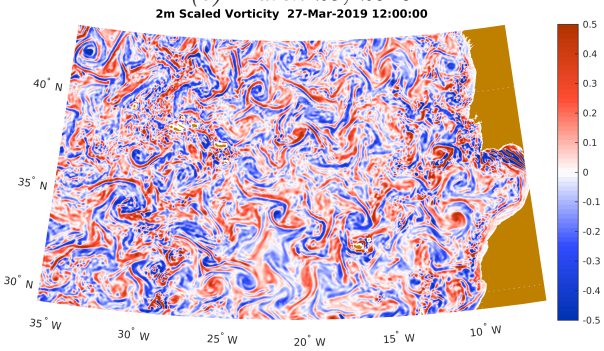

(d) March 27, 2019

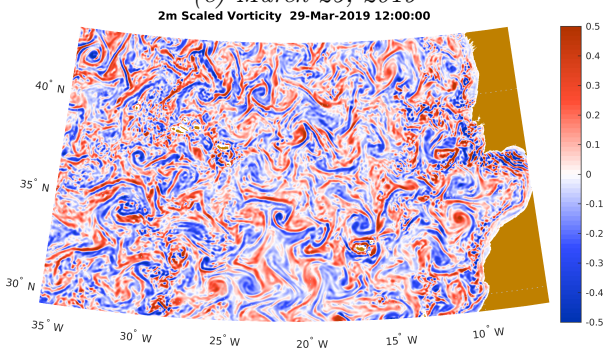

(e) March 29, 2019

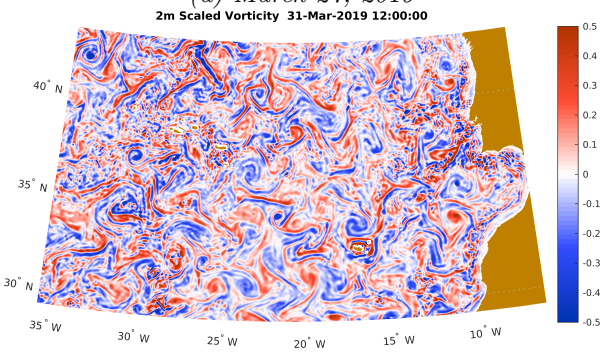

(f) March 31, 2019

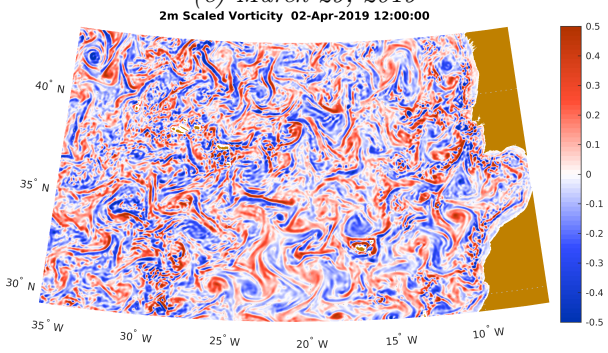

(g) April 2, 2019

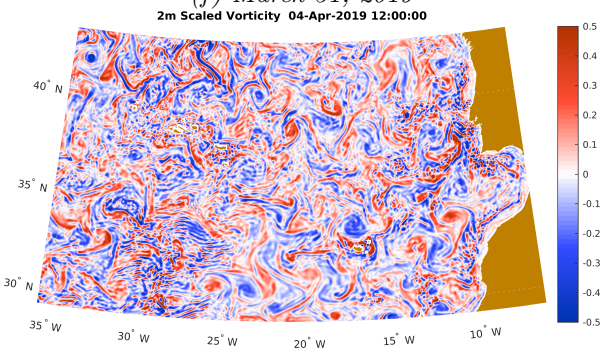

(h) April 4, 2019

Figure 3-12: Surface scaled vorticity field in magnitude every two days for the duration of our MIT-MSEAS multi-resolution 34 day ocean forecast simulation in the 4.5 km resolution domain. The magnitude of the scaled vorticity is unitless, and is shown in the colorbar (Figure Continued).

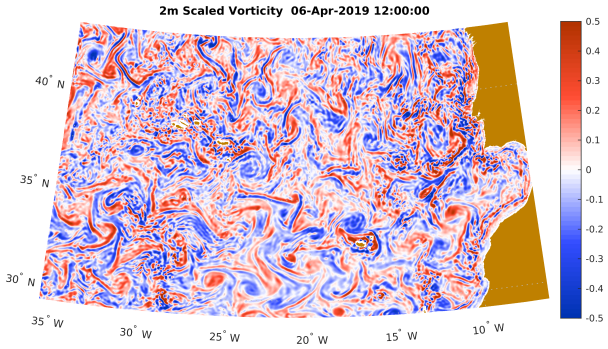

(i) April 6, 2019

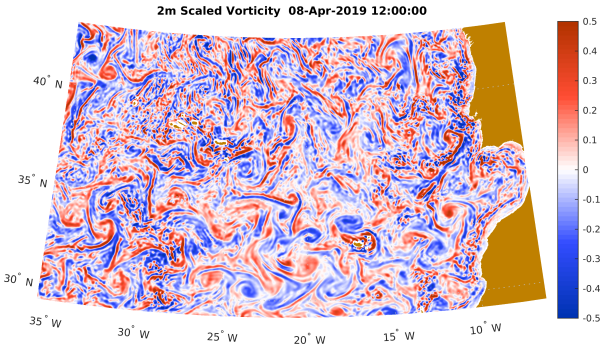

(j) April 8, 2019

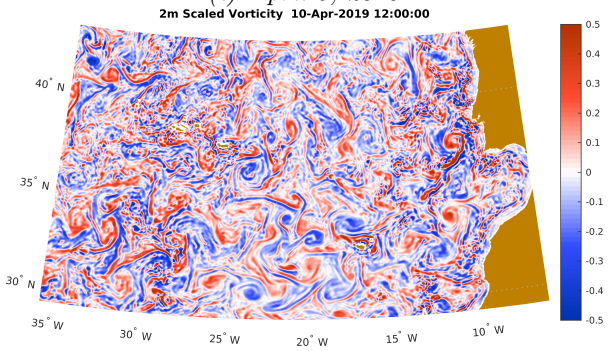

(k) April 10, 2019

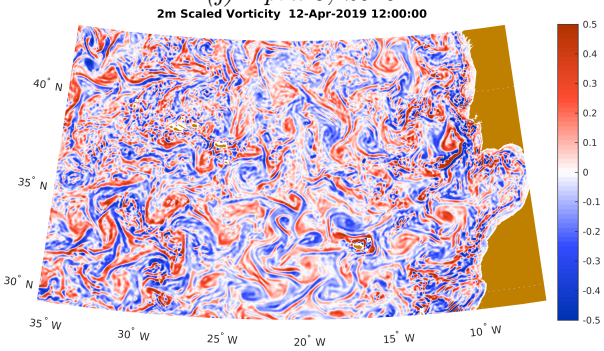

(l) April 12, 2019

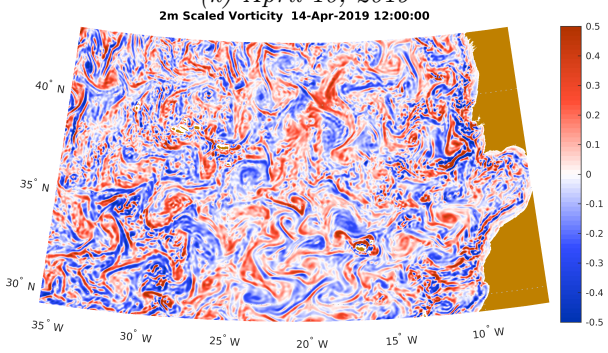

(m) April 14, 2019

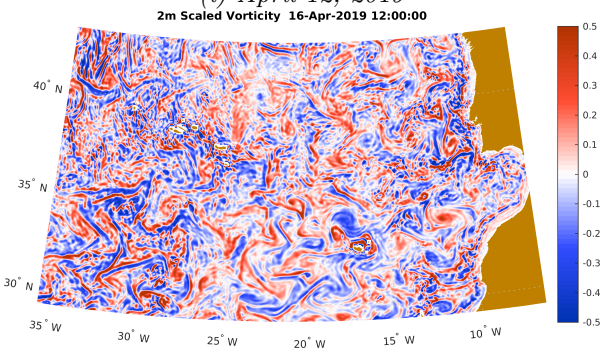

(n) April 16, 2019

Figure 3-12: Continued: Surface scaled vorticity field in magnitude every two days for the duration of our MIT-MSEAS multi-resolution 34 day ocean forecast simulation in the 4.5 km resolution domain. The magnitude of the scaled vorticity is unitless, and is shown in the colorbar.

The surface scaled vorticity of the 1.5 km nested domain along the coast of Portugal is shown in Figure 3-13 below, and illustrates the time-dependent changes.

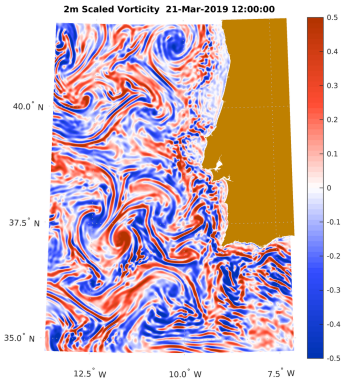

(a) March 21, 2019

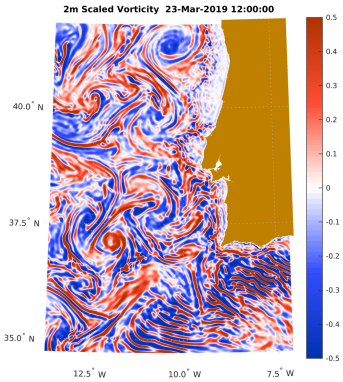

(b) March 23, 2019

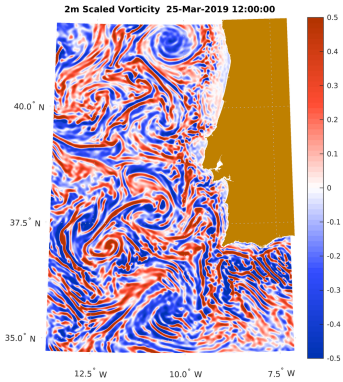

(c) March 25, 2019

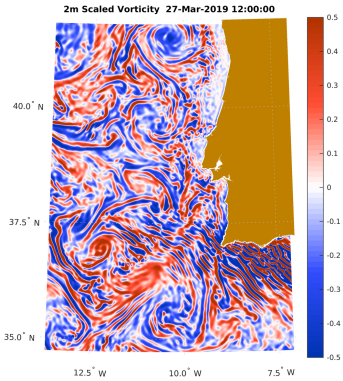

(d) March 27, 2019

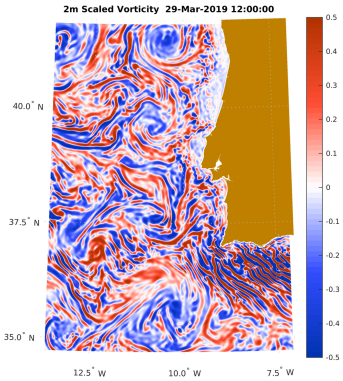

(e) March 29, 2019

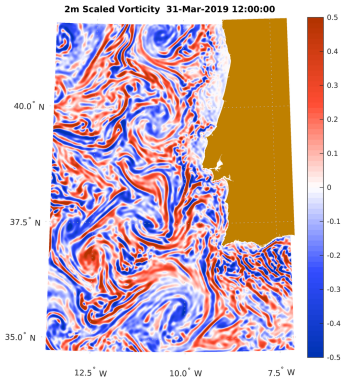

(f) March 31, 2019

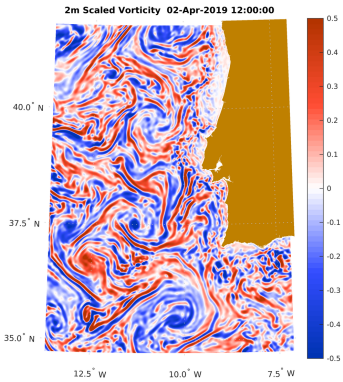

(g) April 2, 2019

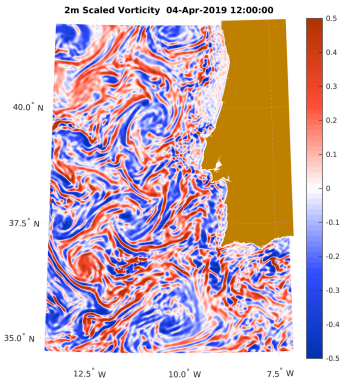

(h) April 4, 2019

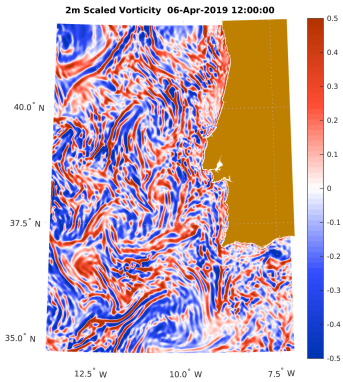

(i) April 6, 2019

Figure 3-13: Surface scaled vorticity field in magnitude every two days for the duration of our MIT-MSEAS multi-resolution 34 day ocean forecast simulation in the 1.5 km resolution domain. The magnitude of the scaled vorticity is unitless, and is shown in the colorbar (Figure Continued).

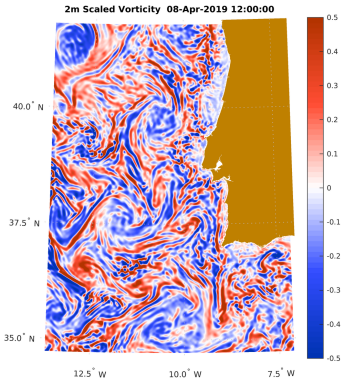

(j) April 8, 2019

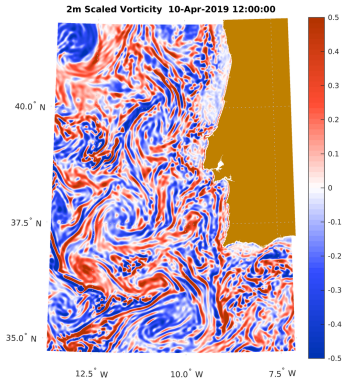

(k) April 10, 2019

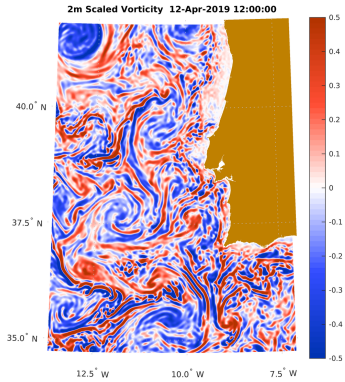

(l) April 12, 2019

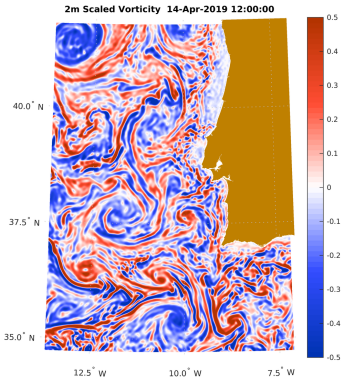

(m) April 14, 2019

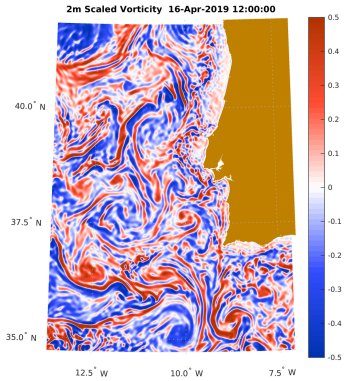

(n) April 16, 2019

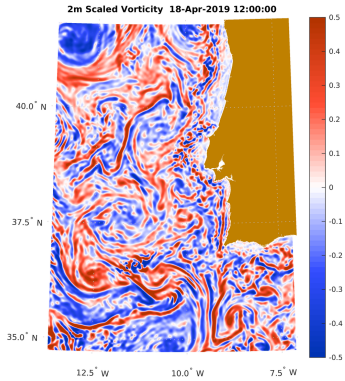

(o) April 18, 2019

Figure 3-13: Continued: Surface scaled vorticity field in magnitude every two days for the duration of our MIT-MSEAS multi-resolution 34 day ocean forecast simulation in the 1.5 km resolution domain. The magnitude of the scaled vorticity is unitless, and is shown in the colorbar.

3.2.4 Multiscale Ocean Currents and Circulations at Depth

As described in Section 3.1.2, there are relevant currents at depths and along the ocean bottom in this region. This is especially applicable to this 34 day ocean forecast during March and April, as springtime coastal upwelling will bring circulation and poleward currents.

Vertical Variability

Our simulations are 4-dimensional (4D) such that we can complete path planning for bottom-traveling vehicles. To illustrate the vertical variability, we show 4D currents

along vertical sections. We first consider a slice of the domain from Lisbon, Portugal (38.730° N, 9.15° W) to the island of Nordeste, Sao Miguel in the Azores (37.83° N, 25.15° W), shown in Figure 3-14. These vertical slices show the velocity both along section (tangent to the slice) and across section (orthogonal to the slice). This shows that currents can be the largest right below the surface, around 50 to 100 m depth, and that they then decay with depth, up to about 1000 to 2000 m. Near bottom currents are much smaller, often less than 5 cm/s, except near steeper topography.

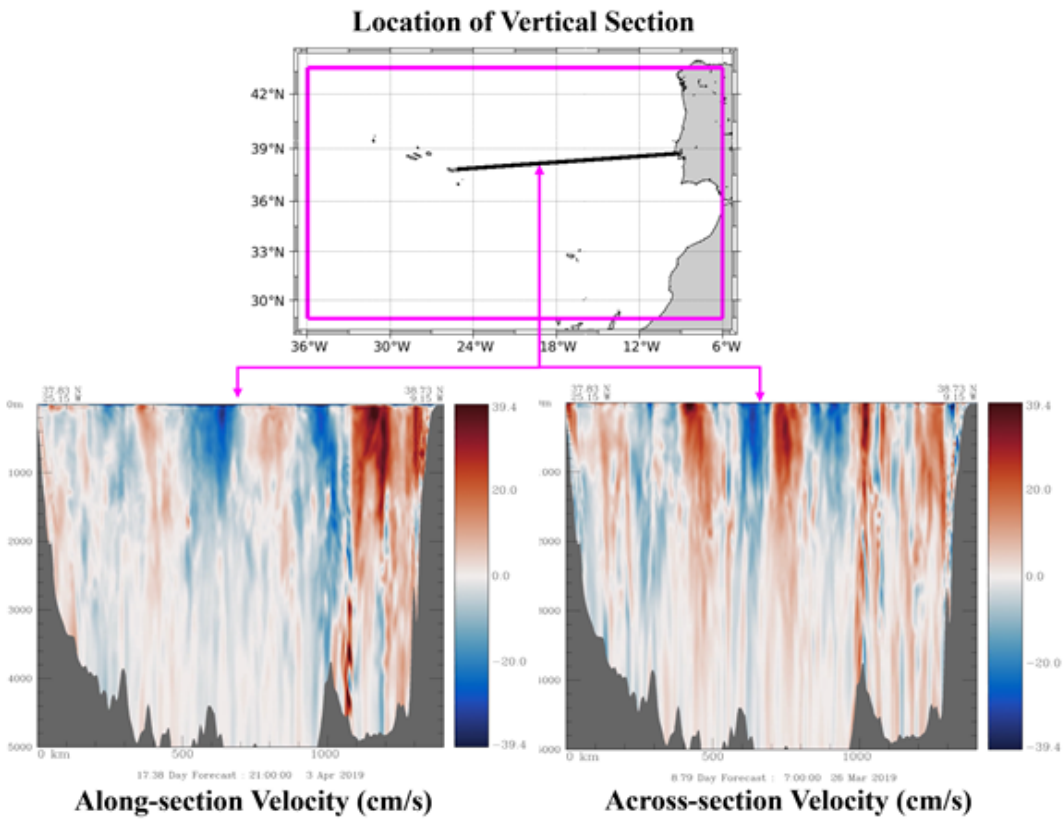

Figure 3-14: Location of vertical sections of along-section and across-section velocity (cm/s), as predicted from our data-driven MIT-MSEAS ocean simulations.

Figures 3-15 and 3-16 illustrate the variability in time of the along and across velocities in the section. There is a seamount located at about 1000 km from the Portuguese coast and is seen here on the slice. This leads to stronger velocities near the seamount showing the development of Taylor columns, as well as internal tides.

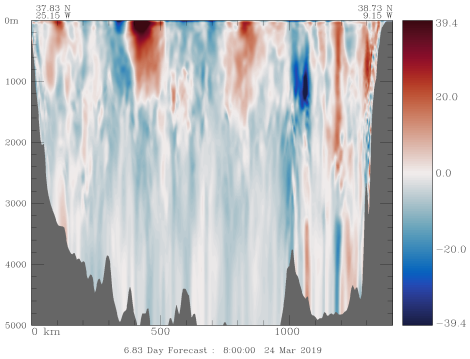

(a) March 24, 2019

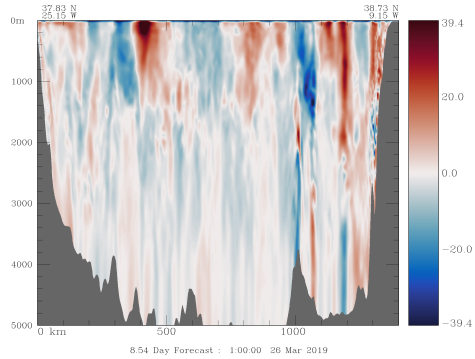

(b) March 26, 2019

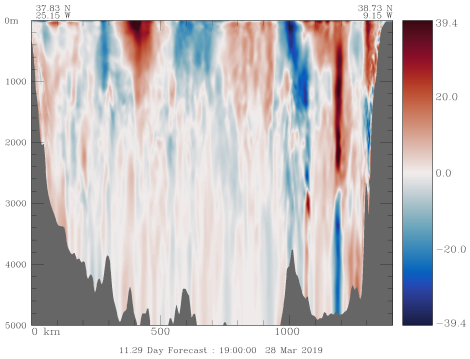

(c) March 28, 2019

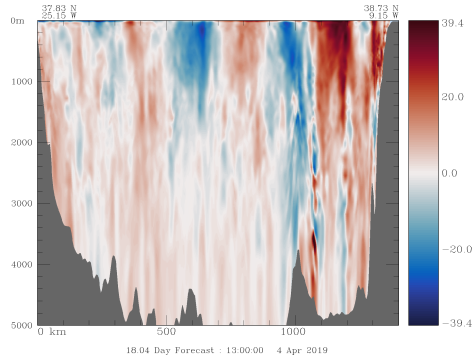

(d) April 4, 2019

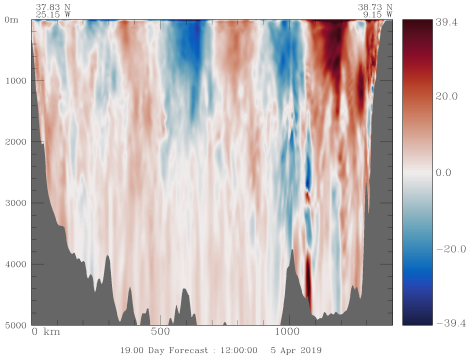

(e) April 5, 2019

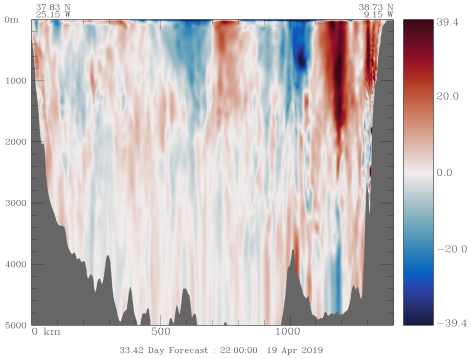

(f) April 19, 2019

Figure 3-15: Select figures of vertical sections of along-section velocity (cm/s) from Lisbon to Nordeste, Sao Miguel. Velocity magnitude is shown in the colorbar, and the direction is tangent to the slice.

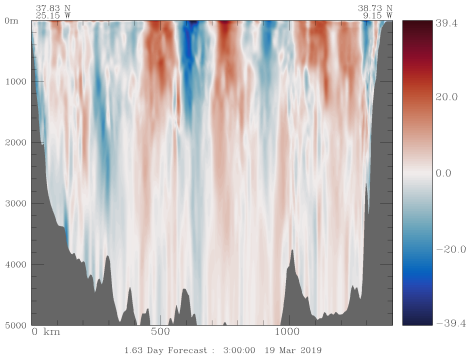

(a) March 19, 2019

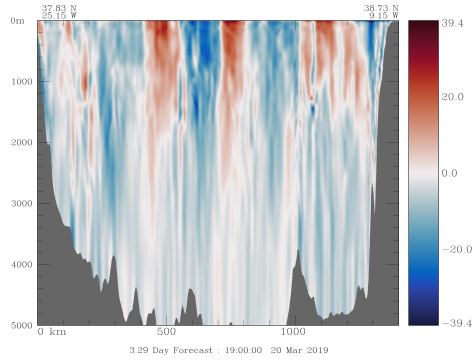

(b) March 20, 2019

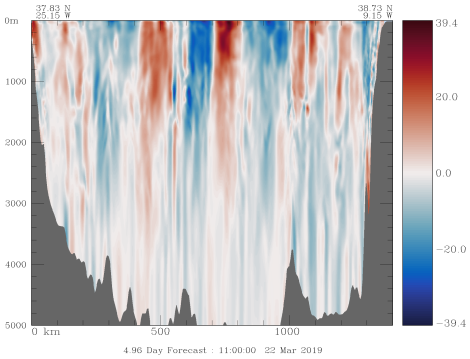

(c) March 22, 2019

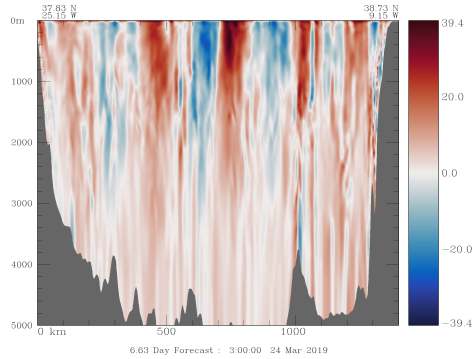

(d) March 24, 2019

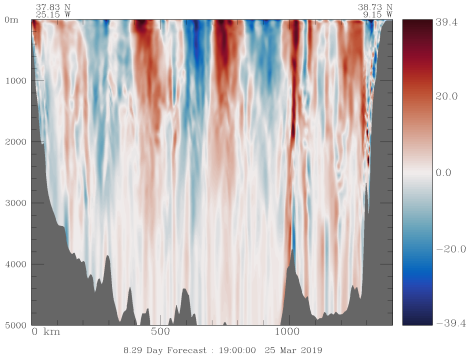

(e) March 25, 2019

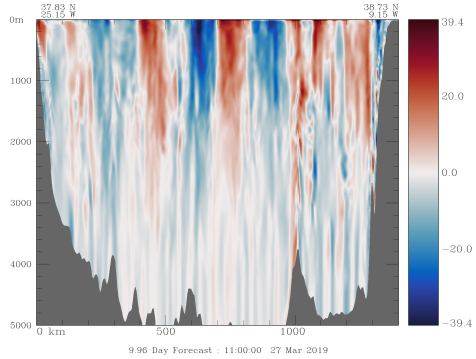

(f) March 27, 2019

Figure 3-16: Select figures of vertical sections of across-section velocity (cm/s) from Lisbon to Nordeste, Sao Miguel. Velocity magnitude is shown in the colorbar, and the direction is orthogonal to the slice.

Deep Velocity Fields

In Figure 3-17, we illustrate the evolution of the deep velocity and scaled vorticity fields at 3000 m in the larger 4.5 km resolution domain, as hindcast by our MSEAS ocean modeling system. Note that in these deep fields, more smaller-scale features are present than in the surface fields; the effect of the large-scale atmospheric forcing

is no longer present. Instead, the deep velocity fields are a result of interactions between the currents, eddies, local topography, and the tides (especially in shallower regions where tides are stronger). Throughout this period, the strongest currents are generally located near steep topography, especially near the shelf break off the Portuguese coast. The uniform light blue areas in the figures indicate where the bathymetry is shallower than 3000 m.

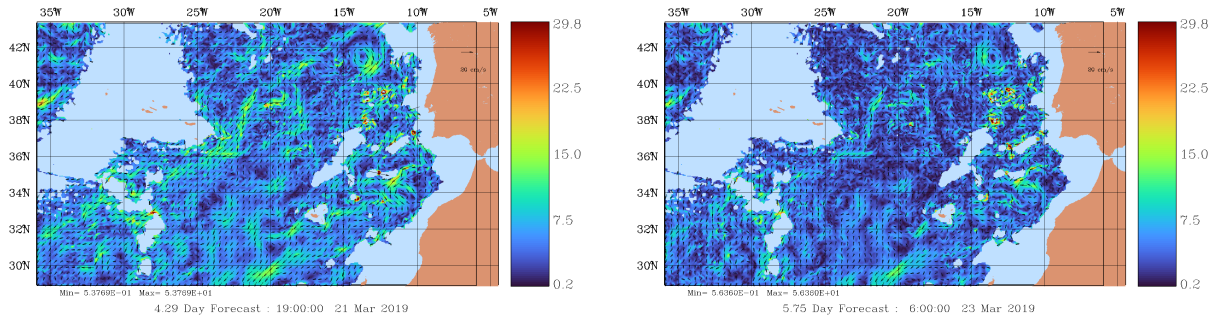

(a) March 21, 2019

(b) March 23, 2019

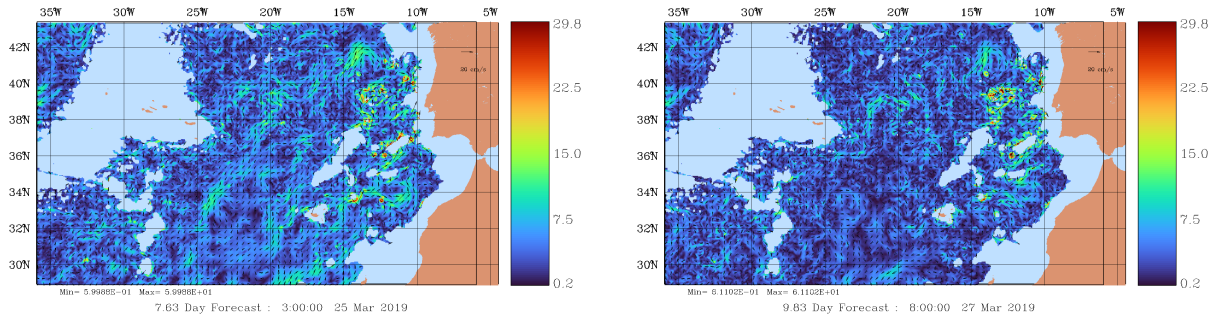

(c) March 25, 2019

(d) March 27, 2019

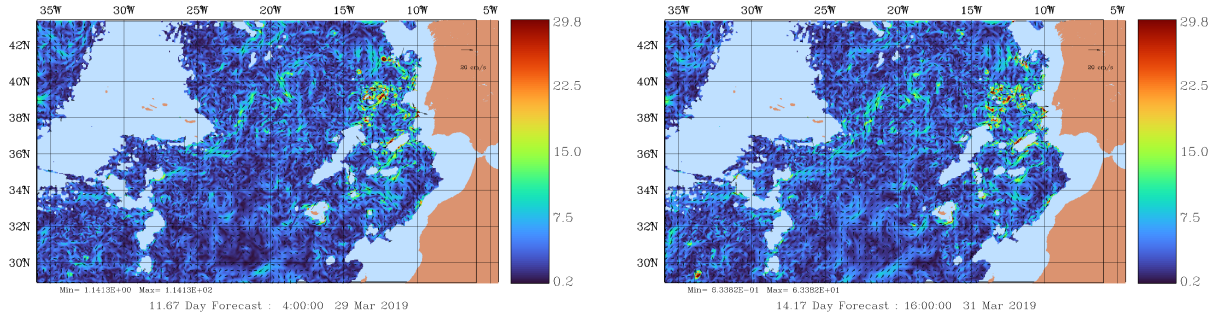

(e) March 29, 2019

(f) March 31, 2019

Figure 3-17: Velocity field at 3000 m of depth in magnitude (cm/s) and direction is shown every two days for the duration of our MIT-MSEAS multi-resolution 34 day ocean forecast simulation in the 4.5 km resolution domain. The magnitude of the velocity is shown in the colorbar, and the direction of the velocity is shown by the vector arrows (Figure Continued).

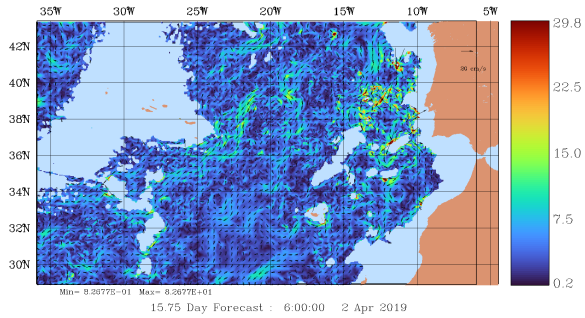

(g) April 2, 2019

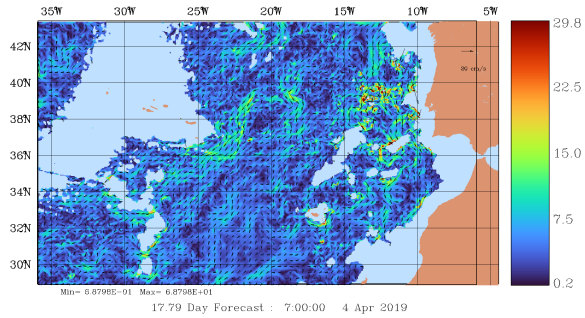

(h) April 4, 2019

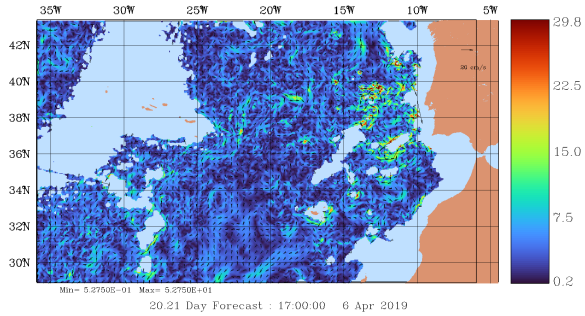

(i) April 6, 2019

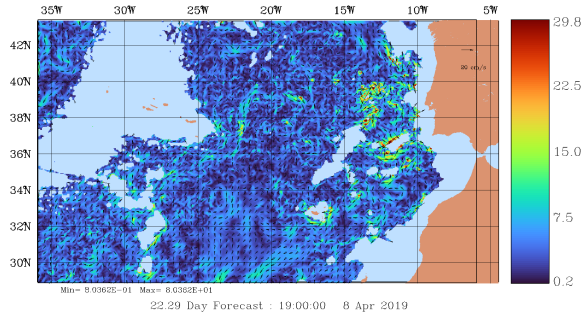

(j) April 8, 2019

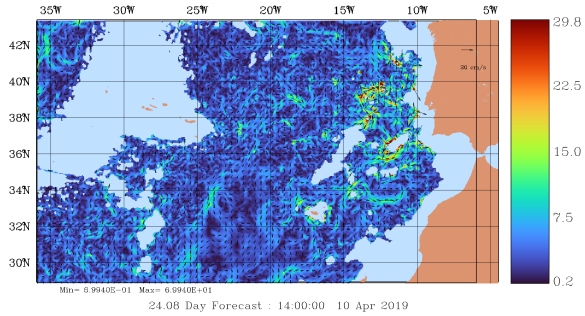

(k) April 10, 2019

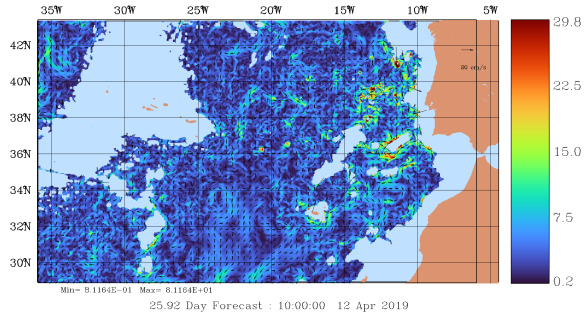

(l) April 12, 2019

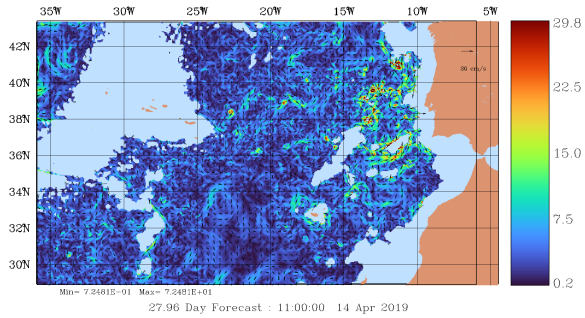

(m) April 14, 2019

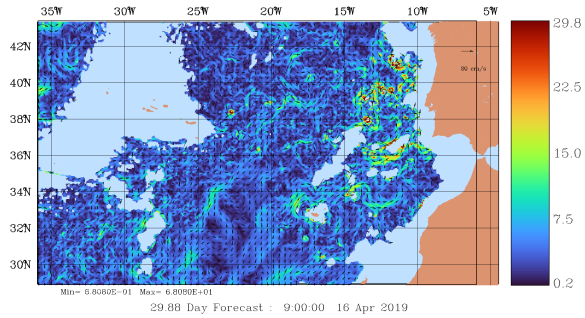

(n) April 16, 2019

Figure 3-17: Continued: Velocity field at 3000 m of depth in magnitude (cm/s) and direction is shown every two days for the duration of our MIT-MSEAS multi-resolution 34 day ocean forecast simulation in the 4.5 km resolution domain. The magnitude of the velocity is shown in the colorbar, and the direction of the velocity is shown by the vector arrows.

Bottom Velocity Fields

In Figure 3-18), the bottom velocity field is shown in the implicit two-way nested 4.5 km and 1.5 km domains. The later higher-resolution domain provides higher resolution fields near the Portugal coastline.

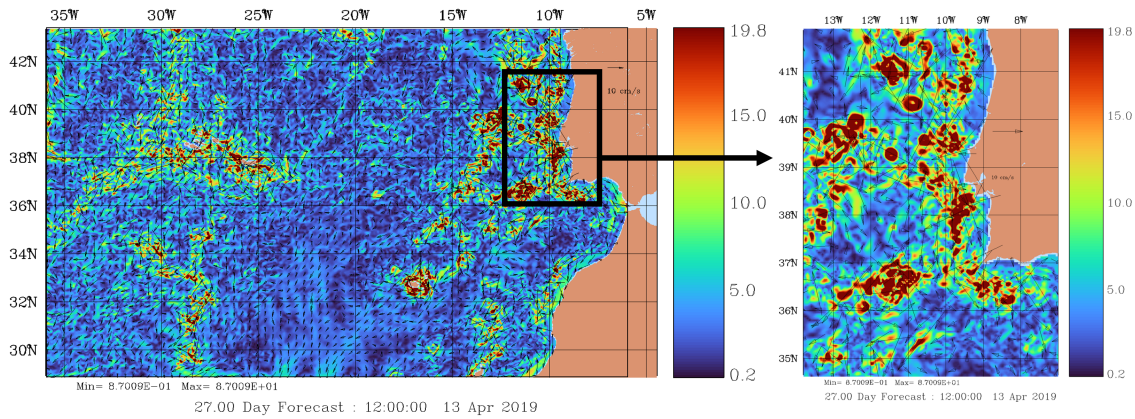

Figure 3-18: Bottom velocity in the 4.5 km domain and nested 1.5 km domain (velocity vectors overlaid on velocity magnitude shown in colorbar).

.

In Figure 3-19, the evolution of the bottom velocity (cm/s) is shown for the 34 days of our simulation. The magnitude of the velocity is shown in the colorbar, and the direction of the velocity is shown by the vector arrows. Bottom velocity is the most relevant factor for bottom-travelling vehicle path planning, since vehicle trajectories are heavily affected by currents. The time-dependent changes of the bottom velocity are illustrated by this figure. Again we see the interactions between the currents, eddies, the local topography, and the tides. These interaction are strongest on the shelf and shelfbreak; around seamounts and islands; and along the Mid-Atlantic Ridge.

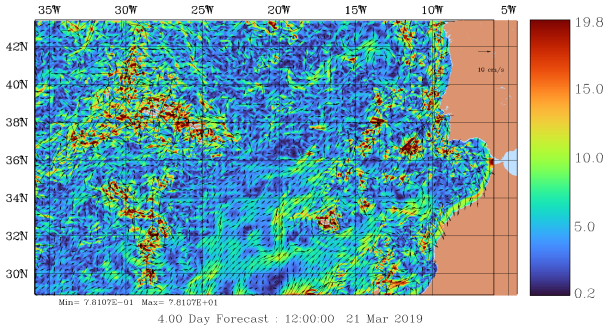

(a) March 21, 2019

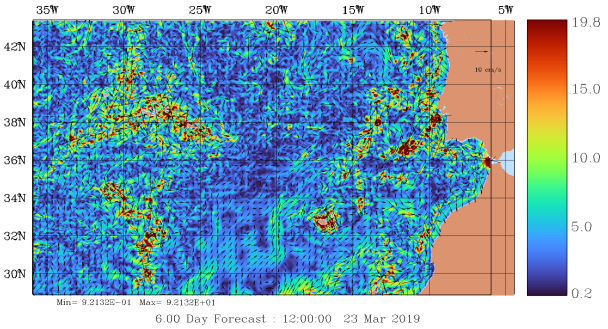

(b) March 23, 2019

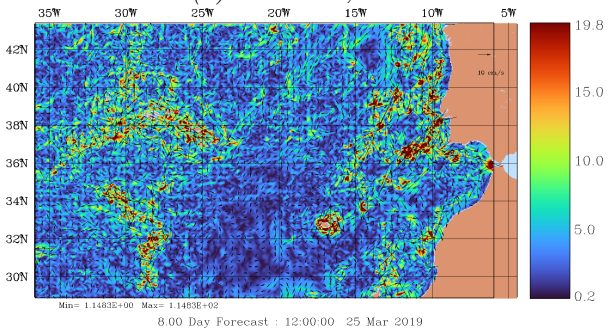

(c) March 25, 2019

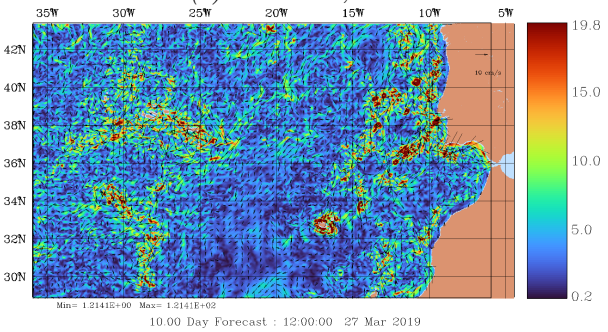

(d) March 27, 2019

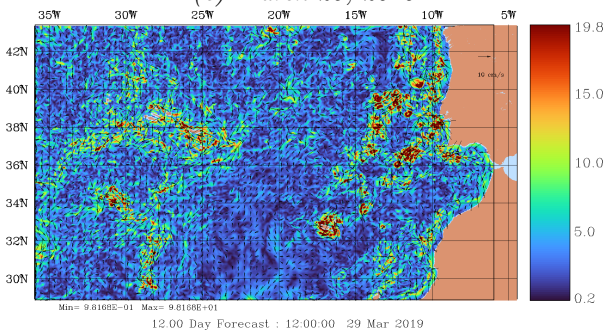

(e) March 29, 2019

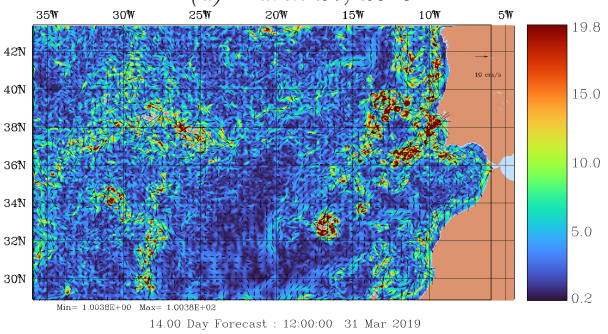

(f) March 31, 2019

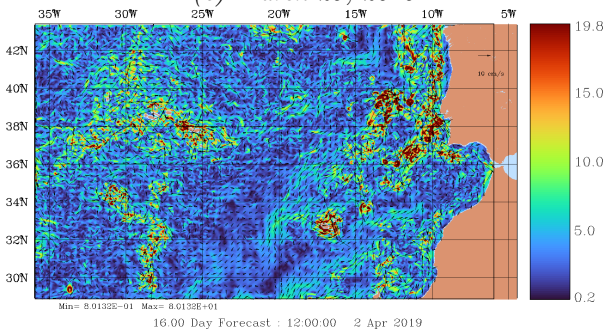

(g) April 2, 2019

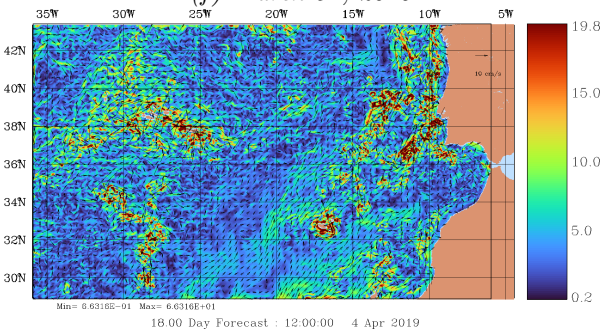

(h) April 4, 2019

Figure 3-19: Bottom velocity field in magnitude (cm/s) and direction is shown every two days for the duration of our MIT-MSEAS multi-resolution 34 day ocean forecast simulation in the 4.5 km resolution domain. The magnitude of the velocity is shown in the colorbar, and the direction of the velocity is shown by the vector arrows (Figure Continued).

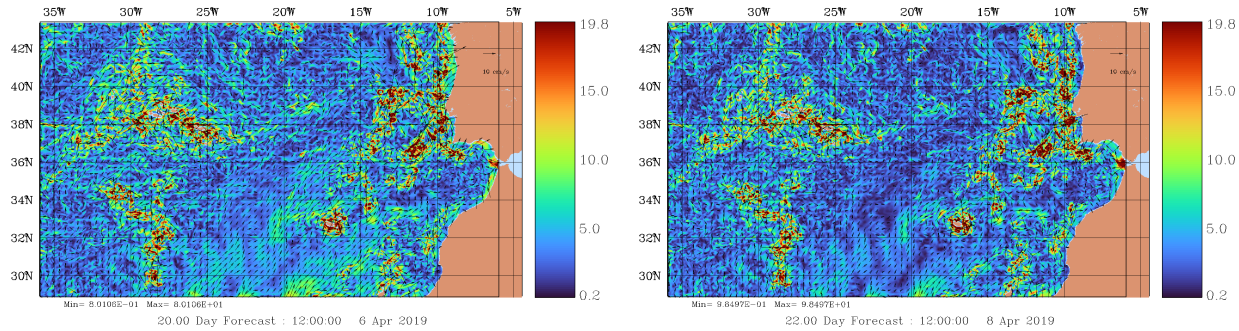

(i) April 6, 2019

(j) April 8, 2019

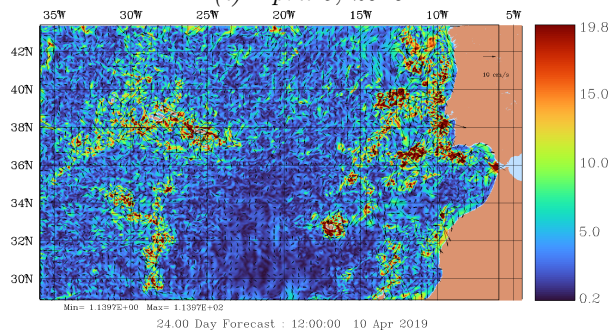

(k) April 10, 2019

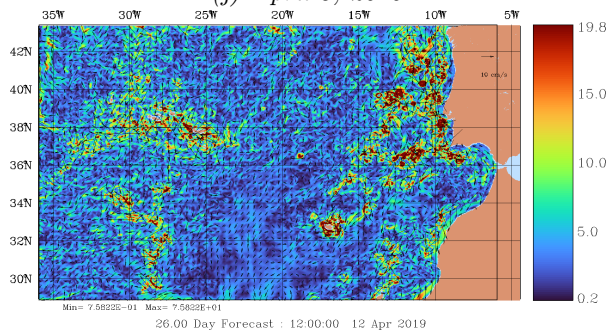

(l) April 12, 2019

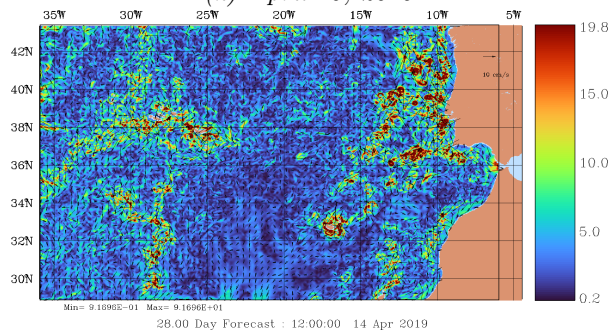

(m) April 14, 2019

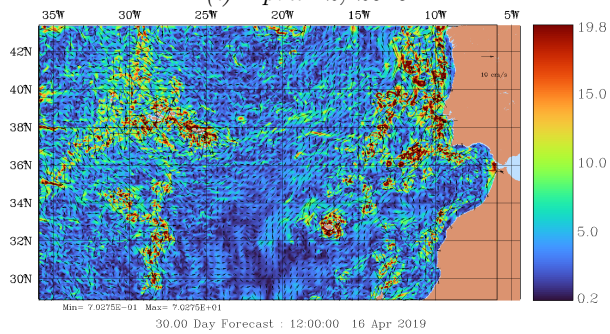

(n) April 16, 2019

Figure 3-19: Continued: Bottom velocity field in magnitude (cm/s) and direction is shown every two days for the duration of our MIT-MSEAS multi-resolution 34 day ocean forecast simulation in the 4.5 km resolution domain. The magnitude of the velocity is shown in the colorbar, and the direction of the velocity is shown by the vector arrows.

The bottom velocity of the 1.5 km nested domain along the coast of Portugal is shown in Figure 3-20.

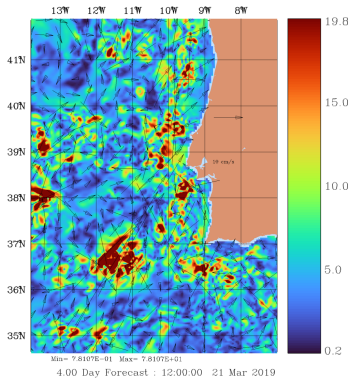

(a) March 21, 2019

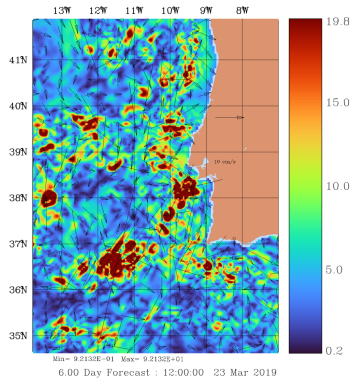

(b) March 23, 2019

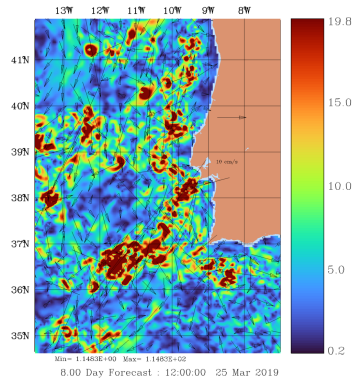

(c) March 25, 2019

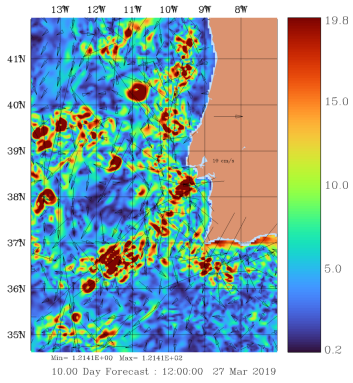

(d) March 27, 2019

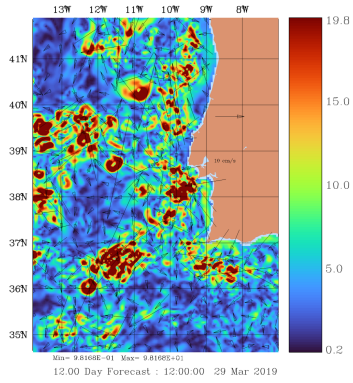

(e) March 29, 2019

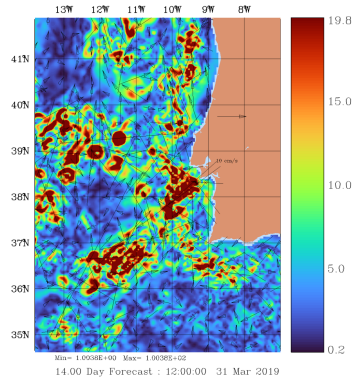

(f) March 31, 2019

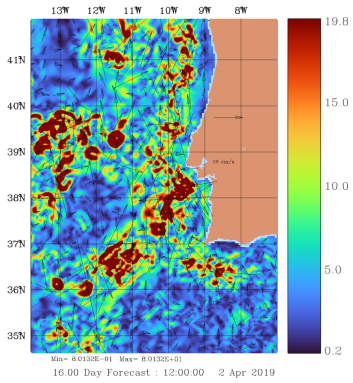

(g) April 2, 2019

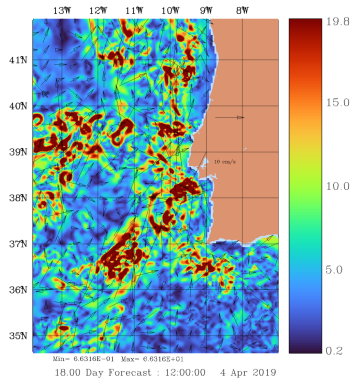

(h) April 4, 2019

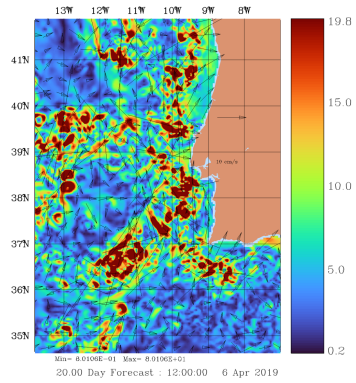

(i) April 6, 2019

Figure 3-20: Bottom velocity field in magnitude (cm/s) and direction is shown every two days for the duration of our MIT-MSEAS multi-resolution 34 day ocean forecast simulation in the 1.5 km resolution domain. The magnitude of the velocity is shown in the colorbar, and the direction of the velocity is shown by the vector arrows (Figure Continued).

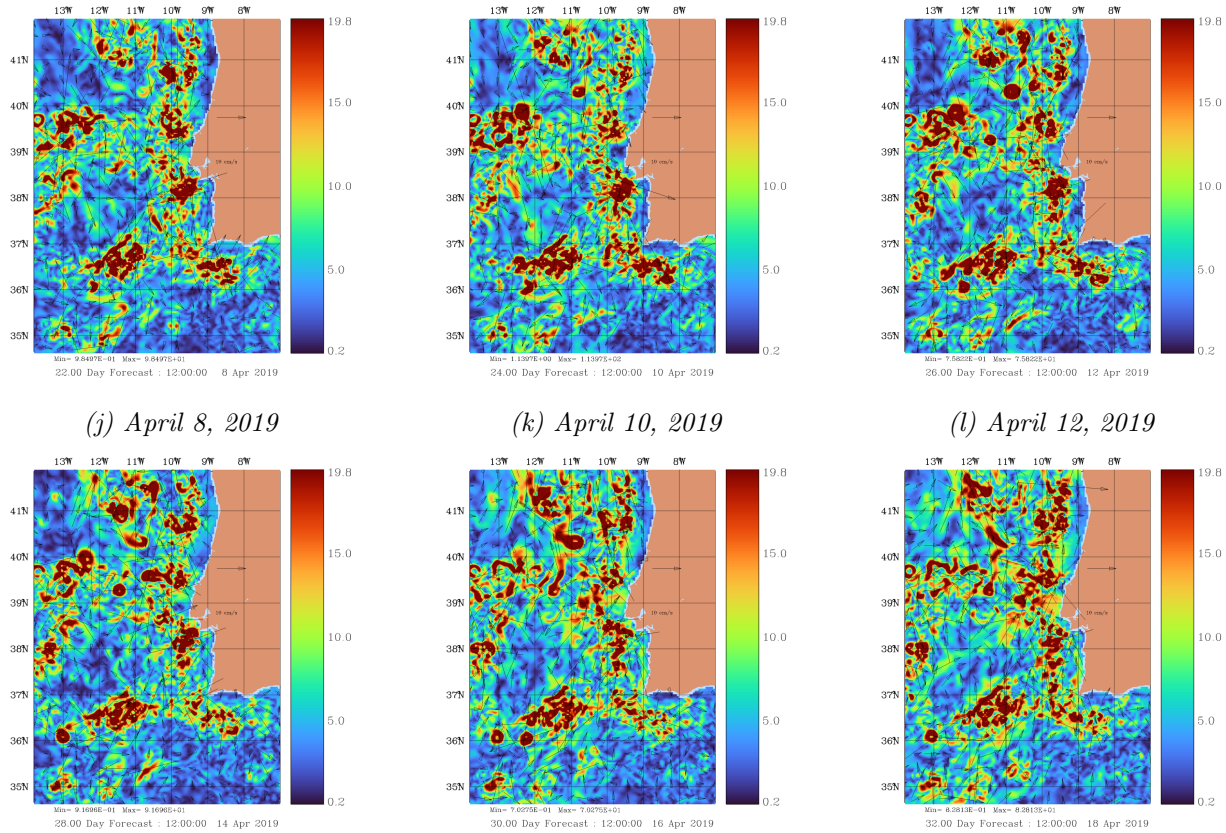

(j) April 8, 2019 *(k) April 10, 2019* *(l) April 12, 2019*

(m) April 14, 2019 *(n) April 16, 2019* *(o) April 18, 2019*

Figure 3-20: Continued: Bottom velocity field in magnitude (cm/s) and direction is shown every two days for the duration of our MIT-MSEAS multi-resolution 34 day ocean forecast simulation in the 1.5 km resolution domain. The magnitude of the velocity is shown in the colorbar, and the direction of the velocity is shown by the vector arrows.

Bottom Vorticity Field

Vorticity is relevant for vehicle path planning as it highlights the circulation features, such as eddies and jets, including the finer scales and how the bottom velocity is affected by the coastline and bathymetry. The scaled vorticity is unitless, as it is scaled by the Coriolis factor [17].

In Figure 3-21, the bottom scaled vorticity is shown in the 4.5 km and 1.5 km domains of our implicit two-way nested simulations. The latter smaller domains provide higher resolutions in the coastal regions of Portugal and of the Azores Islands.

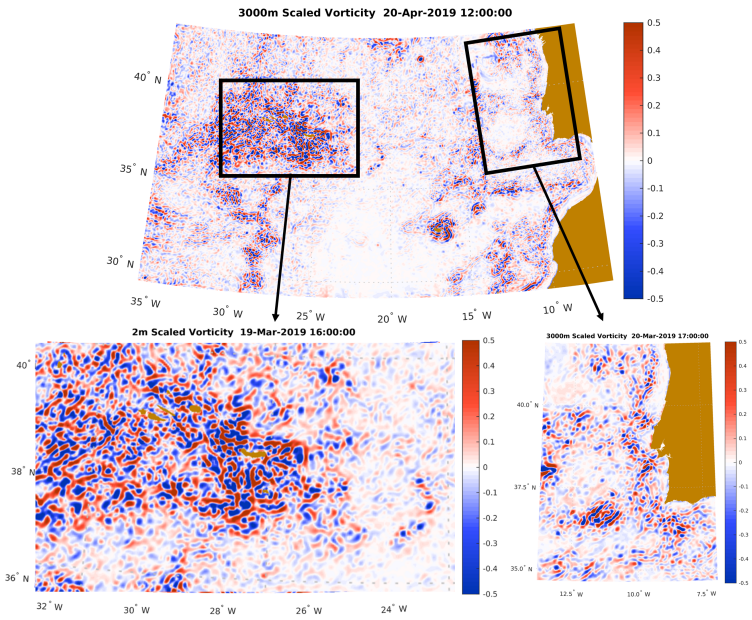

Figure 3-21: Bottom scaled vorticity in the 4.5 km domain and nested 1.5 km domain

In Figure 3-22, we show the scaled bottom vorticity as hindcast by our MIT-MSEAS multi-resolution 34 day ocean simulation in the 4.5 km resolution domain. Again, note the presence of smaller-scale features driven by the interaction between the currents, eddies, local topography, and tides. In the western half of the domain, these features are prevalent along the mid-Atlantic Ridge and the Azores. In the eastern half, the features are concentrated around Madeira Island, the seamounts and the shelf break, especially off Portugal.

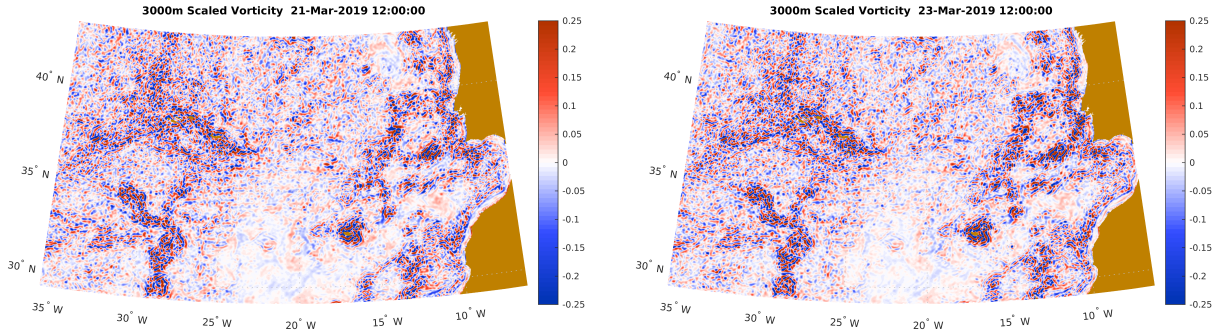

(a) March 21, 2019

(b) March 23, 2019

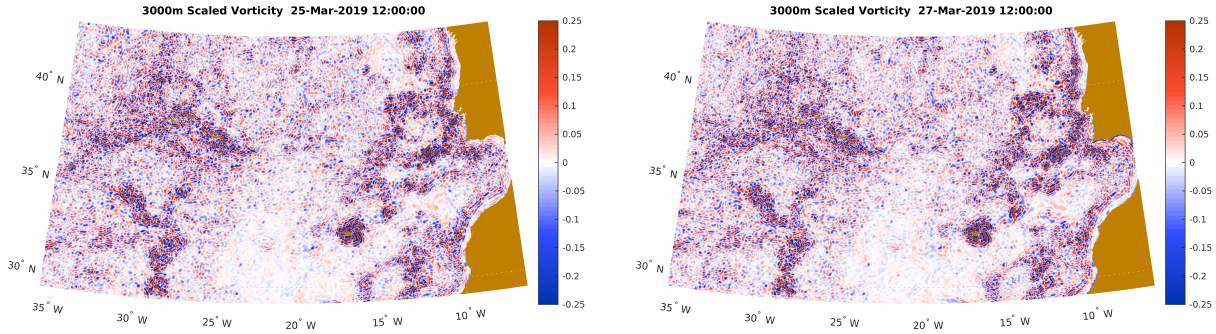

(c) March 25, 2019

(d) March 27, 2019

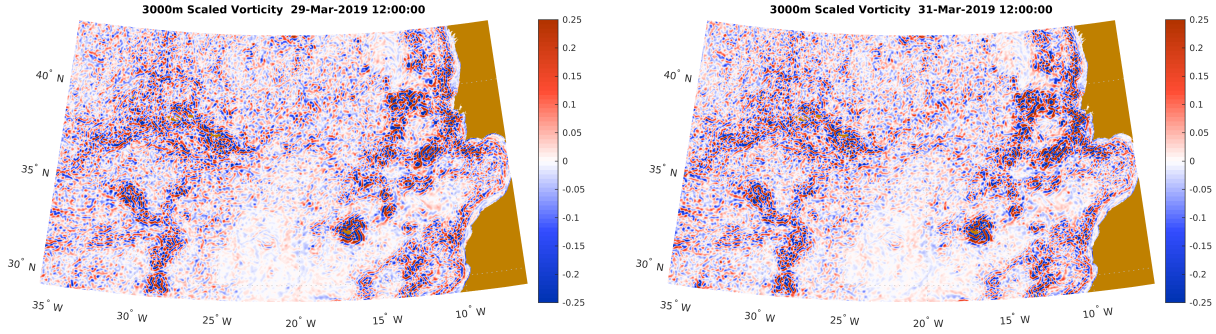

(e) March 29, 2019

(f) March 31, 2019

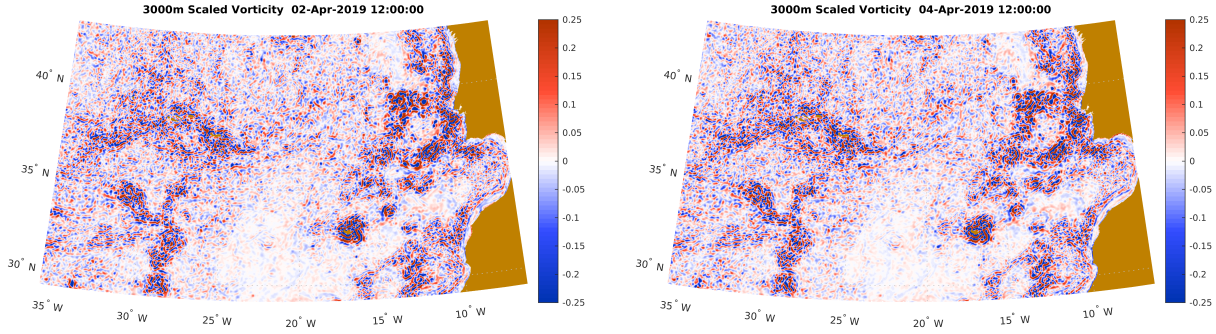

(g) April 2, 2019

(h) April 4, 2019

Figure 3-22: Bottom scaled vorticity field in magnitude every two days for the duration of our MIT-MSEAS multi-resolution 34 day ocean forecast simulation in the 4.5 km resolution domain. The magnitude of the scaled vorticity is unitless, and is shown in the colorbar (Figure Continued).

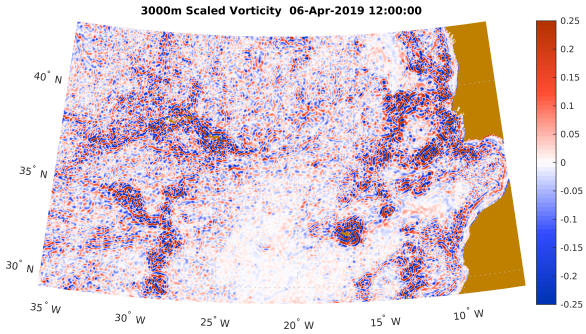

(i) April 6, 2019

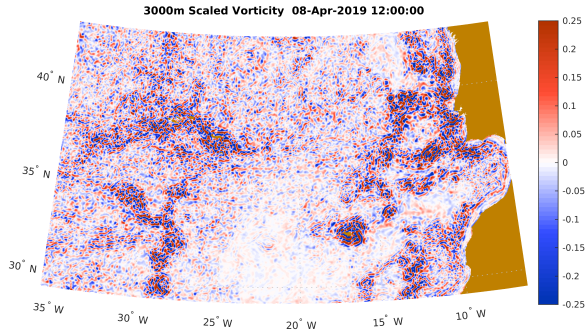

(j) April 8, 2019

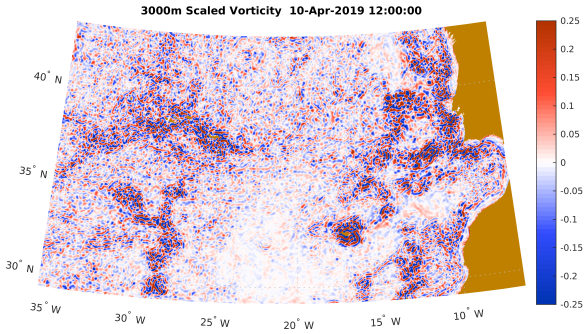

(k) April 10, 2019

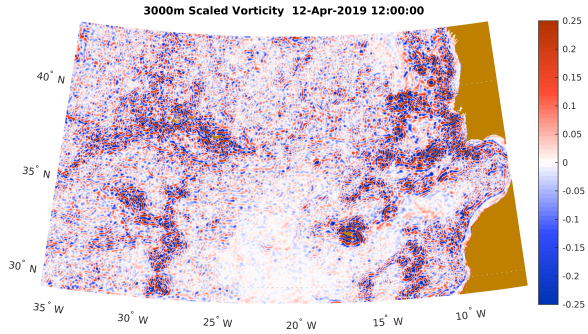

(l) April 12, 2019

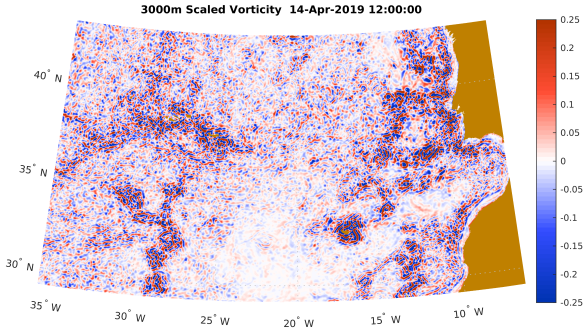

(m) April 14, 2019

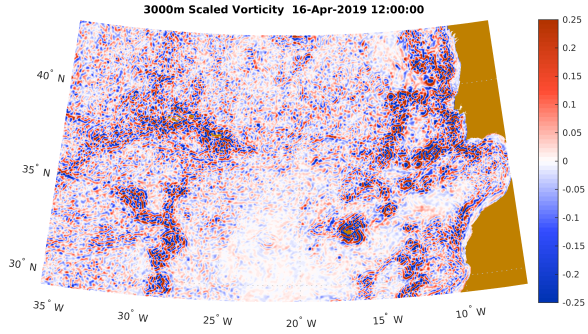

(n) April 16, 2019

Figure 3-22: Continued: Bottom scaled vorticity field in magnitude every two days for the duration of our MIT-MSEAS multi-resolution 34 day ocean forecast simulation in the 4.5 km resolution domain. The magnitude of the scaled vorticity is unitless, and is shown in the colorbar.

The bottom scaled vorticity of the 1.5 km nested domain along the coast of Portugal is shown in Figure 3-23 below, and illustrates the variability in time of the bottom vorticity fields. As described in Section 3.1.2 on ocean conditions in Portugal, there is a presence of eddies along the coastal continental shelf, which is reflected here at the

1.5 km domain. Once again, we note the presence of small-scale features along the shelf break. The vorticity of these features weakens slightly at the end of March in response to the weakening of the tidal forcing. The vorticity re-strengthens in early April following the strengthening of the tides. Note also the presence of additional detail along the shelf break that is not present in the 4.5 km simulations.

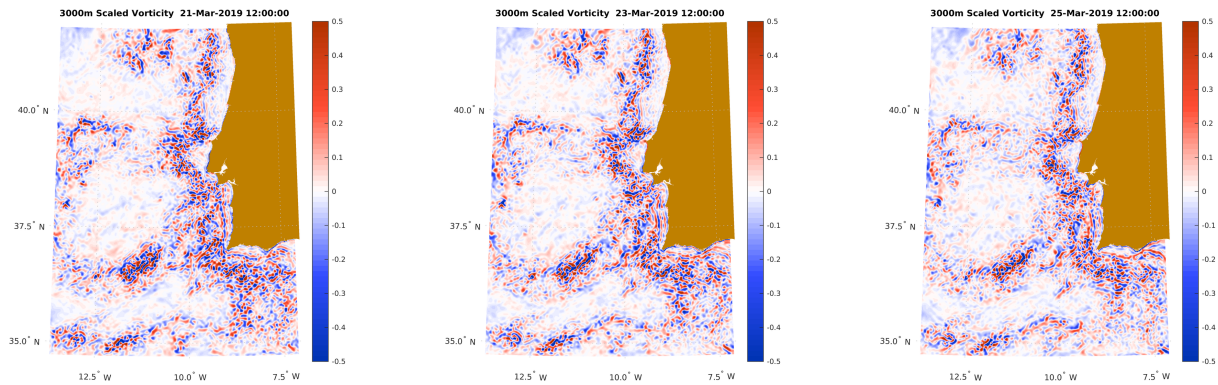

(a) March 21, 2019 *(b) March 23, 2019* *(c) March 25, 2019*

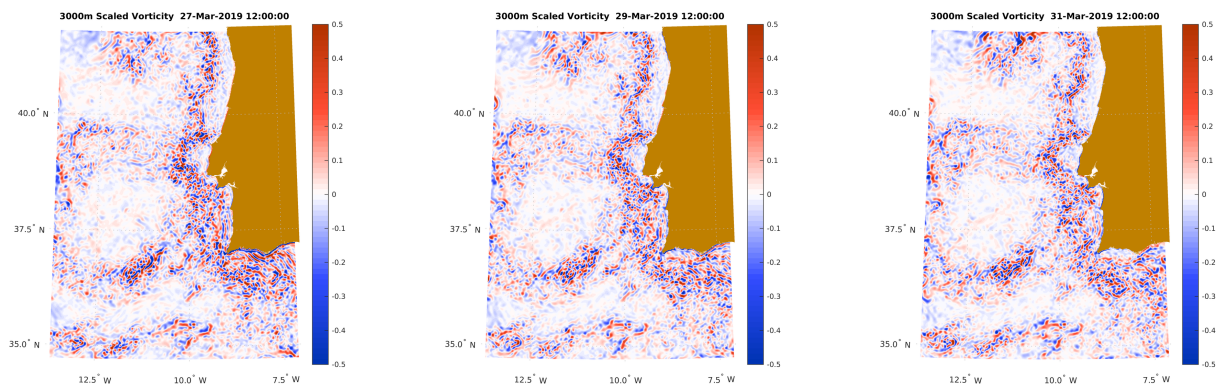

(d) March 27, 2019 *(e) March 29, 2019* *(f) March 31, 2019*

Figure 3-23: Bottom scaled vorticity field in magnitude every two days for the duration of our MIT-MSEAS multi-resolution 34 day ocean forecast simulation in the 1.5 km resolution domain. The magnitude of the scaled vorticity is unitless, and is shown in the colorbar (Figure Continued).

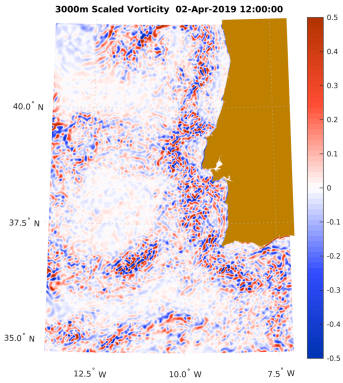

(g) April 2, 2019

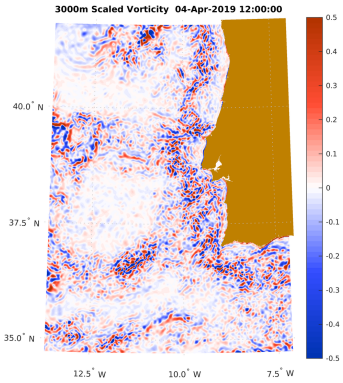

(h) April 4, 2019

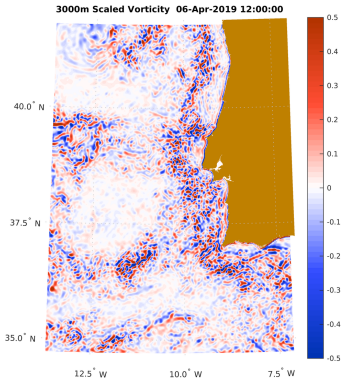

(i) April 6, 2019

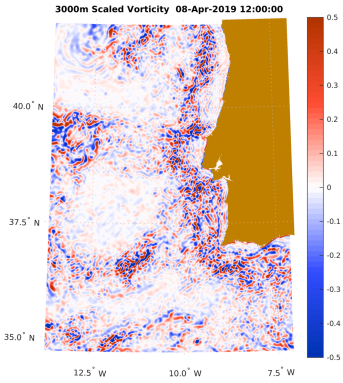

(j) April 8, 2019

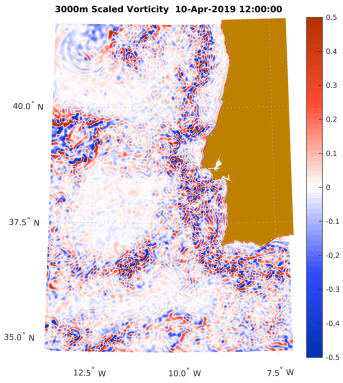

(k) April 10, 2019

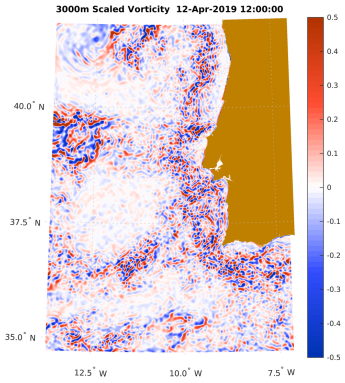

(l) April 12, 2019

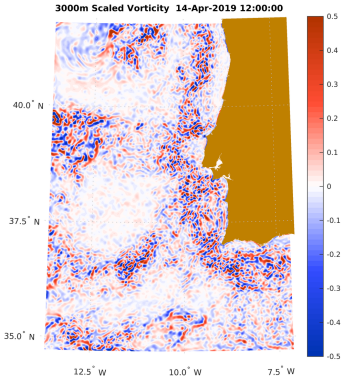

(m) April 14, 2019

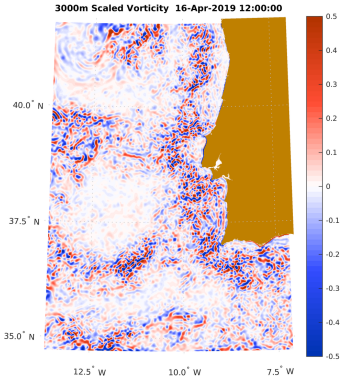

(n) April 16, 2019

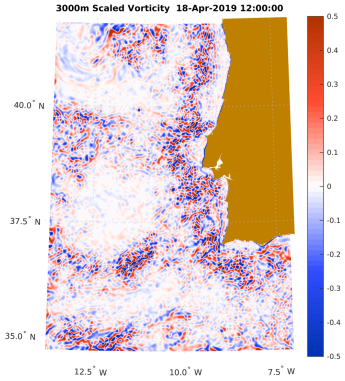

(o) April 18, 2019

Figure 3-23: Continued: Bottom scaled vorticity field in magnitude every two days for the duration of our MIT-MSEAS multi-resolution 34 day ocean forecast simulation in the 1.5 km resolution domain. The magnitude of the scaled vorticity is unitless, and is shown in the colorbar.

3.3 Autonomous Ocean Vehicles

This section contains a description of the growing importance of autonomous ocean vehicles in many applications, and their use in the Portugal-Azores-Madeira region. We also outline the autonomous underwater vehicles (AUVs) that we consider and model in this path planning study.

3.3.1 Applications and types of AUVs

The use of AUVs is now becoming prevalent and important in a wide variety of applications [83]. Applications of AUVs include scientific studies, solar-wind-wave energy harvesting, transportation and distribution of goods, naval operations, security, acoustic surveillance, communication, search and rescue, detecting marine pollution, ocean cleanup, conservation, fisheries, aquaculture, mining, ocean mapping, reducing hazards to navigation, mine-sweeping, and monitoring and forecasting [52, 53, 54]. In addition to the myriad of applications, there are also many different types of vehicles that qualify as autonomous marine vehicles. Below is a list of different vehicle types,

- Autonomous Surface Vessels
- Wave-devouring AUVs
- Subsurface AUVs
- Ocean floor AUVs
- Solar vehicles
- Floats
- Gliders
- Sailboats/saildrones
- And many more!

Each different vehicle types have different parameters, which are used to select the vehicle the most appropriate for the environment it will be deployed in, as well as its mission. The main parameters of interest include [12, 32]:

- Sensing and sampling methods

- Speed range
- Max distance and time range
- Battery capacity
- Battery recharge/discharge rate
- Method of propulsion
- Method of steering and navigation
- Max payload
- Size and weight
- Depth rating
- Dive and climb rates

In Section 3.3.3, we discuss the vehicles and parameters that we consider in this thesis.

3.3.2 AUV utilization in the Portugal-Azores-Madeira region

Portugal is renowned as an ocean-focused country. With 1794 km of coastline, which exceeds its length of land borders, and a political and commercial vantage in its proximity to the entrance of the Mediterranean Sea, Portugal has a vested interest in the exploration and utilization of the ocean environment. Modern tools for these goals are the use of autonomous and unmanned ocean vehicles. Studies by researchers in Portugal have also focused on the integration of unmanned air systems for ocean monitoring, using a mixed initiative control of unmanned air and ocean vehicles. These researchers have executed multiple operational deployments around Portugal and in ocean regions worldwide with many of these autonomous craft [19], some of which are illustrated in Figure 3-24.

Another important use of AUVs in Portugal is by the University of Porto. The Modular Autonomous Robot for Environment Sampling (MARES), is a highly maneuverable, small (1.5 m long) AUV that can dive up to 100 m, and uses controllable pitch and vertical thrusters to navigate. MARES, shown in Figure 3-25, has been used for a myriad of environmental sampling missions such as pollution monitoring, scientific data collection, sonar mapping, underwater videos, and mine countermea-

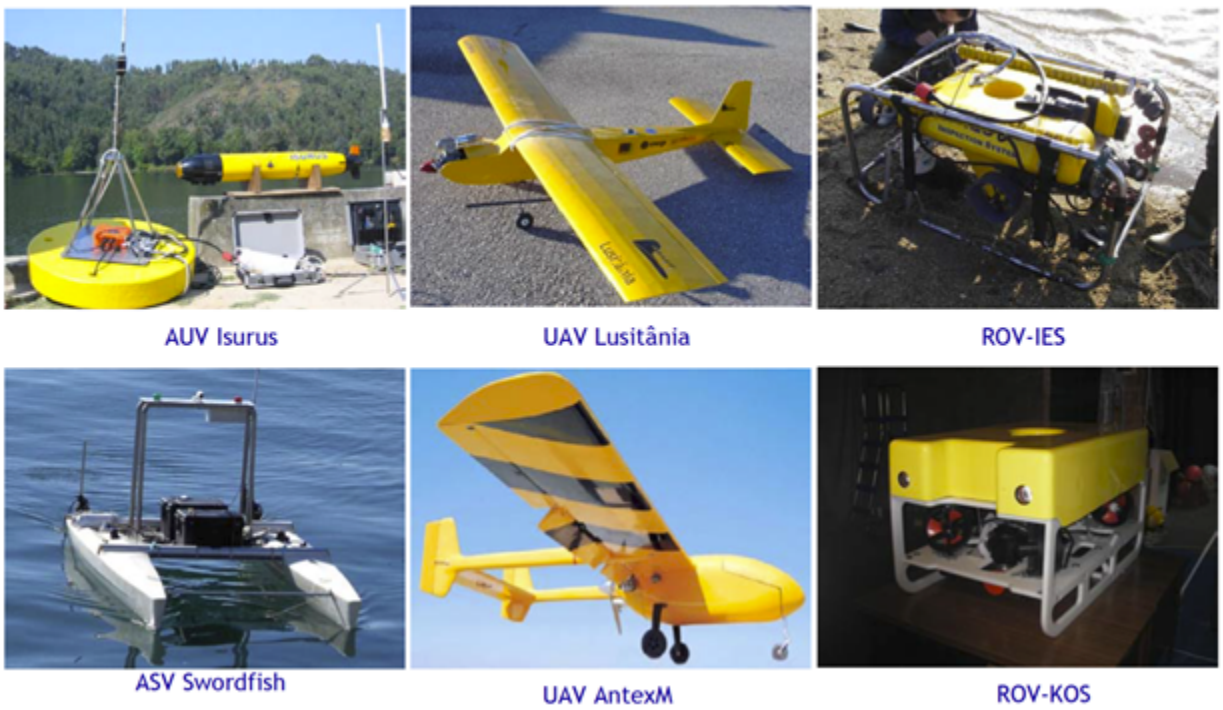

Figure 3-24: Autonomous Air and Ocean Vehicles used in Portugal and ocean regions worldwide [19].

sures. There are two main ways that the MARES is deployed. The first is to program a preset path, using the housed sensors to collect data along its trajectory. The second is to use a system of GPS enabled Navigation and Instrumentation Buoys (NIBs), which in addition to collecting their own samples for data processing and correction, also provide MARES with acoustic navigation beacons. MARES uses this system of NIBs in known locations to triangulate, allowing it to navigate, and the NIBs in turn relay the MARES location back to the mission control station. This second method allows for real-time autonomous navigation of the MARES [15].

Figure 3-25: MARES AUV [15]

Figure 3-26: ISURUS AUV [84]

Another use of AUVs in Portugal is for environmental monitoring, for example

ocean outfall monitoring. These AUVs are used to measure, map, and detect wastewater plumes, which can be harmful to the environment. The S. Jacinto outfall, located on the Aveiro coast near Porto, discharges at a rate of 0.7 m^3/sec through a diffuser of mainly industrial wastewater. In-situ measurements of this outfall can be provided by AUVs, with a sampling strategy guided by model predictions of the plume characteristics. This sampling strategy was best matched with the Isurus, as shown in Figure 3-26, which is a REMUS (Remote Environment Measuring UnitS) class AUV, and was produced by the Woods Hole Oceanographic Institution (WHOI) [84].

3.3.3 AUVs Simulated

There are many names and descriptors of ocean vehicles: unmanned craft, autonomous vehicles, autonomous ocean/marine underwater vehicles, etc. From this point on, we will refer to the vehicles used in this thesis as Autonomous Underwater Vehicles, or *AUVs*. While there are many applications and corresponding AUVs that could be utilized in the Portugal ocean region, for the purposes of this study, the parameters of the following AUVs were used in the path-planning algorithm: the REMUS 600 for simulations of surface path planning, and the MBARI AUV for simulations of deep and bottom path planning.

REMUS 600

The REMUS 600 is one of the REMUS AUVs used by WHOI [32]. It is versatile, with a modular design that allows it to reconfigure its sensors, allowing for it to be used in many different mission types. It hosts a Small Synthetic Aperture Minehunter for imaging at high resolution. This AUV is also perfect for long-range missions, being able to operate for 70 hours, dive up to 600 meters, and travel at speeds up to 5 knots at the surface, making it an optimal AUV model for the surface runs in this study [32]. The REMUS 600, shown in Figure 3-27, has also been used for past MSEAS real-time sea exercises [97].

Figure 3-27: Surface craft: REMUS 600 [32].

MBARI

The Monterey Bay Aquarium Research Institute's (MBARI) uses the MBARI Dorado class AUV, which is primarily used for mapping the ocean floor at high resolutions. This AUV also has a modular design, and operates at a speed of less than 1.5 meters per second (3 knots) and can dive to 6,000 meters [73]. The MBARI AUV, shown in Figure 3-28, houses multibeam, multifrequency sonars and bottom profilers [12, 73], making it an optimal AUV model for the deep and bottom runs simulations in this study.

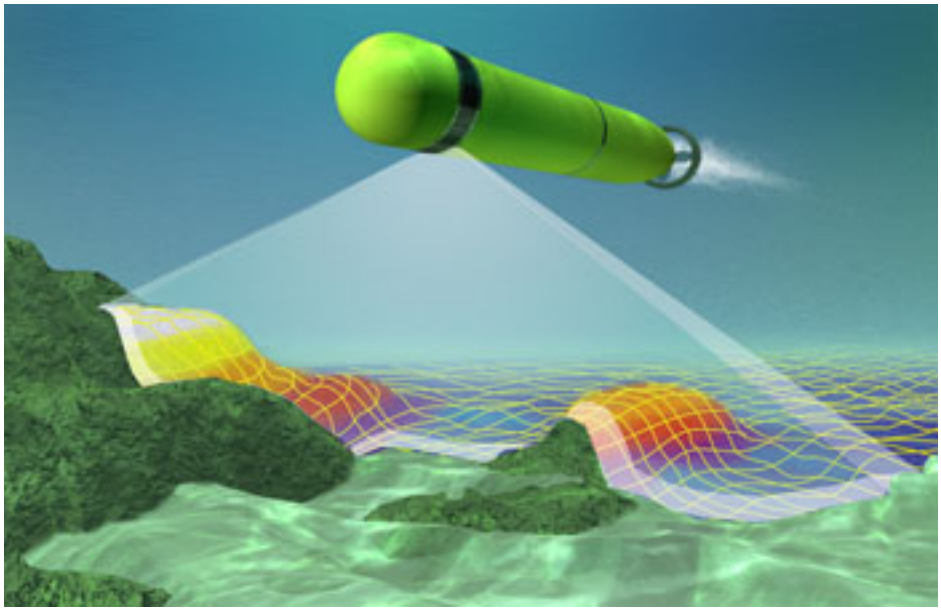

Figure 3-28: Bottom craft: MBARI Dorado AUV [73]

Since the parameters of these two AUVs fit the constraints of the surface and bottom path planning, the only variable parameter to select is speed. Due to the

low operating speeds of both of these vehicles, the time-optimal path planning was modelled after the AUVs travelling at either 0.5 m/s (∼1 knot) for slow operating speed, or 1.5 m/s (∼3 knots) for faster operating speed. Slower speeds are favorable for AUVs as this reduces energy use, minimizes forward drag, and extends battery usage [42]. For this study, low operating speeds are also favorable as they will show larger variations in the optimal path due to interactions with the ocean flow-field, as slower vehicles are more sensitive to ocean dynamic effects, and faster vehicles will have smoother and more direct paths.

Both of these AUVs have other specific parameters, such as vehicle weight, drag, and thrust consistency, that are not explicitly considered by our path planning simulations because we are interested in planning for spatial scales much larger than the size of the AUVs. Hence, our methods are based on an AUV that is a point moving at an effective speed that implicitly accounts for these operational properties of the vehicles [68, 66, 62, 61, 64]. The exact parameters used in the simulations completed in this thesis are outlined in Chapter 5.

Chapter 4

Theory & Methods

This chapter outlines the theory and methods that we employ for exact planning optimal paths for autonomous vehicles. First, we review path planning of autonomous marine vessels including different methods that have been used. Then, we describe the methodology used in this time-optimal path planning case.

4.1 Prior Path Planning Results

4.1.1 Path Planning of Autonomous Marine Vessels

While the design and build of an autonomous vehicle or robot is a complex engineering feat on its own, the task of computing its navigational path can be just as complicated. The capabilities of the vehicle, the dynamic environment it operates in, and the various parameters of its mission lead to multiple different methods of path planning. Since these vehicles are autonomous, the creation of their optimal paths must be calculated using many factors. This science of autonomy can be defined as the "systematic development of fundamental knowledge about autonomous decision-making and task completing in the form of testable autonomous methods, models, and systems" [53]. Since these autonomous vehicles operate in the ocean, the theory used must focus on optimizing algorithms within a strong and dynamic environment, and take into account the vehicle's interaction with its environment [68, 69]. The

next consideration for path planning is deciding what aspect of the mission must be optimized by computing the path panning. The performance of AUVs is usually optimized in the following factors: a) travel time; b) energy used; 3) safety of vehicle; 4) coordination with other vehicles; 5) sampling capabilities; [68, 61, 53]. Because ocean vehicles often operate in missions that are of long duration when compared to the capacities of the vehicles, minimizing time (and energy) often take precedence in the path optimization [68]. Additional challenges are posed by the environment, which delineates an infinite number of control choices and involves movement from a pervasive flow field [66, 60].

4.1.2 Path Planning Methods

There is not a universal method for vehicle path planning, due to both the large scope of path planing applications, as well as the varying goals achieved in each different case. This section summarizes different path planning methods that are used. We also refer to [58] for more details.

For motion control of a robot with multiple degrees of freedom, path planning is reduced to motion planning [11, 39], which can have a higher level of planning by using either methods of cooperative control [78, 43] or coordination [18, 3]. These methods have been studied largely for robotic arms. In the case of path planning for robots in unsteady flows, there are fewer studies due to difficulties in variable movements costs due to the interaction of the vehicle with the dynamic environment [33, 66].

For path planning for vehicles, another method discussed is a heuristic search scheme called Rapidly exploring Random Trees (RRTs). This method uses a randomized path planning algorithm with the purpose of avoiding obstacles within the domain, and is adapted to high dimensionality and many degrees of freedom, as seen in Figure 4-1 below [41]. This method has been used for path planning of ocean vehicles [102, 69]. The main disadvantage of RTT is due to the probabilistic nature of the algorithm, which favors a local extreme over a globally optimal generated path [68, 8]. Due to this limitation, RRTs cannot be used as the main path planning algorithm for

highly dynamic environments.

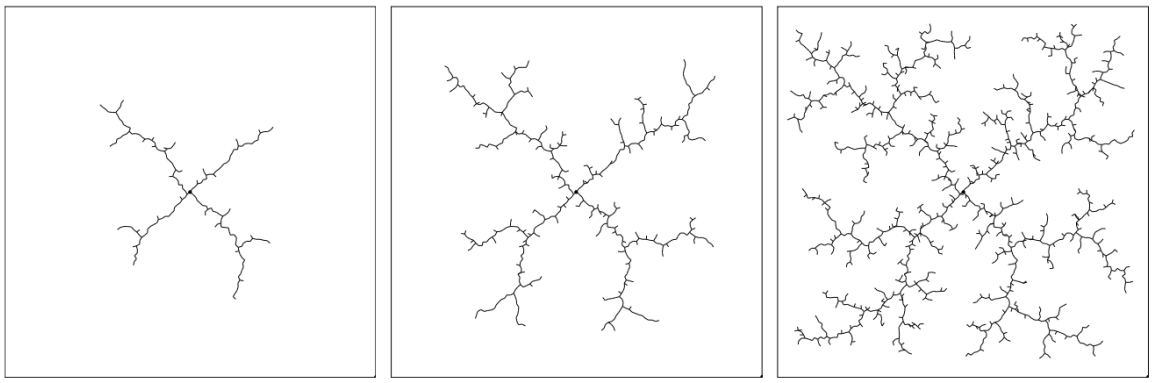

Figure 4-1: RRT from a start point at the center of the domain, through three stages of growth (adapted from [41, 8])

Another heuristic search scheme, called the A* approach, is a graph search algorithm to create a path free of obstacles, discretizing the navigable domain into continuous cells. This method has been used in AUV path planning [87, 86]. The method is illustrated in Figure 4-2 below, and shows a discretization of the domain [68, 80].

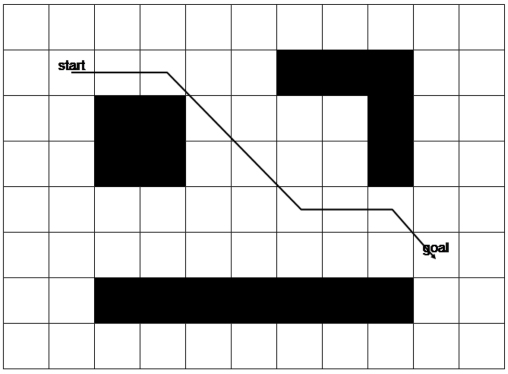

Figure 4-2: Uniform discretization of a continuous robot workspace into cells, where the robot can travel to any empty cell on its path from start to finish, avoiding the obstacles represented by the black cells [58]

The A* method is an extension of Dijkstra's algorithm, which finds the shortest path between two nodes on a graph, and is commonly used in discrete path planning [40]. The main disadvantage of the A* algorithm is that there is ambiguity in defining the choice of a heuristic. This method is better used in a simple constant flow, as there will be a loss of optimality in complex ocean flows [86, 54, 59]. The D*

algorithm is modeled from the A* algorithm, and adapted to allow variations in the cost parameters to prevent the limitations the A* algorithm experiences when applied to flow fields [94, 80]. The D* also has limitations, as it determines infeasible paths which will create high costs [35]. Other approaches that have been used for AUV path planning include fast marching algorithms [82], swarm optimization [105], VISIR ("discoVerIng Safe and effIcient Routes"), a dependent version of Dijkstra's algorithm [69], nonlinear trajectory generation [106], and genetic algorithms [2].

Due to the dynamic complexity of path planning in highly dynamic ocean flow fields, many of these described methods will either fail or be too expensive to apply to AUV path planning, preventing them from being used for accurate real-time applications. In the next section, we will discuss an exact PDE based scheme that is valid for any sufficiently smooth flow field and will thus be utilized for this study.

4.2 Time-Optimal Path Planning: Governing Equations and Numerical Schemes

This thesis focuses on the prediction of time-optimal paths within a dynamic ocean flow field. Time-optimal path planning is governed by a Hamilton-Jacobi-Bellman PDE. To solve for this exact time-optimal PDE and obtain the corresponding globally optimal paths in continuous, strong and dynamic ocean environments, we employ the MSEAS level set and backtracking method [68, 59, 67, 54, 8, 22, 21].

Utilizing the MSEAS-PE multi-resolution ocean modelling system, we use a non-dimensional form of the Hamilton-Jacobi-Bellman level set equation [61, 38] for optimal path planning in a realistic ocean scenario. From these level set equations, a reachable set of points is determined with numerical consistency from a discrete forward evolution of the reachable set and discrete backward tracing to get an optimal path. The notation used throughout this section is defined in Table 4.1 below.

Next, we summarize the theory and numerical schemes for the path planning equations. All of these results are described in [68, 59, 67, 54, 8, 22].

Notation	Definition
d	The number of spatial dimensions
$\boldsymbol{x}$	Spatial variable
t	Time variable
t_i	Initial time
t_f	final optimal arrival time
$\boldsymbol{x}_s$	Position of the start point
$\boldsymbol{x}_f$	Position of the target
$\boldsymbol{X_p}$	Position of the vehicle
$\boldsymbol{p}$	The trajectory of the vehicle
$\boldsymbol{V}$	Background velocity
F	Relative speed of the vehicle
F_{max}	Maximum relative speed of the vehicle
$\hat{\boldsymbol{h}}(t)$	Heading of vehicle

Table 4.1: Notation Definitions

Problem Statement

We consider an AUV that completes a journey from a start point, $\boldsymbol{x}_s$, to an endpoint $\boldsymbol{x}_f$. This vehicle navigates through an external dynamic ocean flow field $\boldsymbol{V}(\boldsymbol{x}, t)$ defined in the physical domain Ω, where $\Omega \subseteq \mathbb{R}^d$, and is treated as a point particle. The AUV aims to optimize the time spent on the journey, as shown in Figure 4-3.

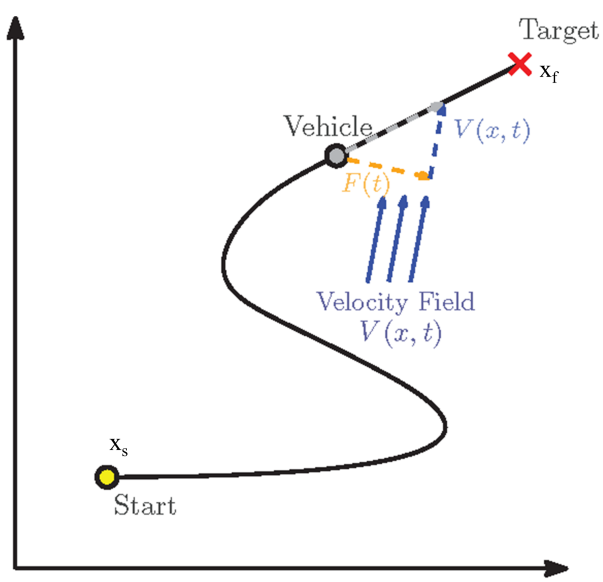

Figure 4-3: Visualization of the time-optimal path planning problem (adapted from [68])

Assumptions

The following are the base assumptions that are made in this study:

1. The ocean flow-field $\boldsymbol{V}(\boldsymbol{x}, t)$ is exactly known. While ocean flow-fields are uncertain in real life, we simplify the case with the assumption that the MSEAS-PE model is accurate and the flow-fields exact and known. For accounting for uncertainty and to minimize risks, we refer to [98, 99].

2. The AUV is assumed to be a point particle, given the scales of the vehicle size compared to these of the ocean flow fields. While the distance travelled by the AUV is much larger than its own size, the goal of this study is to compute globally optimal long-distance trajectories, $\boldsymbol{p}$. As a point particle, the vehicle does not have inertia, and therefore the interaction between the AUV and the ocean flow-field is purely kinematic.

3. The trajectory of the AUV is continuous [58, 20].

Before a path is planned, the control parameters for the vehicle must be acknowledged. There are two ways to control a vehicle: speed and direction. The first control of the AUV is its relative speed compared to the background flow-field. The maximum speed of the vehicle in a still, no-flow field is represented by F_{max}, and the relative speed of the vehicle with respect to the flow-field at a given time t is represented by $F(t) \in \mathbb{R} \cap [0, F_{max}]$. The second control of the AUV is its heading, which is the direction of relative velocity or propulsion by the AUV. It is represented by a unit vector: $\hat{\boldsymbol{h}}(t) \in S^{d-1}$ [20]. Equation 4.1 shows this relationship between the particle net velocity of the AUV, the background velocity of the flow-field, and the AUV's relative velocity.

$$\overbrace{\frac{\mathrm{d}\boldsymbol{X_p}}{\mathrm{d}t}}^{\text{Net velocity}} = \overbrace{\boldsymbol{V}\left(\boldsymbol{X_p}(t), t\right)}^{\text{Background Velocity}} + \overbrace{F(t)\hat{\boldsymbol{h}}(t)}^{\text{Relative velocity}} \tag{4.1}$$

Now that the control parameters and motion of the AUV is defined, let's review the theory and schemes for time-optimal path planning.

4.2.1 Reachability

The *reachable set* is the set of all points that can be reached from a given starting point within a given time. The reachable set is governed by the Hamilton-Jacobi PDE. The first time when the reachable set reaches the final destination is the minimum travel time between the start position and final destination [67, 38, 21]. The boundary of the reachable set is called the *reachability front*, and it contains all of the points in space that can be traveled to within the corresponding time. By tracking the reachability front, we can obtain the optimal path, as it will be the path traced by the point on the reachability front that reaches the target first [58].

The reachability set and front is illustrated in Figure 4-4.

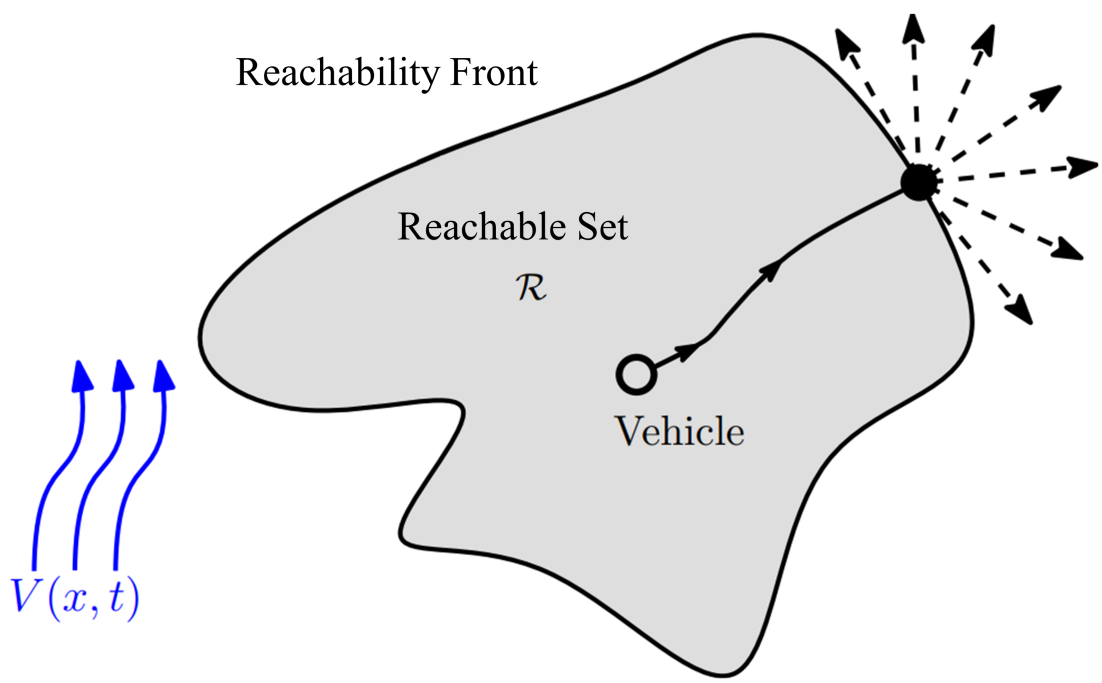

Figure 4-4: Reachable set, $\mathcal{R}$, Reachability Front, and infinite possible vehicle heading directions (adapted from [66]).

The reachable set is represented by $\mathcal{R}(\boldsymbol{x}_s, t)$, dependent on time by t, and starting position by $\boldsymbol{x}_s$. This reachable set $\mathcal{R}(\boldsymbol{x}_s, t)$ contains all of the possible points that make up all possible trajectories, $\boldsymbol{p}$, from the start point $\boldsymbol{x}_s$, where $\boldsymbol{p}(t) \in \mathcal{S}_{[0,t]}(\boldsymbol{x}_s)$

[58]. This relationship is delineated in Equation 4.2:

$$\mathcal{R}(\boldsymbol{x}_s, t) = \boldsymbol{p} : \boldsymbol{p} \in \mathcal{S}_{[0,t]}(\boldsymbol{x}_s), \tau \in [0, t]\} \tag{4.2}$$

The set of all of these executable trajectories must also satisfy $\boldsymbol{p}(t = 0) = \boldsymbol{x}_s$ [25]. Within this set of all executable trajectories that satisfy these requirements, there is an infinite number of paths from the start point $\boldsymbol{x}_s$ to the leading edge of the reachability front.

From this understanding of the reachable set and front, we can develop a time-optimal path through a background dynamic flow-field. This will be solved using a level set method [58].

4.2.2 Forward Solve with Level Sets

The first step is to solve the forward reachability PDE using the level set method. The forward solve of the reachability front is a *level set*, as it is the set of all points that can be reached within the given amount of time. The first level set, the zero level-set contour, defines the reachability front, and is when $\phi(\boldsymbol{x}, t) = 0$ [58, 97].

This level set, or reachability front $\mathcal{R}(\boldsymbol{x}_s, t)$ as previously defined, will be evolved by solving the Hamilton–Jacobi Equation forward in time, as shown in Equation 4.3 for $\phi(\boldsymbol{x}, t)$:

$$\frac{\partial \phi(\mathbf{x}, t)}{\partial t} + F|\nabla \phi(\mathbf{x}, t)| + \mathbf{V}(\mathbf{x}, t) \cdot \nabla \phi(\mathbf{x}, t) = 0 \tag{4.3}$$

The function ϕ is started from the origin, at $\boldsymbol{x}_s = 0$. The initial conditions for ϕ are:

$$\phi(\boldsymbol{x}, t = 0) = \|\boldsymbol{x} - \boldsymbol{x}_s\| \tag{4.4}$$

and open boundary conditions are discussed in [58, 66, 37, 38].

The evolution of the reachability front can then be computed by solving an initial value PDE that governs the evolution of the level set function $\phi(\boldsymbol{x}, t)$. The solution $\phi(\boldsymbol{x}, t)$ of the PDE in Equation 4.3 will provide the zero-level set contour, that is the

reachability front of the AUV starting at $\boldsymbol{x}_s$ at any time $t > 0$. The evolution of this reachability front contains the present locations of all possible trajectories, $\mathcal{R}(\boldsymbol{x}_s, t)$, from the starting point $\boldsymbol{x}_s$ to any destination points. With the forward solve from start $\boldsymbol{x}_s$ to destination $\boldsymbol{x}_f$, the final optimal arrival time of the vehicle t_f is the first time t when the level sets reach the destination, and $\phi(\boldsymbol{x}, t) = 0$ [58, 97].

Figures 4-5 and 4-6 sketch these levels sets in a hypothetical domain. In Figure 4-5, the AUV has smooth levels sets showing the reachability in the case of no background ocean dynamics, so they are circles. In Figure 4-6, the AUV has curved and irregular level sets and reachability fronts that differ from a circle due to the effects of the background ocean flow field.

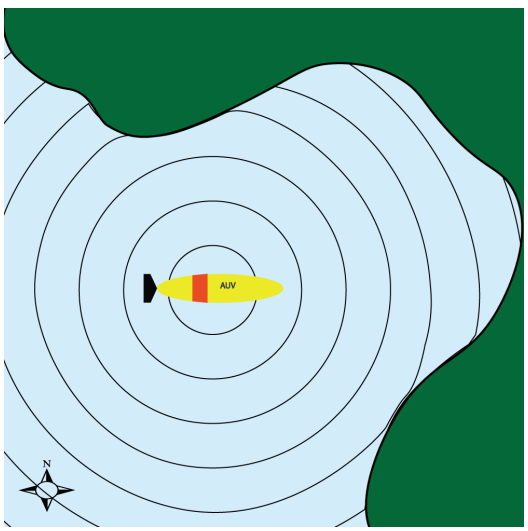

Figure 4-5: Reachable set, without ocean flows.

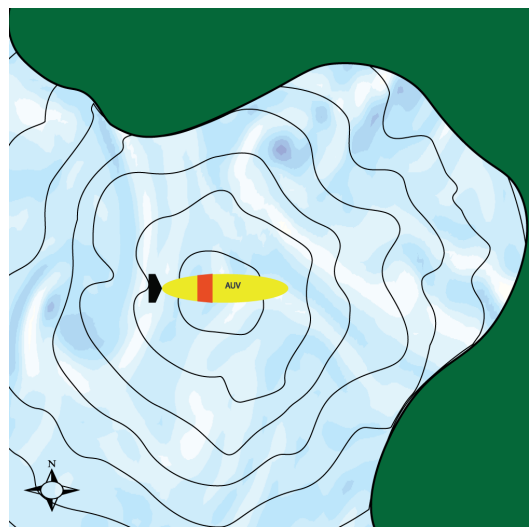

Figure 4-6: Reachable set, with ocean flows.

Figures 4-7 and 4-8 show such levels sets in the Portugal domain used in this study. In Figure 4-7, forward propagation has started with expanding level sets. In Figure 4-8, the forward solve finishes as the zero level set (reachability front) reaches the final destination location. Mathematically, the final optimal arrival time t_f is reached when $\phi(\boldsymbol{x}_f, t) = 0$. Since this case uses the flow field of the background ocean dynamics, it is clear that the level sets are curved and varying due to dynamic reachability as the AUV is advected by the background ocean currents.

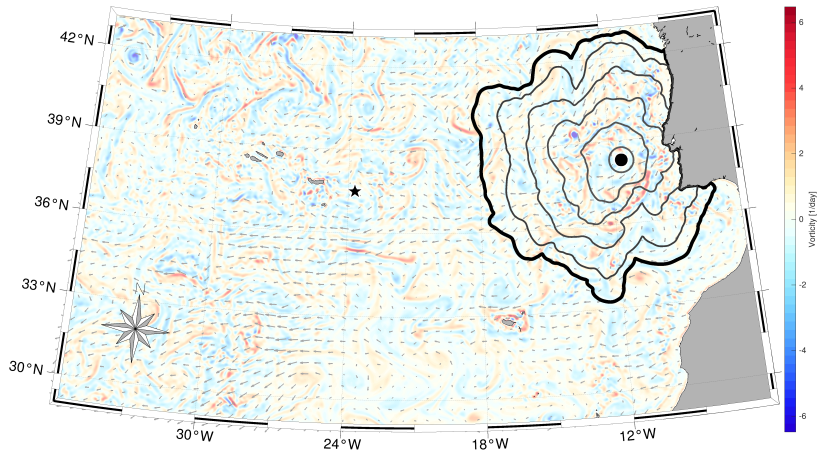

Figure 4-7: Level sets, expanding from Lisbon towards final destination of Azores. Thick black curve is reachability front, plotted against scaled vorticity of surface flow.

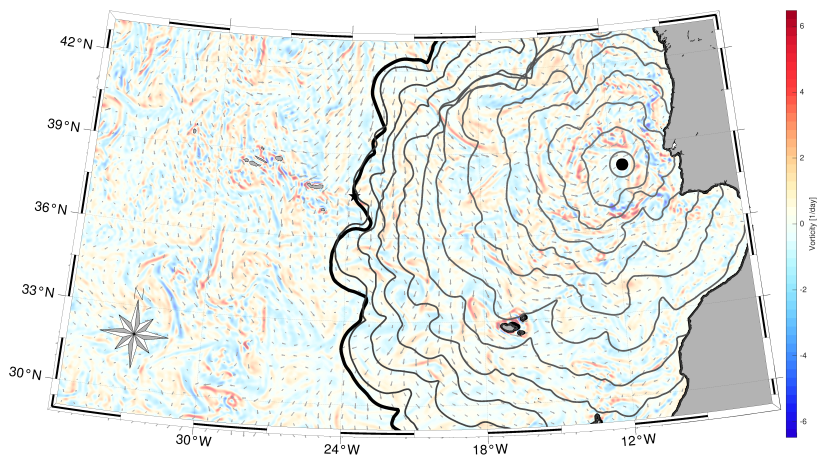

Figure 4-8: Level sets from Lisbon to Azores, final destination reached. Thick black curve is reachability front, plotted against scaled vorticity of surface flow.

4.2.3 Backtracking

Backward vehicle tracking occurs after the reachability front reaches the final destination $\boldsymbol{x}_f$. The optimal vehicle trajectory and controls are computed by solving the trajectory ordinary differential equation backwards in time [68, 65].

Once the level set of the reachability front reaches the target destination, $\boldsymbol{x}_f$, backtracking is used to the original starting point, $\boldsymbol{x}_s$, extracting a final time-optimal path $\boldsymbol{X}_P^*$. Assuming that ϕ is differentiable, the particle backtracking equation is

used to trace the time-optimal path, $\boldsymbol{X}_P^*(\boldsymbol{x}_s, t)$, in Equation 4.5 [58, 97]:

$$\frac{\mathrm{d}\boldsymbol{X}_P^*(\boldsymbol{x}_s, t)}{\mathrm{d}t} = -\boldsymbol{V}(\boldsymbol{X}_P^*(\boldsymbol{x}_s, t), t) - F\frac{\nabla\phi(\ X(\boldsymbol{x}_s, t), t)}{|\nabla\phi(\boldsymbol{X}_P^*(\boldsymbol{x}_s, t), t)|} \tag{4.5}$$

Equation 4.5 is integrated backward in time starting from the target point at $\boldsymbol{x} = \boldsymbol{x}_f$ when the final optimal path time is reached at $t = t_f$. This will result in $\boldsymbol{X}_P^*(\boldsymbol{x}_s, t)$, the time-optimal path through a dynamic ocean region with background velocity flow-fields of $\boldsymbol{V}(\boldsymbol{x}, t)$ [58, 97]. Equation 4.6 shows that following the final time-optimal path, a function of the start point $\boldsymbol{x}_s$, time t, and final optimal time t_f, will result in the vehicle arriving at the final point, $\boldsymbol{x}_f$:

$$\boldsymbol{X}_P^*(\boldsymbol{x}_s, t, t_f(\boldsymbol{x}_f : \boldsymbol{x}_s)) = \boldsymbol{x}_f \tag{4.6}$$

Figure 4-9 illustrates this backtracking in the Portugal domain (at different time steps) used in this study. As the forward propagating level sets reaches the final destination $\boldsymbol{x}_f$, it is stopped, and the backtracking is started, integrating backward in time across the level sets to the starting position, in the direction orthogonal to the local level sets.

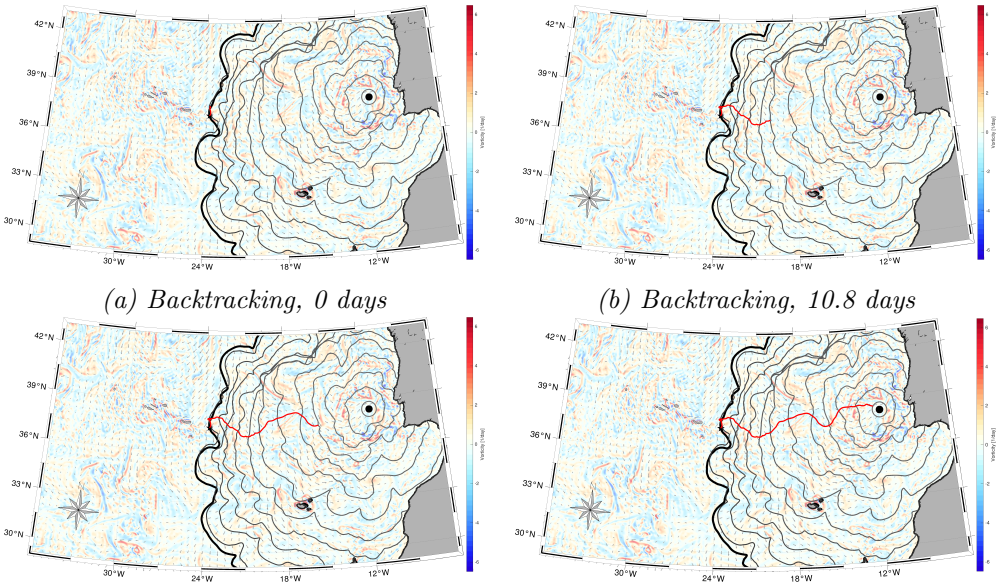

(a) Backtracking, 0 days

(b) Backtracking, 10.8 days

(c) Backtracking, 16.2 days

(d) Backtracking, 23.4 days, complete

Figure 4-9: Backtracking to from final destination to start point to yield optimal path.

4.2.4 Implementation

Using this path-planning methodology, paired with the MSEAS-PE modeling system to hindcast the ocean flow field $V(\boldsymbol{x}, t)$, we can predict time-optimal paths between points. The following parameters are the inputs used for each path, including a description of how they are used.

Parameters	Description
dims	Number of dimensions of the physical domain. For this study, we used 2
dt	Time step
t_i	Initial Start time of vehicle
depth	Depth, out of 100 levels
$\boldsymbol{x}_s$	Position of the start point, in latitude and longitude
$\boldsymbol{x}_f$	Position of the destination point, in latitude and longitude
Speed	Constant speed of the vehicle, in meters/sec
$\boldsymbol{V}(\boldsymbol{x}, t)$	Velocity flow-field, using the MSEAS-PE model
ir	Initial radius of the reachability front sphere to use, in meters

Table 4.2: Input Parameters

Each of the cases used in Chapter 5 will have their own case parameter values.

Chapter 5

Portugal-Azores-Madeira Applications

This chapter presents the results of applying the MIT-MSEAS time-optimal path planning algorithm in the Portugal-Azores-Madeira Ocean Region. Different cases and AUV missions are simulated for different input parameters. In each of these mission cases, there is a discussion of how the ocean dynamics and background flow field affects the time-optimal path. The effect of this flow field can be seen by examining the level set reachability front. The final result will be a final time-optimal path from the starting point to the destination, that uses our time-optimal path planning methodology, with the environmental velocities, $\boldsymbol{V}(\boldsymbol{x}, t)$, provided by our MSEAS-PE forecasting system.

5.1 Summary of Mission Types

To illustrate our time-optimal path planning method and framework in the region, multiple mission cases were created to compare the optimal journeys from different locations and with different goals. Below is a summary of the mission types used that will be discussed in this chapter:

1. Zero flow-field case
2. Individual point-to-point case

3. Multi-end point, one start point case
4. Multi-start point, one end point case
5. Bottom Paths
6. Intercept case
7. Arrival Time Fields Case

Furthermore, for the cases of the individual point-to point missions, a comparison study was done on the effect of the following factors on the optimal path:

1. Vehicle Speed
2. Path Direction
3. Start Time

5.2 Zero Flow-Field

In the "No Flow-Field Case" or "Zero Flow-Field Case" mission, the ocean dynamics and background flow-field are assumed to be zero. This gives a baseline for an estimate of travel times between points, based on the speed of the vehicle. It can also be directly computed by our schemes, simply by setting the background flow fields to zero [71, 97].

The total time for an AUV to travel from its start to its destination point can be determined with the simple $time = \frac{distance}{speed}$ calculation. As shown in Figure 5-1, the total time of the AUV's journey is dependent on the speed of the vehicle. With the zero-flow field, the vehicle propulsion speed will be equal to the relative speed of the vehicle, F, since there is no background velocity flow-fields $\boldsymbol{V}(\boldsymbol{x}, t)$ present. The figure shows a line to represent each of the 10 journeys with their total distance (in nautical miles), and the direct relationship between the vehicle's speed (in knots) and the time it will take to complete the journey (in days).

While the method for computing optimal paths in the zero flow-field case is the same as the method for the flow-field cases, the input parameters will be different, particularly the input of the velocity flow-field, $\boldsymbol{V}(\boldsymbol{x}, t)$, as shown in Table 5.1. For a description of each of these parameters, see Table 4.2.

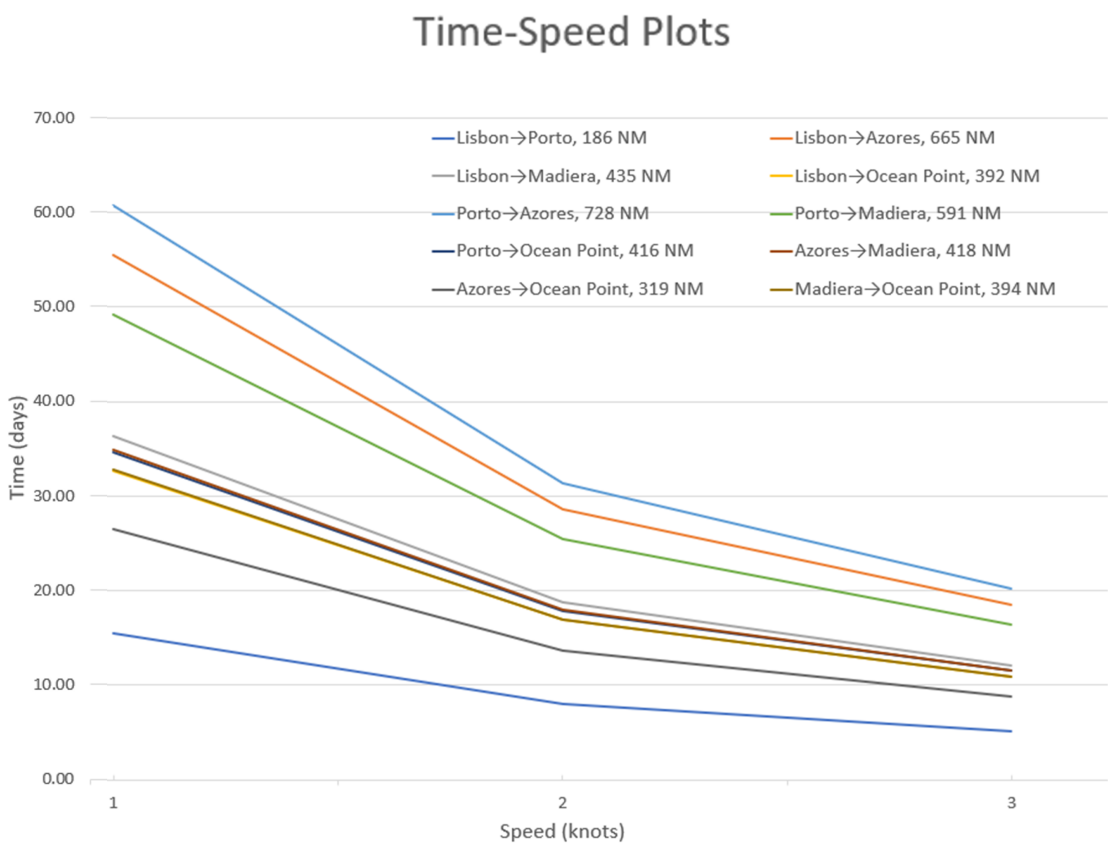

Figure 5-1: Time to reach destination vs vehicle speed for zero flow-field case

Parameters	Value
dims	2
dt	1,000 sec
t_i	0.0 sec
depth	2nd vertical level (surface)
$\boldsymbol{x}_s$	Lisbon: 38.0° N, 10.0° W
$\boldsymbol{x}_f$	Azores: 37.5° N, 24.0° W
Speed	0.5 meters/sec
$\boldsymbol{V}(\boldsymbol{x}, t)$	0 velocity flow-field
ir	50,000 meters

Table 5.1: Zero flow-field case input parameters

For path planning in the zero flow-field state, the reachability front will be smooth, as illustrated in Figure 5-2, and the final optimal path will be a great circle line (the largest possible circle that can be drawn around a sphere) as it follows the curve of the earth between the two points, as illustrated in Figure 5-3. The final time-optimal path will be the same regardless of the direction or start time of the vehicle, since there is no ocean dynamics that will affect the vehicle. Landmasses, such as islands, will affect the reachability front as they contain points where the vehicle cannot travel, as they are ocean vehicles and not hybrid land vehicles. Therefore, these points are not included in the reachable set, and the reachability front will wrap *around* these islands and create "dents" in the front as they continue to propagate towards the final destination [61].

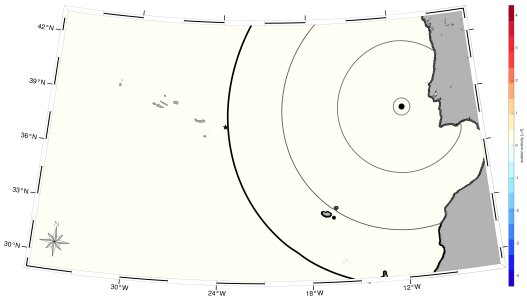

Figure 5-2: Zero flow-field case, final reachability Level Set for run from Lisbon to Azores. The plot background is the unitless surface scaled vorticity. The magnitude of the vorticity is shown in the colorbar, and is zero since there is no flow-field present.

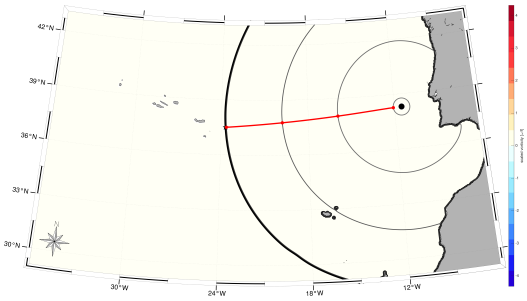

Figure 5-3: Zero flow-field case, final reachability Level Set for run from Lisbon to Azores. The plot background is the unitless surface scaled vorticity. The magnitude of the vorticity is shown in the colorbar, and is zero since there is no flow-field present.

In this Figure 5-4, multiple comparisons are made for the final path of a vehicle in a field with no ocean dynamics present, vs one with ocean dynamics present. As seen by the final arrival times, the direct, no-flow path differs from the path where the environmental velocity flow field $\boldsymbol{V}(\boldsymbol{x}, t)$ is present and non-zero. The no-flow case will be faster than the flow-field case if there are sufficiently adverse currents present in the environmental flow field that would slow down or stop the AUV. The no-flow case will be slower than the flow-field case if there are favorable currents that propel the AUV toward its destination.

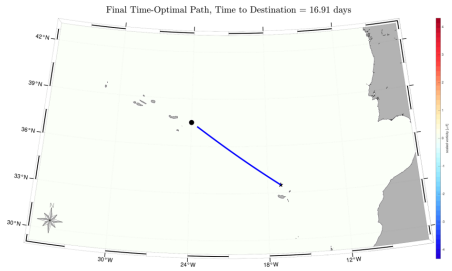

(a) Azores to Madiera

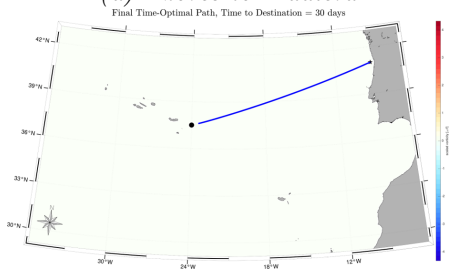

(b) Azores to Porto

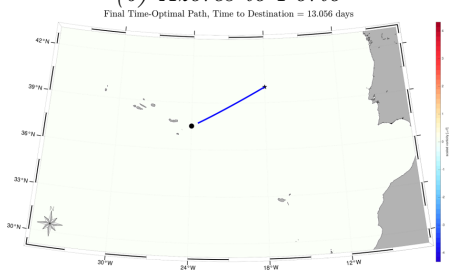

(c) Azores to Ocean Midpoint

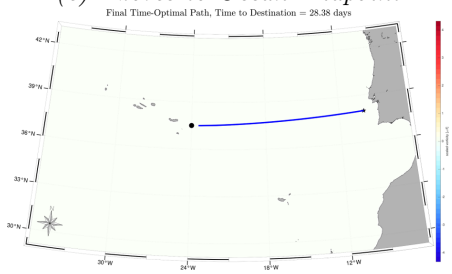

(d) Azores to Lisbon

(e) Zero Ocean Dynamics Present

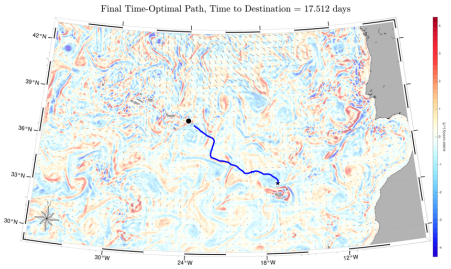

(f) Azores to Madiera

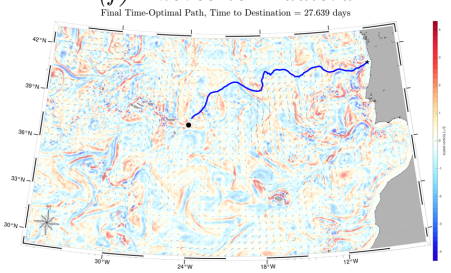

(g) Azores to Porto

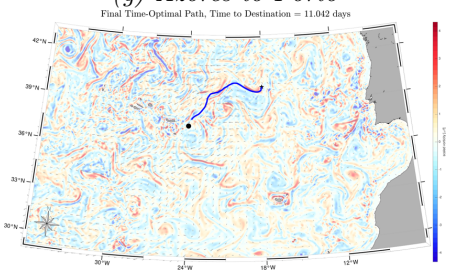

(h) Azores to Ocean Midpoint

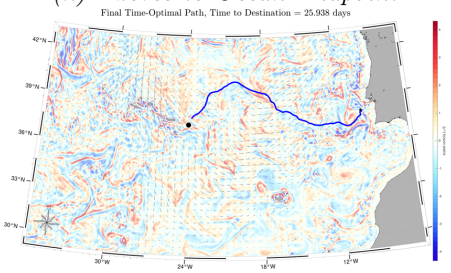

(i) Azores to Lisbon

(j) Ocean Dynamics Present

Figure 5-4: Zero flow vs Ocean Dynamics present, vehicles traveling at 0.5 m/s from the Azores to various end points. The plot background is the unitless surface scaled vorticity. The magnitude of the surface vorticity is shown in the colorbar, and is zero when no ocean dynamics are present.

This simple comparison is a relevant launching point for all applications in this study. It shows what the baseline direct path would be if the vehicle was not affected by the background flow field, e.g. using the flow fields to hitchhike on favorable currents and achieve a faster time-optimal path.

5.3 Individual point-to-point

For this mission type, the time-optimal path is planned from a single start point to a single end point. The points used are the repeating five important locations listed in Table 3.1 in Chapter 3. This mission type is important to this study because it illustrates the basic method of this type of path planning for long journeys between major destinations. Possible applications for this case could be transport, long-range monitoring, or data collection along a major shipping path, all of which are important to the Portugal-Azores-Madeira ocean region.

For the first run in this case, we study a vehicle that travels from Lisbon to Azores. The vehicle will be travelling through the surface currents of the flow field. The parameters shown in Table 5.2 are the inputs used for the case parameters for this path.

Parameters	Value
dims	2
dt	1,000 sec
t_i	0.0 sec
depth	2nd vertical level (surface)
$\boldsymbol{x}_s$	Lisbon: 38.0° N, 10.0° W
$\boldsymbol{x}_f$	Azores: 37.5° N, 24.0° W
Speed	0.5 meters/sec
$\boldsymbol{V}(\boldsymbol{x}, t)$	MSEAS-PE model flow-field
ir	50,000 meters

Table 5.2: Lisbon to Azores run input parameters

With these input parameters, we first examine the evolving level sets of the reachability front, shown at different times in the front's evolution in Figures 5-5 and 5-6. This allows us to observe the effects of the ocean dynamics in this case. The strong flow-fields that surround the vehicle show that there are variations in the reachability front based on the location of favorable currents and eddies to propel (thrust) the vehicle in the fastest direction, or avoid a slower direction from a current opposite of the intended path. In this case, there are variations throughout the level sets. For example, the reachability front can be seen to extend further south, indicating that, for the same time duration, the vehicle can travel further when travelling south.

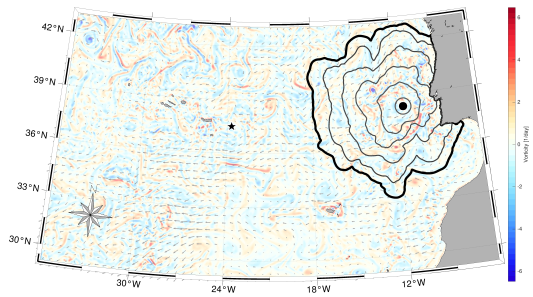

Figure 5-5: Evolving level sets of reachability front for AUV travelling at 0.5 m/s from Lisbon to Azores. The plot background is the unitless surface scaled vorticity. The magnitude of the vorticity is shown in the colorbar.

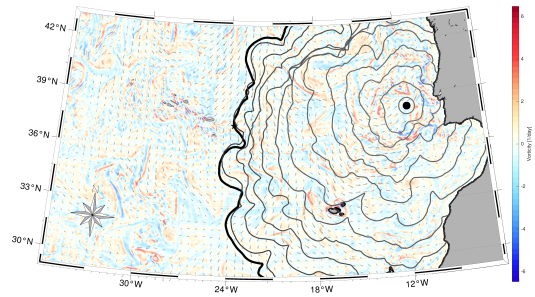

Figure 5-6: Final level set of reachability front for AUV travelling at 0.5 m/s from Lisbon to Azores. The plot background is the unitless surface scaled vorticity. The magnitude of the vorticity is shown in the colorbar.

After the evolution of the reachability sets, the next step is to backtrack, as shown in Figure 5-7 to get the final time-optimal path for this case, which is shown in Figure 5-8. The effects of the background flow-field velocity shows that the final time-optimal path is not a straight line from start to end points, but a varying path that travels further south in some areas, and farther north in others as it encounters surface currents.

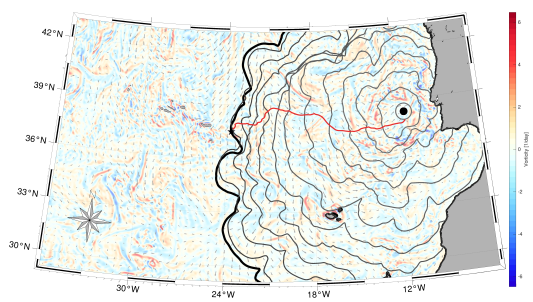

Figure 5-7: Final backtracking for AUV travelling at 0.5 m/s from Lisbon to Azores. The plot background is the unitless surface scaled vorticity. The magnitude of the vorticity is shown in the colorbar.

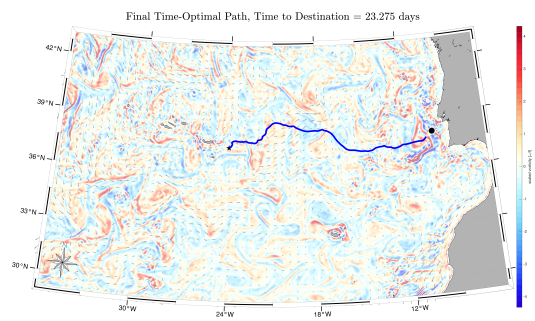

Figure 5-8: Final time-optimal path for AUV travelling at 0.5 m/s from Lisbon to Azores. The plot background is the unitless surface scaled vorticity. The magnitude of the vorticity is shown in the colorbar.

With the focus on vehicle speed, it is worth examining how the input vehicle speed does not change throughout the journey. Figure 5-9 illustrates how the vehicle propulsion speed will not change throughout the run, and is based on the input speed

parameter for each journey, from Table 5.2. As discussed in Chapter 4, the relative speed of the vehicle, F, will not remain constant through the journey, as it interacts with the background velocity flow-fields, $\boldsymbol{V}(\boldsymbol{x}, t)$.

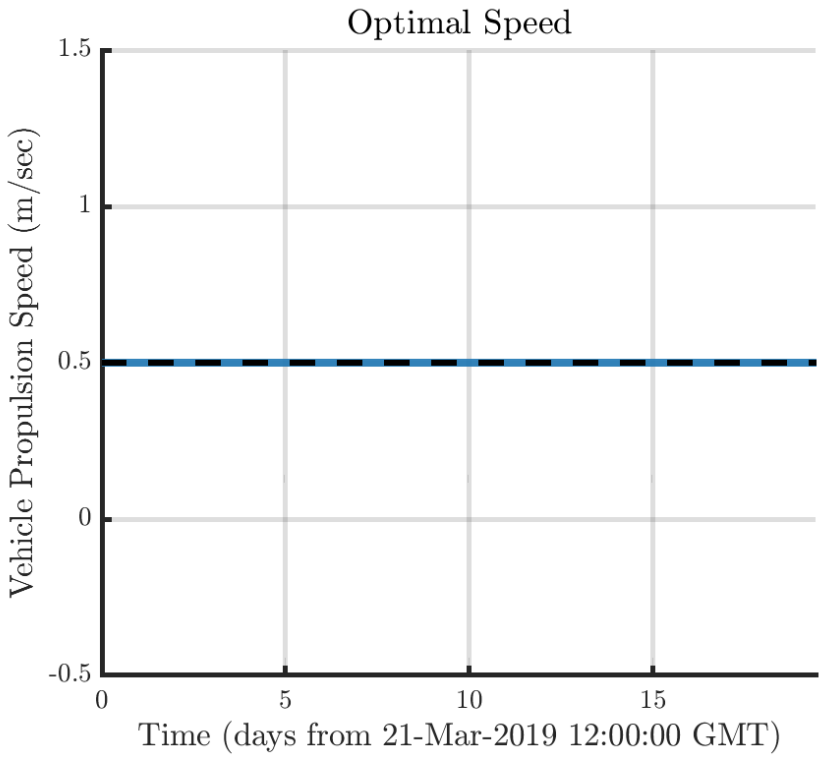

Figure 5-9: Vehicle propulsion speed (m/sec) against total time of the path. The Vehicle propulsion speed remains constant throughout journey.

We repeated this case using the same methods for all possible run combinations between the five major locations, with a total of 20 runs for an AUV operating at 0.5 m/s, and another 20 runs for an AUV operating at 1.5 m/s. Each of these missions will use the same case input parameters as described in Table 5.2, but with variation to $\boldsymbol{x}_s$, $\boldsymbol{x}_f$, and speed. In Figure 5-10 below, the final time-optimal paths are shown for some of these run configurations, with the final time shown in the title of each subfigure.

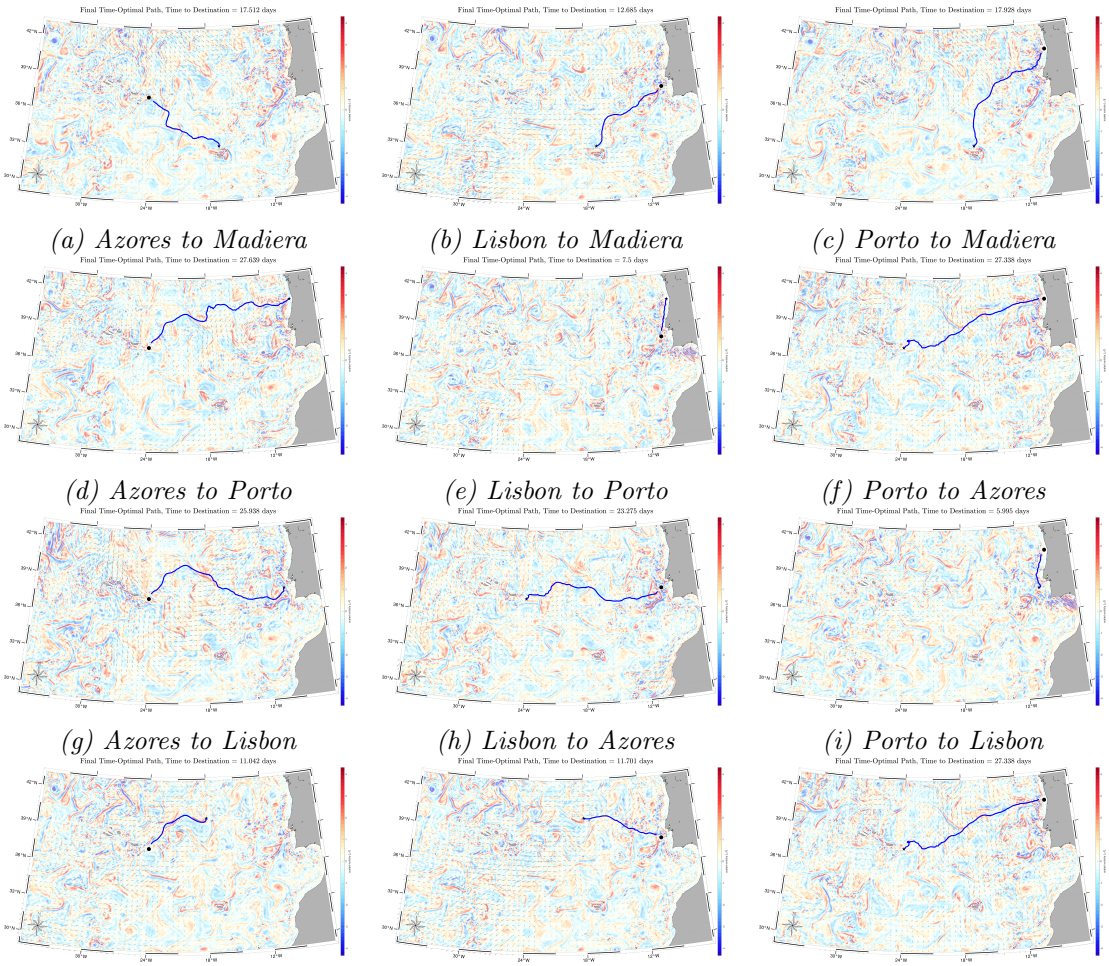

(a) Azores to Madiera *(b) Lisbon to Madiera* *(c) Porto to Madiera*

(d) Azores to Porto *(e) Lisbon to Porto* *(f) Porto to Azores*

(g) Azores to Lisbon *(h) Lisbon to Azores* *(i) Porto to Lisbon*

(j) Azores to Ocean Midpoint *(k) Lisbon to Ocean Midpoint* *(l) Porto to Ocean Midpoint*

Figure 5-10: Final time-optimal path for individual point-to-point runs throughout the domain for various start and end points, for AUVs travelling at 0.5 m/s. The plot background is the unitless surface scaled vorticity. The magnitude of the vorticity is shown in the colorbar.

Another way to illustrate the effects of the velocity flow-field $\boldsymbol{V}(\boldsymbol{x}, t)$ on the vehicle is to compare the final time-optimal path with the path of the vehicle in the zero flow-field state. As shown in Figure 5-11 below, the vehicle using the advantage of the background ocean dynamics present will travel 5.1 days faster than a vehicle in a direct path with no ocean dynamics present.

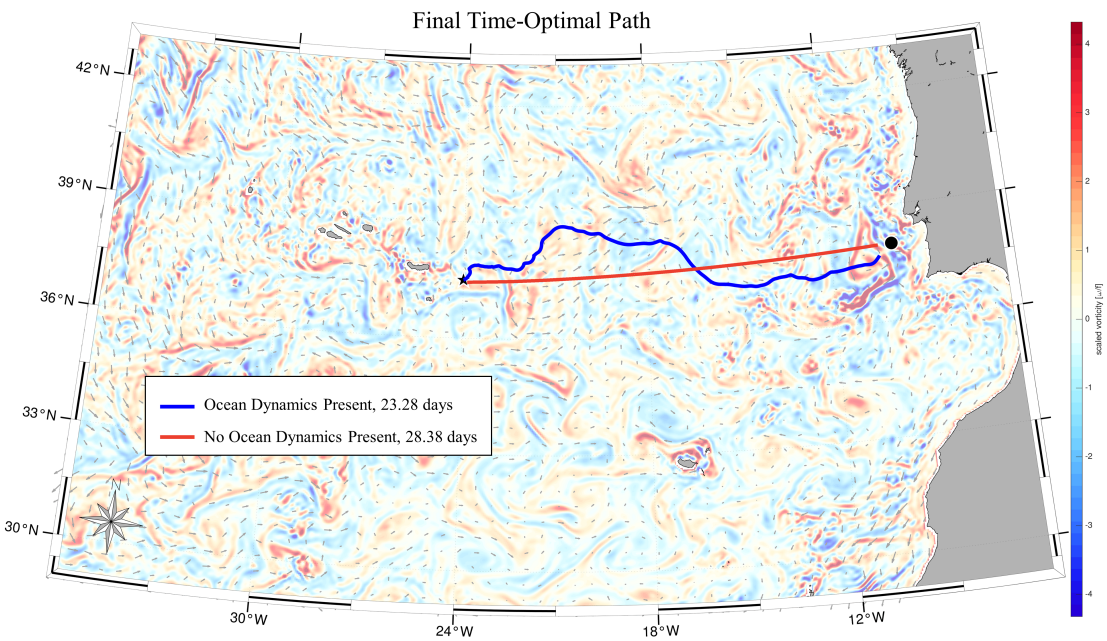

Figure 5-11: Comparison of time-optimal paths of point-to-point case with flow-field vs zero flow-field case. Vehicles travelling from Lisbon to Azores at 0.5 m/s. The plot background is the unitless surface scaled vorticity. The magnitude of the vorticity is shown in the colorbar, and applies to the case with ocean dynamics present.

Figure 5-12 below shows more of these comparisons for point-to-point runs. As shown in the figure, the final time-optimal path with the background ocean dynamics model is much more curved and varied than the direct path where there is zero flow-field present. While the optimal path is usually faster than the direct path, there are some exceptions, as seen in Azores to Madeira where the direct path is 0.6 days faster. This can happen when there are several strong persistent currents within their region during the time domain, which can increase the final travel time. With the zero-flow field, the vehicle propulsion speed will be equal to the relative speed of the vehicle, F, since there is no background velocity flow-fields $\boldsymbol{V}(\boldsymbol{x}, t)$ present.

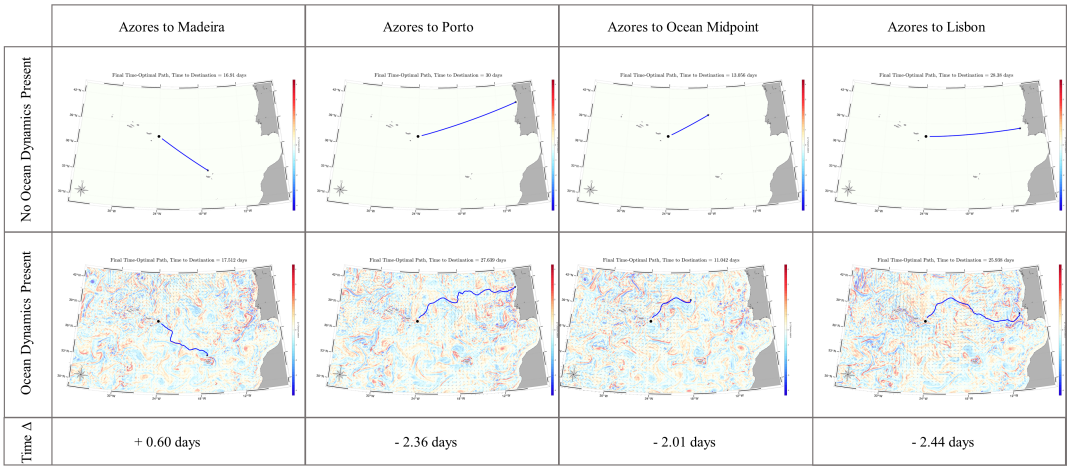

Figure 5-12: Comparison of time-optimal paths of multiple point-to-point case with flow-field vs zero flow-field case for various start and end points, for AUVs travelling at 0.5 m/s. The plot background is the unitless surface scaled vorticity. The magnitude of the vorticity is shown in the colorbar. The time Δ between the ocean dynamics vs no ocean dynamics case will be positive when the no flow-field case is faster.

Overall, this case builds a great foundation for other applications of this study, by computing the optimal paths between two points. These runs were used in comparing the effects of varying parameters, as shown in the next section.

5.4 Comparisons within Individual Cases

5.4.1 Vehicle Speed

For this case, the time-optimal path is planned between a start point and an end point, but varying the vehicle speed to show the variation between an AUV travelling at 0.5 m/s (∼1 knot) for slow operating speed, and at 1.5 m/s (∼3 knots) for faster operating speed, as described in Chapter 3, Section 3.3.3.

This type of case comparison is relevant to this study because it illustrates the need to take AUV speed into consideration when planning for a specific mission type, such as long range missions. The speed not only affects the direct outcome of total

travel time by the basic $time = \frac{distance}{speed}$ relationship, but also the time-optimal path, since a faster vehicle speed will be less influenced by the velocity flow-field.

Possible applications for this case comparison would be data collection and surveillance, as well as any sort of transport, security, or ocean monitoring mission where multiple vehicles may need to travel at different speeds to meet their goals of the mission.

The following parameters are outlined in Table 5.3, for the inputs used for the case of the slower vehicle, as well as Table 5.4, for the inputs used for the case of the faster vehicle.

Parameters	Value
dims	2
dt	1,000 sec
t_i	0.0 sec
depth	2nd vertical level (surface)
$\boldsymbol{x}_s$	Lisbon: 38.0° N, 10.0° W
$\boldsymbol{x}_f$	Azores: 37.5° N, 24.0° W
Speed	0.5 meters/sec
$\boldsymbol{V}(\boldsymbol{x}, t)$	MSEAS-PE model flow-field
ir	50,000 meters

Table 5.3: 0.5 run input parameters

Parameters	Value
dims	2
dt	1,000 sec
t_i	0.0 sec
depth	2nd vertical level (surface)
$\boldsymbol{x}_s$	Lisbon: 38.0° N, 10.0° W
$\boldsymbol{x}_f$	Azores: 37.5° N, 24.0° W
Speed	1.5 meters/sec
$\boldsymbol{V}(\boldsymbol{x}, t)$	MSEAS-PE model flow-field
ir	50,000 meters

Table 5.4: 1.5 m/s run input parameters

With these input parameters, we used the same methods as the individual point-to-point case, with the evolution of the reachability front through the velocity flow-field, and backtracking to the final time-optimal paths for this case, which are shown together in Figure 5-13.

As shown in the figure, the final time-optimal paths will differ with vehicle speed of the surface AUV. The green path in Figure 5-13 from Lisbon to the Azores has a speed of 0.5 m/s, while the pink path has a speed of 1.5 m/s. The pink, faster vehicle path is a "smoother" and more direct path, as it less affected by the small-scale velocities of the ocean surface current velocity. As shown in the ocean modelling figures in

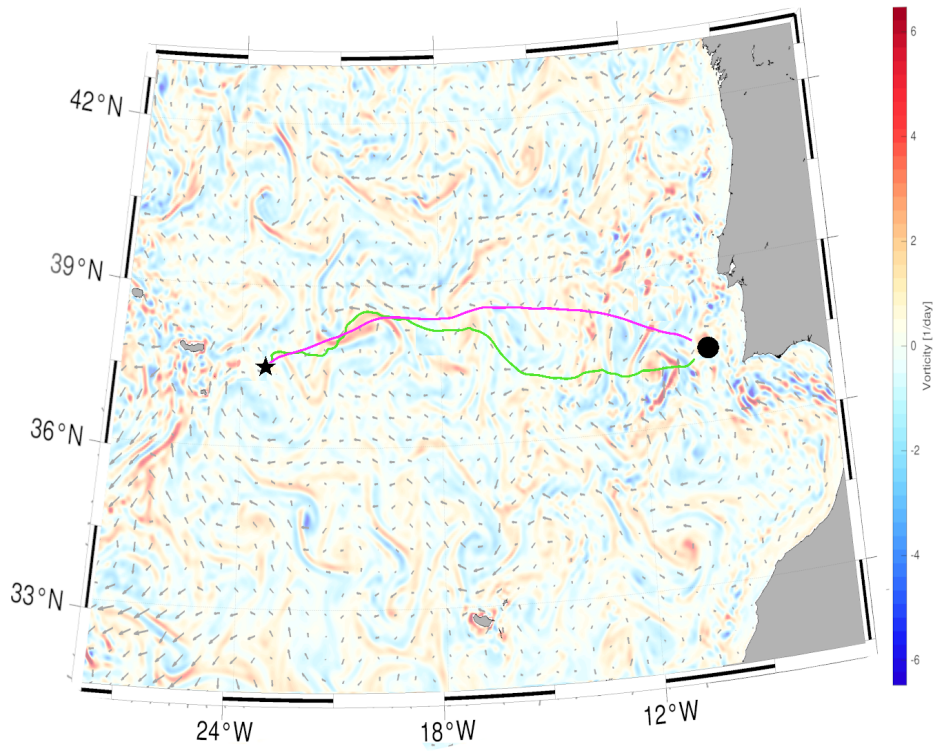

Figure 5-13: Speed comparison of time-optimal paths for AUVs travelling from Lisbon to Azores at 0.5 m/s (green) vs 1/5 m/s (pink). The plot background is the unitless surface scaled vorticity. The magnitude of the vorticity is shown in the colorbar.

Chapter 3, Section 3.2, the surface velocity $\boldsymbol{V}(\boldsymbol{x}, t)$ rarely exceeds 1.5 m/s, so a AUV traveling at 1.5 m/s will be equal in velocity to the surface velocity. The green, slower vehicle path is much more curved and varied than the faster vehicle path, and travels first further south, and then north, following the location of favorable currents and eddies to propel the vehicle towards a fastest optimal path. Overall, the final time to destination for the 0.5 m/s speed vehicle will be 23.28 days in this case, which is 15.29 days slower than the 1.5 m/s speed vehicle at 7.99 days.

We repeated this case using the same methods for more runs between different points, and all runs showed that varying the input parameter of speed will change the final time-optimal path. This case in particular was highlighted in this discussion because it covers a long distance and has a greater chance of illustrating differences in the paths due to speed changes.

5.4.2 Path Direction

For this case, the time-optimal path is planned between a start point and an end point in one direction, and compared to the path in the opposite direction, from that same end point to the same start point. Simply put, this comparison studies an AUV travelling in one direction (Lisbon to Azores) to an AUV travelling the opposite direction (Azores to Lisbon), both starting on the same day.

This type of case comparison is relevant to this study because it illustrates the need to take AUV direction into consideration when planning for a specific mission type, such as recursive missions. The direction can affect both the time duration and direction of the path, as the two AUVs will experience the velocity flow-field in different ways, and significant currents that sweep through the domain may be felt by one AUV only.

Possible applications for this case comparison would be transport, security, fisheries, ocean monitoring and mapping - any mission where vehicles are repeating a journey from one point to another, and repeating in the opposite direction. This could also apply to multiple vehicles that are being released from two drop off points, such as two "mother ship" research vessels deploying AUVs, where they travel to the other research vessel to be picked up, creating opposing vehicle paths between the two research vessels.

The following parameters are outlined in Table 5.5, for the inputs used for the case of the vehicle travelling from Lisbon to Azores, as well as Table 5.6, for the inputs used for the case of the vehicle travelling from Azores to Lisbon. The vehicle speed selected for these runs was 0.5 m/s, in order to have increased interaction with the velocity flow-field.

Parameters	Value
dims	2
dt	1,000 sec
t_i	0.0 sec
depth	2nd vertical level (surface)
$\boldsymbol{x}_s$	Lisbon: 38.0° N, 10.0° W
$\boldsymbol{x}_f$	Azores: 37.5° N, 24.0° W
Speed	0.5 meters/sec
$\boldsymbol{V}(\boldsymbol{x}, t)$	MSEAS-PE model flow-field
ir	50,000 meters

Table 5.5: Lisbon to Azores parameters

Parameters	Value
dims	2
dt	1,000 sec
t_i	0.0 sec
depth	2nd vertical level (surface)
$\boldsymbol{x}_s$	Azores: 37.5° N, 24.0° W
$\boldsymbol{x}_f$	Lisbon: 38.0° N, 10.0° W
Speed	0.5 meters/sec
$\boldsymbol{V}(\boldsymbol{x}, t)$	MSEAS-PE model flow-field
ir	50,000 meters

Table 5.6: Azores to Lisbon parameters

With these input parameters, we used the same methods as the individual point-to-point case by first evolving of the reachability front through the velocity flow-field and then backtracking the final time-optimal paths, which are shown together in Figure 5-14.

As shown in the figure, the final time-optimal paths will differ with vehicle direction of the surface AUV. The green path in Figure 5-14 from Lisbon to the Azores is more direct, travelling slightly south from Lisbon before travelling slightly north to reach the Azores.

The pink path of the vehicle travelling from the Azores to Lisbon is more curved, travelling further north as it leaves the Azores, before travelling slightly south to Lisbon. Looking at both paths together, you can see that some ocean currents within smaller regions had similar effects on the AUVs; both paths curve slightly north in the area northwest of the Azores as ocean currents push northwest as seen by the velocity vectors, whereas both paths travel slightly south near Lisbon. Both vehicles make use of favorable currents and eddies to propel them to the destination as fast as possible, while avoiding currents and eddies that could slow them down.

Overall, the final time to destination for the path from Azores to Lisbon is 25.94 days, which is 2.66 days slower than the path from Lisbon to Azores, which takes

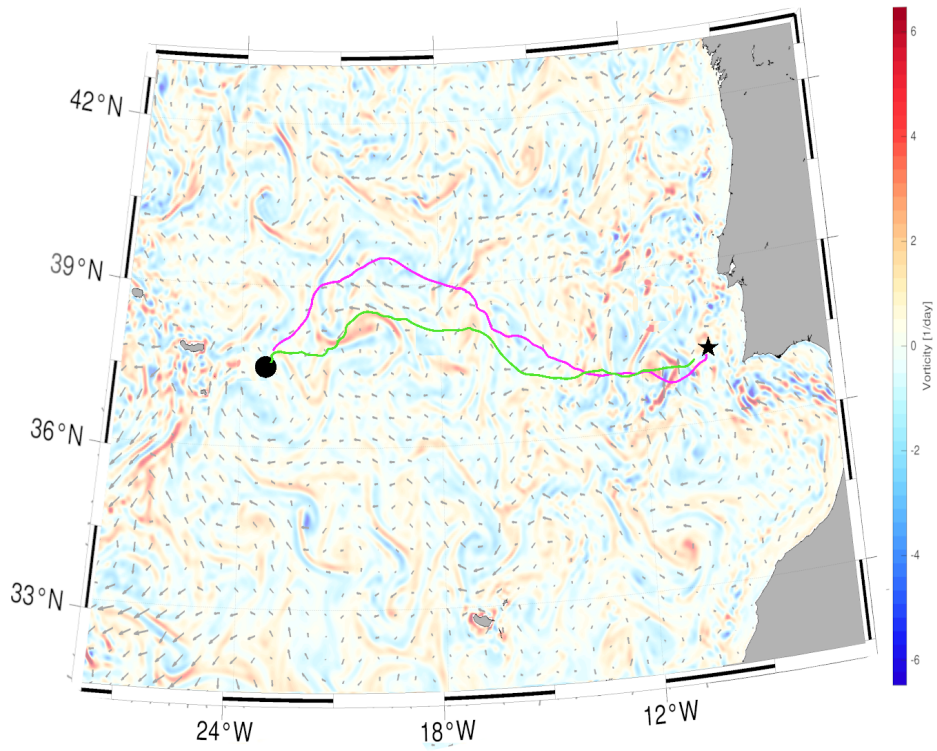

Figure 5-14: Direction comparison of time-optimal paths of AUVs travelling from Lisbon to Azores (green) vs Azores to Lisbon (pink) at 0.5 m/s. The plot background is the unitless surface scaled vorticity. The magnitude of the vorticity is shown in the colorbar.

23.28 days. As observed, the Lisbon to Azores direction is faster in this case for the velocity flow-field present during these opposite journeys.

We repeated this case using the same methods for more runs between different points, and all runs showed that varying the direction of the journey will change the final time-optimal path. This case in particular was highlighted in this discussion because it covers a long distance and has a greater chance of illustrating differences in the paths due to direction changes.

5.4.3 Start Time

For this case, the time-optimal path is planned with variations in its start time, t_i, and compared to see how changes in start time effects the final path. This type of case comparison is relevant to this study because it illustrates the need to take AUV start into consideration when planning for a specific mission type, as different

ocean dynamics and flow-fields will be present at different times, which will result in different optimal paths. For example, if one AUV is released and begins its journey on day 1 and travels through a high wind event, it will have a different path than a vehicle that is released and begins its journey on day 8 and completely misses the high wind event. Changes to the ocean dynamics over time can be seen in the figures shown in the ocean modelling figures in Chapter 3, Section 3.2.

Possible applications for this case comparison would be data collection, transportation, naval operations, ocean cleanup, or any mission where vehicles are released asynchronously instead of simultaneously.

The following parameters are outlined in Table 5.7, with the time start (t_i) varying from 1 to 10 days, with an interval of 1 day, for a total of 10 runs to compare in this case. The vehicle speed selected for these runs was 0.5 m/s, in order to have increased interaction with the velocity flow-field.

Parameters	Value
dims	2
dt	1,000 sec
t_i	Vary: 1:1:10 days
depth	2nd vertical level (surface)
$\boldsymbol{x}_s$	Lisbon: 38.0° N, 10.0° W
$\boldsymbol{x}_f$	Madeira: 33.5° N, 17.0° W
Speed	0.5 meters/sec
$\boldsymbol{V}(\boldsymbol{x}, t)$	MSEAS-PE model flow-field
ir	50,000 meters

Table 5.7: Start time variation run input parameters

With these input parameters, we used the same methods as the individual point-to-point case, with the evolution of the reachability front through the velocity flow-field, and backtracking to the final time-optimal paths for these runs, which are shown together in Figure 5-15.

As shown in the figure, the final time-optimal paths will differ with vehicle start time of the surface AUV. The paths starting on days 1-7 follow a similar path (red, orange, yellow, and pink toned colors), but on day 8 (green) the optimal path goes north, and then south for day 9 (blue) and 10 (purple), as velocity flow-field turns

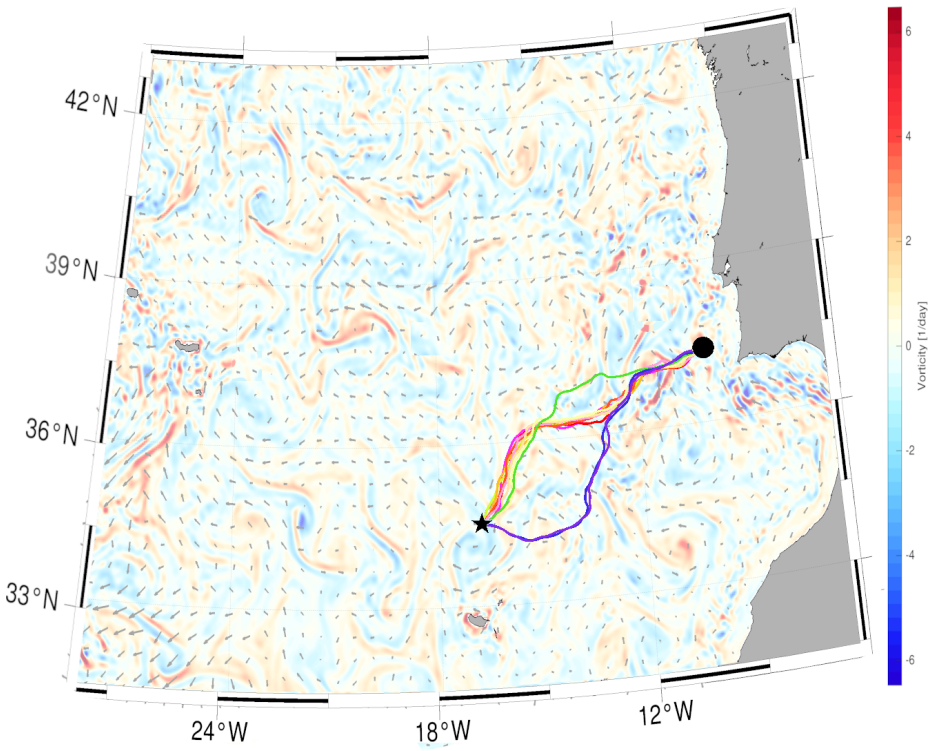

Figure 5-15: Start time comparison of time-optimal paths for multiple AUVs travelling from Lisbon to Madeira, Day 1 to Day 10 t_i, at 0.5 m/s. The plot background is the unitless surface scaled vorticity. The magnitude of the vorticity is shown in the colorbar.

south during that time window. While changes in the direction and curve of the optimal paths are illustrated in the figure, the final path time to destination is summarized in Table 5.8 for each start time, as well as adding the final optimal path time for the 0 day t_i, which represents an AUV being launched with no delays in the time start.

Overall, the final time to destination varies minimally, with the fastest paths being on and around a day 4 t_i, and the slowest times being on and around a day 9 t_i. Each of these vehicles will use favorable currents and eddies to propel the vehicle towards the fastest optimal path, and avoid currents and eddies that could slow them down, but since they are each travelling during different time periods with different velocity flow-fields present, the final time-optimal path will differ.

We repeated this case using the same methods for more runs between different points and at different speeds, and all runs showed that varying the input parameter of start time will change the final time-optimal path. This case in particular was

t_i	Final Path Total Time
0 days	12.69 days
1 day	12.57 days
2 days	12.53 days
3 days	12.38 days
4 days	12.20 days
5 days	12.41 days
6 days	12.35 days
7 days	12.44 days
8 days	13.11 days
9 days	13.83 days
10 days	13.76 days

Table 5.8: Final path total time from varying start time

highlighted in this discussion because it includes the region between Madeira and Lisbon, where high contrast changes in velocity flow-field occur due to the drop-off of the continental shelf, and therefore clearly illustrated the differences in the paths due to start time changes.

5.5 Multi-end points, one start point

For this case, the time-optimal path is planned with an AUV that has one start point, with four different possible end points. This type of case is interesting to this study because it shows the difference in time-optimal paths diverging from a central point during the same time range of ocean dynamics.

Possible applications for this case would be scientific exploration, data collection, naval operations, search and rescue, or any mission where vehicles are released from one point and can travel to many different end points. This case would also be useful in applications where a large domain had to be covered by multiple vehicles, and each vehicle would travel to different end points to explore different areas of the domain.

The following parameters, outlined in Table 5.9, are the inputs used for the case parameters for this application for vehicles starting at Lisbon.

With these input parameters, we use the same methods as the individual point to point case, with the evolution of the reachability front through the velocity flow-field

Parameters	Value
dims	2
dt	1,000 sec
t_i	0.0 sec
depth	2nd vertical level (surface)
$\boldsymbol{x}_s$	Lisbon: 38.0° N, 10.0° W
$\boldsymbol{x}_f$	Porto: 41.0° N, 9.0° W
	Azores: 37.5° N, 24.0° W
	Madeira: 33.5° N, 17.0° W
	Ocean (mid-domain): 40.0° N, 18.0° W
Speed	0.5 meters/sec
$\boldsymbol{V}(\boldsymbol{x}, t)$	MSEAS-PE model flow-field
ir	50,000 meters

Table 5.9: Multi-end points, Lisbon start point run input parameters

towards each end point from the common start point, and backtracking to the final time-optimal paths for these runs, which are shown together in Figure 5-16. Since this simulates either one vehicle with several options of ending points, or multiple vehicles that simultaneously travel toward the multiple end points, all of these runs were started simultaneously at the same t_i, to experience the velocity flow-field in the domain at the same time.

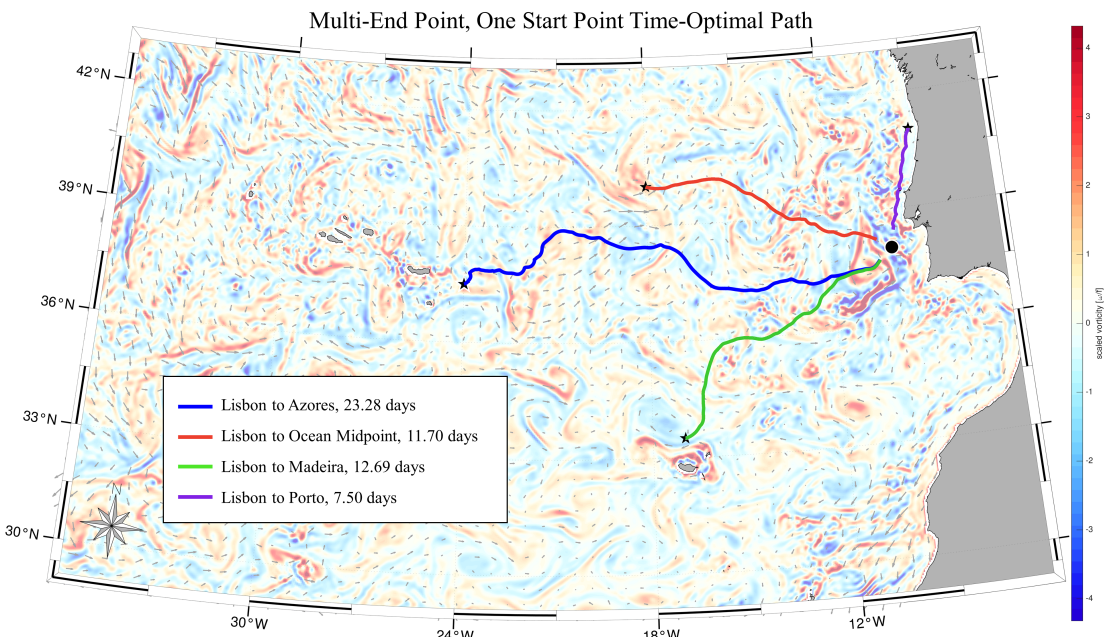

Figure 5-16: Final time-optimal paths for case with multiple end points, one common start point at Lisbon, for an AUV travelling 0.5 m/s. The plot background is the unitless surface scaled vorticity. The magnitude of the vorticity shown in the colorbar.

The figure also shows the final time to destination for each end point from the common start point. While the vehicles have the same start point, their variations in end points show how the velocity flow-fields in those smaller regions will affect the final optimal path.

We repeated this case using the same methods for more runs that used different start points with multiple end points. We highlight the starting points Madeira and Porto, in addition to Lisbon showed above, in order to show more examples of this case from different start points.

The following parameters, outlined in Table 5.10, are the inputs used for the case parameters for this application for vehicles starting at Madeira.

Figure 5-17 shows the multiple end points from the common starting point, Madeira.

Parameters	Value
dims	2
dt	1,000 sec
t_i	0.0 sec
depth	2nd vertical level (surface)
$\boldsymbol{x}_s$	Madeira: 33.5° N, 17.0° W
$\boldsymbol{x}_f$	Porto: 41.0° N, 9.0° W
	Azores: 37.5° N, 24.0° W
	Lisbon: 38.0° N, 10.0° W
	Ocean (mid-domain): 40.0° N, 18.0° W
Speed	0.5 meters/sec
$\boldsymbol{V}(\boldsymbol{x}, t)$	MSEAS-PE model flow-field
ir	50,000 meters

Table 5.10: Multi-end points, Madeira start point run input parameters

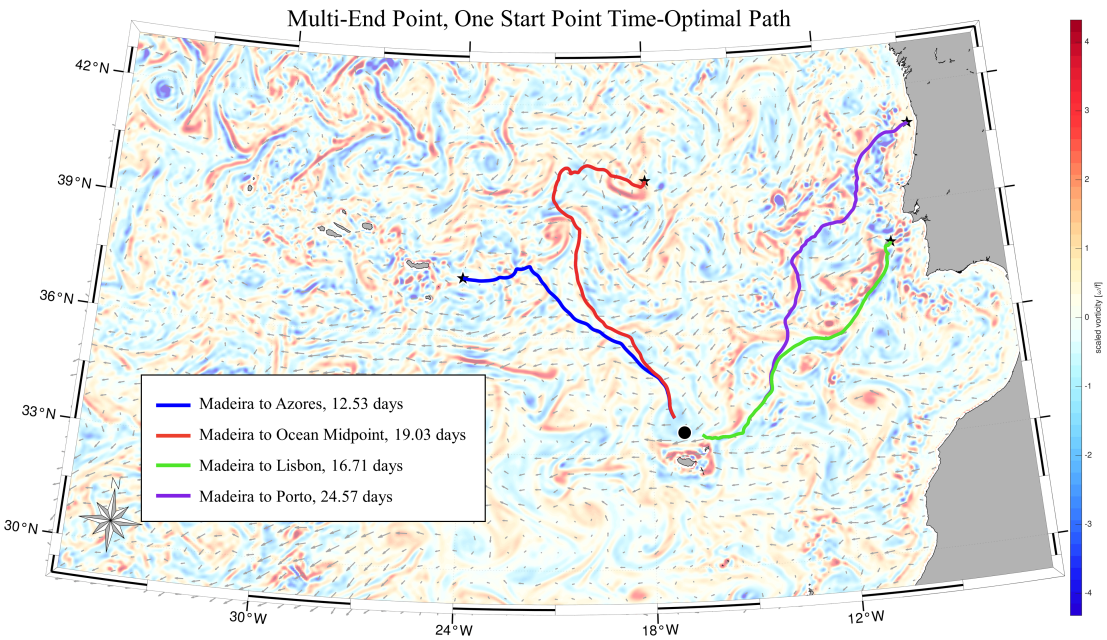

Figure 5-17: Final time-optimal paths for case with multiple end points, one common start point at Madeira for an AUV travelling 0.5 m/s. The plot background is the unitless surface scaled vorticity. The magnitude of the vorticity shown in the colorbar.

The following parameters, outlined in Table 5.11, are the inputs used for the case parameters for this application for vehicles starting at Porto.

Figure 5-18 shows the multiple end points from the common starting point, Porto.

Parameters	Value
dims	2
dt	1,000 sec
t_i	0.0 sec
depth	2nd vertical level (surface)
$\boldsymbol{x}_s$	Porto: 41.0° N, 9.0° W
$\boldsymbol{x}_f$	Madeira: 33.5° N, 17.0° W
	Azores: 37.5° N, 24.0° W
	Lisbon: 38.0° N, 10.0° W
	Ocean (mid-domain): 40.0° N, 18.0° W
Speed	0.5 meters/sec
$\boldsymbol{V}(\boldsymbol{x}, t)$	MSEAS-PE model flow-field
ir	50,000 meters

Table 5.11: Multi-end points, Porto start point run input parameters

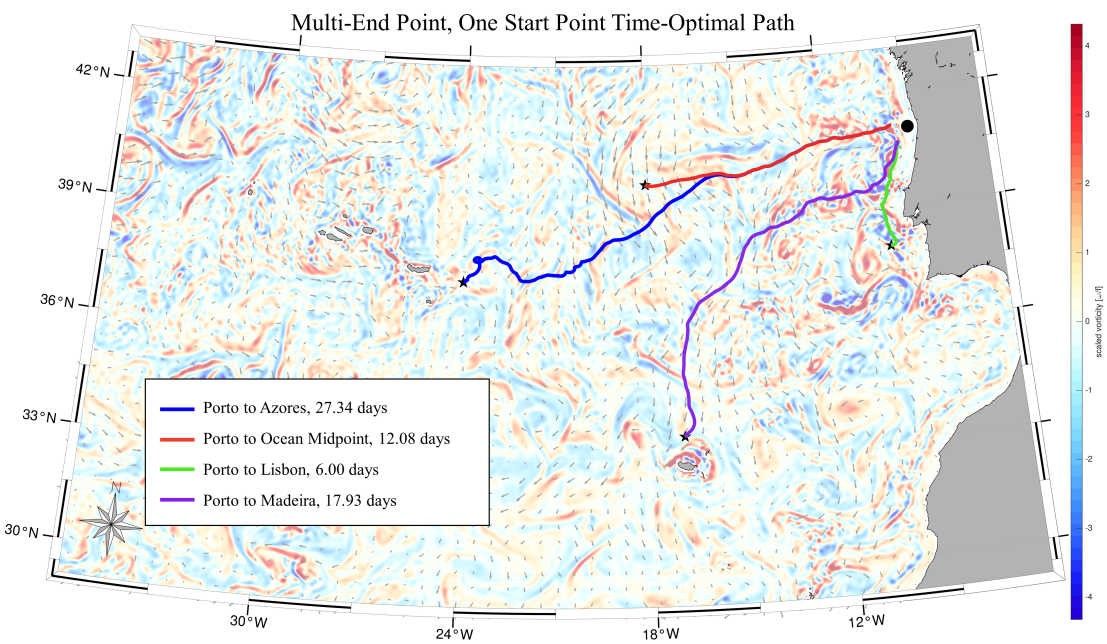

Figure 5-18: Final time-optimal paths for case with multiple end points, one common start point at Porto for an AUV travelling 0.5 m/s. The plot background is the unitless surface scaled vorticity. The magnitude of the vorticity shown in the colorbar.

5.6 Multi-start points, one end point

For this case, the time-optimal path is planned with an AUV that has one end point, with four different possible start points. This type of case is interesting to this study

because it shows the difference in time-optimal paths from vehicles starting in different locations and converging at a central point during the same time range of ocean dynamics.

Possible applications for this case would be scientific exploration, data collection, naval operations, security, ocean cleanup, or any mission where vehicles will converge at a central point. This could include applications where different AUVs are launched from different boats, and converge at one point to be picked up. Another application could be ocean cleanup, where multiple AUVs converge at one point to clean up an isolated spill.

The following parameters, outlined in Table 5.12, are the inputs used for the case parameters for this application for vehicles with paths ending at Lisbon.

Parameters	Value
dims	2
dt	1,000 sec
t_i	0.0 sec
depth	2nd vertical level (surface)
$\boldsymbol{x}_s$	Azores: 37.5° N, 24.0° W
	Madeira: 33.5° N, 17.0° W
	Ocean (mid-domain): 40.0° N, 18.0° W
	Porto: 41.0° N, 9.0° W
$\boldsymbol{x}_f$	Lisbon: 38.0° N, 10.0° W
Speed	0.5 meters/sec
$\boldsymbol{V}(\boldsymbol{x}, t)$	MSEAS-PE model flow-field
ir	50,000 meters

Table 5.12: Multi-start points, Lisbon end point run input parameters

With these input parameters, we use the same methods as the individual point to point case, with the evolution of the reachability front through the velocity flow-field from multiple start points towards one common end point, and backtracking to the final time-optimal paths for these runs, which are shown together in Figure 5-19. Since this simulates either one vehicle with several options of starting points, or multiple vehicles that simultaneously launched at different locations and travel toward the end points, all of these runs were started simultaneously at the same t_i, to experience the velocity flow-field in the domain at the same time.

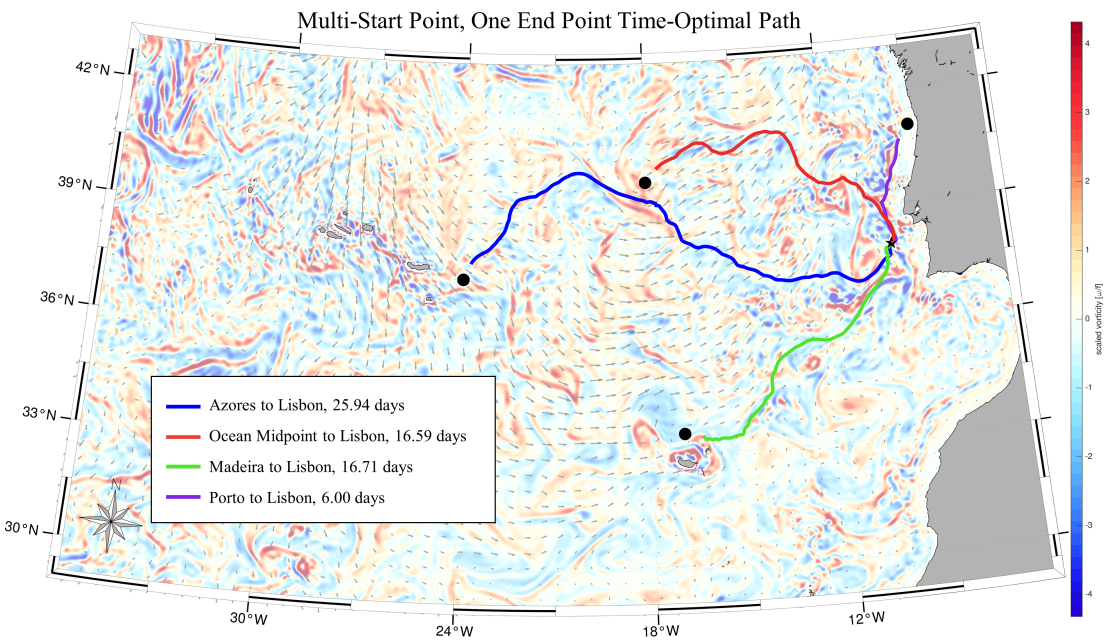

Figure 5-19: Final time-optimal paths for case with multiple start points, one common end point at Lisbon for an AUV travelling 0.5 m/s. The plot background is the unitless surface scaled vorticity. The magnitude of the vorticity shown in the colorbar.

The figure also shows the final time to destination for each starting point toward the common end point. While the vehicles have the same final destination, their variations in starting location show how the velocity flow-fields in those smaller regions will affect the final optimal path.

We repeated this case using the same methods for more runs that used different common end points with multiple start points. Here, we highlight the end point of the Azores, in addition to Lisbon showed above, in order to show more examples of this case with different end points.

The following parameters, outlined in Table 5.13, are the inputs used for the case parameters for this application for vehicles with paths ending at the Azores.

Figure 5-20 shows the multiple start points towards the common final destination of the Azores.

Parameters	Value
dims	2
dt	1,000 sec
t_i	0.0 sec
depth	2nd vertical level (surface)
$\boldsymbol{x}_s$	Lisbon: 38.0° N, 10.0° W
	Madeira: 33.5° N, 17.0° W
	Ocean (mid-domain): 40.0° N, 18.0° W
	Porto: 41.0° N, 9.0° W
$\boldsymbol{x}_f$	Azores: 37.5° N, 24.0° W
Speed	0.5 meters/sec
$\boldsymbol{V}(\boldsymbol{x}, t)$	MSEAS-PE model flow-field
ir	50,000 meters

Table 5.13: Multi-start points, Azores end point run input parameters

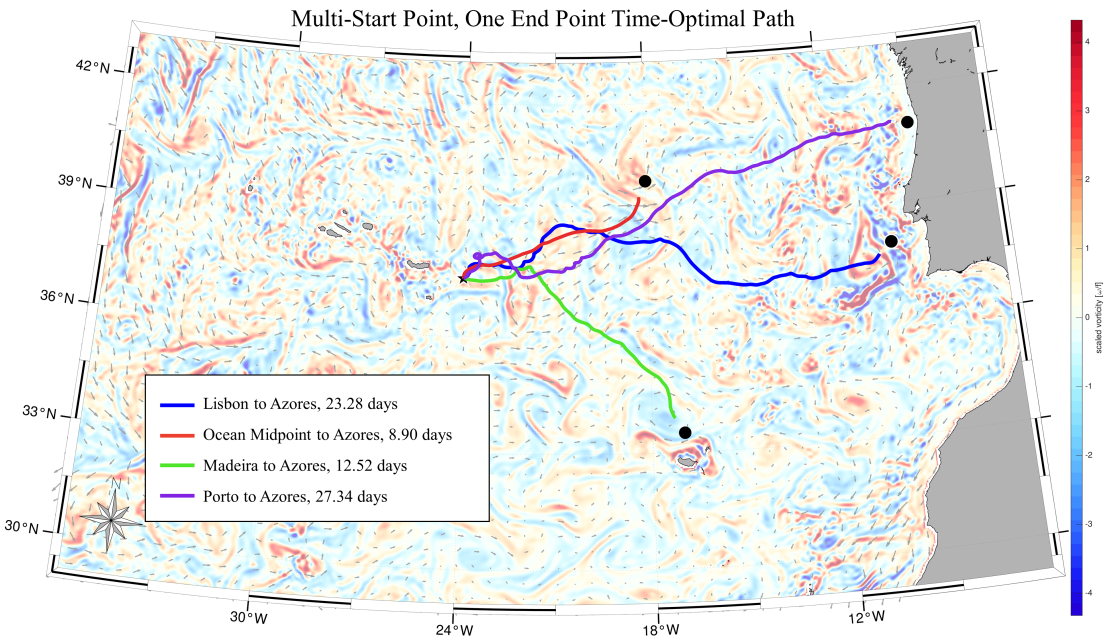

Figure 5-20: Final time-optimal paths for case with multiple start points, one common end point at Azores for an AUV travelling 0.5 m/s. The plot background is the unitless surface scaled vorticity. The magnitude of the vorticity shown in the colorbar.

5.7 Bottom paths

For this case, the time-optimal path is planned from one point to another point along the bottom of the ocean floor. This case also compared the bottom travelling AUV

run to the surface travelling AUV run, using the same input parameters except for depth.

This type of case is interesting for this study because is shows how the bottom vehicle with have a different time-optimal path from the bottom vehicle, due to differences in the velocity flow-field at the ocean surface vs the bottom.

Possible applications for this case would be naval operations, management of underwater platforms, mine-sweeping, or subsea cable monitoring. Applications with both a surface craft and bottom craft operation synchronously could collect data in the water column between the two vehicles, or one vehicle could track and relay information for the other vehicle. In this surface/depth paired vehicle application, it's important to understand the effects of the background flow-field on the final time-optimal path, and how they differ. As described in Chapter 3, Section 3.3.3, the MBARI AUV is best used to model for bottom travelling paths.

The following parameters, outlined in Table 5.14, are the inputs used for the case parameters for this application. The depth will be on the 1000th vertical level of the bathymetry. This run is simplified by keeping it in 2 dimensions, where changes in bathymetry will lead to increases in path distance as the AUV travels along the ocean floor features, but changes in vehicles' vertical movement is omitted. This case used a slow operation speed, 0.5 m/s, because the ocean dynamics flow-field is reduced at the ocean floor, as summarized in Chapter 3, Section 3.2.

Parameters	Value
dims	2
dt	1,000 sec
t_i	0.0 sec
depth	100th vertical level (bottom)
$\boldsymbol{x}_s$	Lisbon: 38.0° N, 10.0° W
$\boldsymbol{x}_f$	Azores: 37.5° N, 24.0° W
Speed	0.5 meters/sec
$\boldsymbol{V}(\boldsymbol{x}, t)$	MSEAS-PE model flow-field
ir	50,000 meters

Table 5.14: Input parameters for bottom vehicle, traveling at 0.5 m/s from Lisbon to Azores

With these input parameters, we first examine the evolving level sets of the reach-

ability front, and the backtracking that creates a final time-optimal path. The level sets and final paths for the surface and bottom vehicles are shown in Figures 5-21 and 5-22. This comparison allows us to observe the effects of the ocean dynamics on a vehicle at depth. The smooth, circular level sets and direct final path of the bottom vehicles as compared to the surface vehicle confirms the reduced currents near the ocean floor.

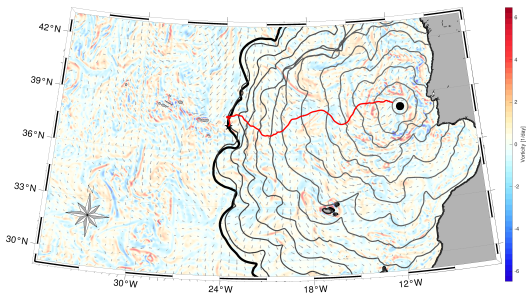

Figure 5-21: Level sets and final backtracking for surface craft travelling from Lisbon to Azores at 0.5 m/s. The plot background is the unitless surface scaled vorticity. The magnitude of the vorticity shown in the colorbar.

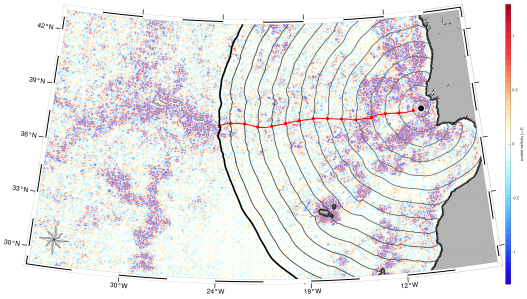

Figure 5-22: Level sets and final backtracking for bottom craft travelling from Lisbon to Azores at 0.5 m/s. The plot background is the unitless bottom scaled vorticity. The magnitude of the vorticity shown in the colorbar.

The final time-optimal path of the bottom vehicle travelling from Lisbon to Azores is shown in Figure 5-23

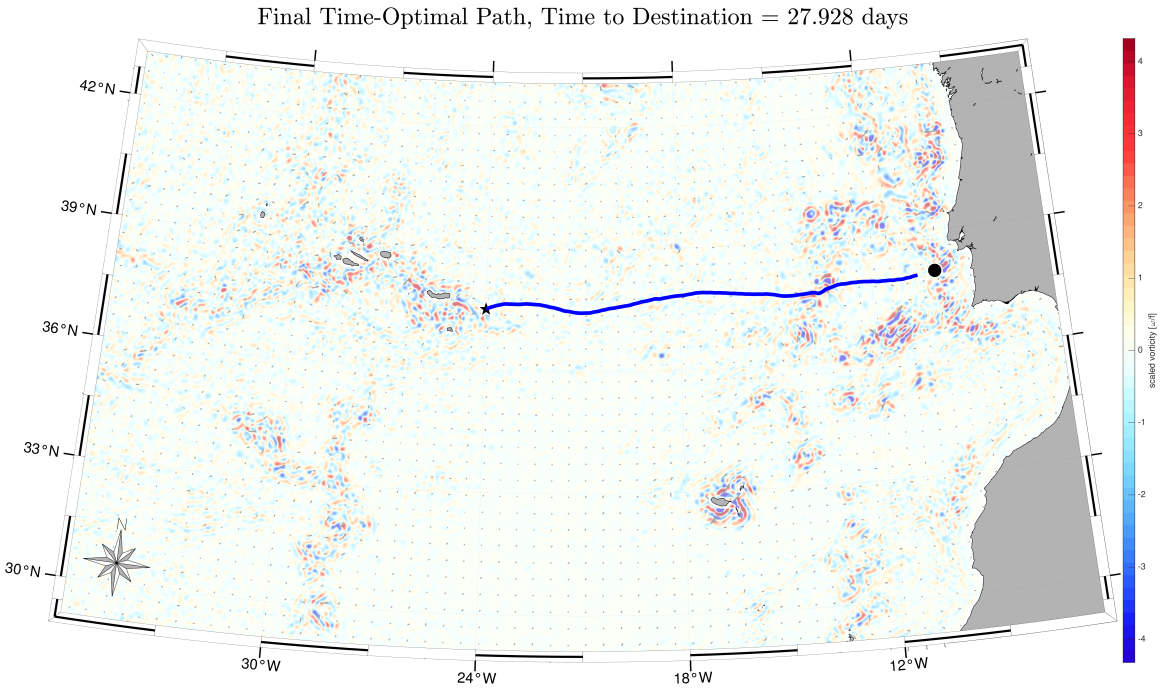

Figure 5-23: Final time-optimal path for bottom craft, traveling at 0.5 m/s from Lisbon to Azores. The plot background is the unitless bottom scaled vorticity. The magnitude of the vorticity shown in the colorbar.

The final time-optimal paths of both the surface and bottom vehicles directly compared is shown in Figure 5-24. The background of this comparison figure is the bottom vorticity present in the domain.

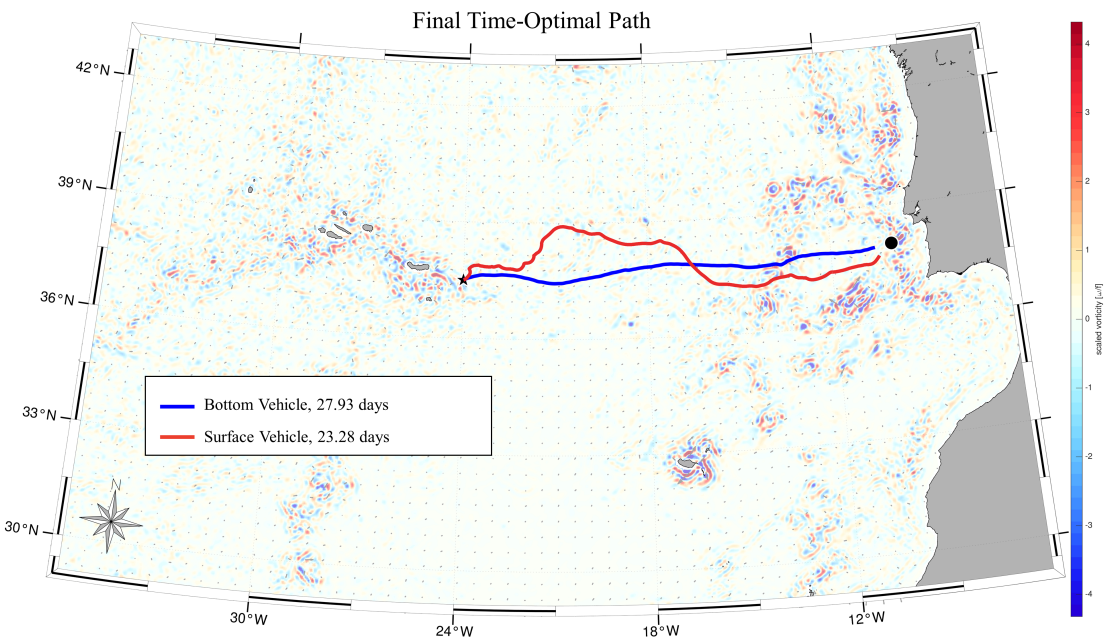

Figure 5-24: Final time-optimal paths for bottom vs surface Craft, travelling from Lisbon to Azores at 0.5 m/s. The plot background is the unitless bottom scaled vorticity. The magnitude of the vorticity shown in the colorbar.

As shown in the figure, the final time-optimal paths will differ between the vehicle travelling at the surface and the vehicle travelling on the ocean bottom. The bottom vehicle is more direct, while the surface vehicle travels slightly south and then northwest, before travelling southwest to arrive at the Azores. Both vehicles make use of favorable currents and eddies to propel the vehicle towards the fastest optimal path, and avoid currents and eddies that could slow them down, but the direct path of the bottom vehicle indicates the reduced currents near the ocean floor. Overall, the final time to destination for the bottom AUV is 27.93 days, which is 4.65 days slower than surface vehicle, which takes 23.28 days. Even though both vehicles have the same input operating speed, the surface vehicle hitchhikes on favorable currents to have a faster arrival time.

We repeated this case using the same methods for more runs. In addition to the Lisbon to Azores runs, this section will also illustrate the Madeira to Porto bottom and surface vehicle runs. These cases in particular were highlighted in this discussion because it covers a long distance and has a greater chance of illustrating differences

in the paths due to background flow-field interactions.

The following parameters, outlined in Table 5.15, are the inputs used for the case parameters for this subsequent run for an ocean bottom travelling vehicle from Madeira to Porto.

Parameters	Value
dims	2
dt	1,000 sec
t_i	0.0 sec
depth	100th vertical level (bottom)
$\boldsymbol{x}_s$	Madeira: 33.5° N, 17.0° W
$\boldsymbol{x}_f$	Porto: 41.0° N, 9.0° W
Speed	0.5 meters/sec
$\boldsymbol{V}(\boldsymbol{x}, t)$	MSEAS-PE model flow-field
ir	50,000 meters

Table 5.15: Input parameters for bottom vehicle, traveling at 0.5 m/s from Madeira to Porto

The final time-optimal path of the bottom vehicle travelling from Madeira to Porto is shown in Figure 5-25.

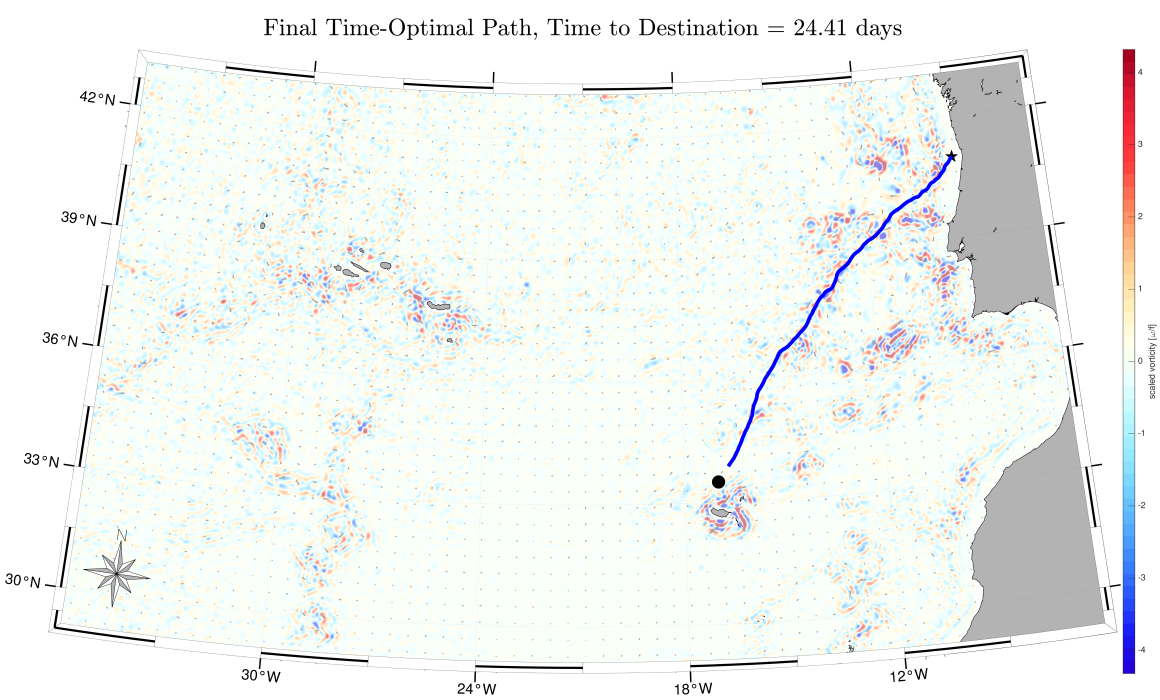

Figure 5-25: Final time-optimal path for bottom craft, traveling at 0.5 m/s from Madeira to Porto. The plot background is the unitless bottom scaled vorticity. The magnitude of the vorticity shown in the colorbar.

The final time-optimal paths of both the surface and bottom vehicles directly compared is shown in Figure 5-26. The background of this comparison figure is the bottom vorticity present in the domain.

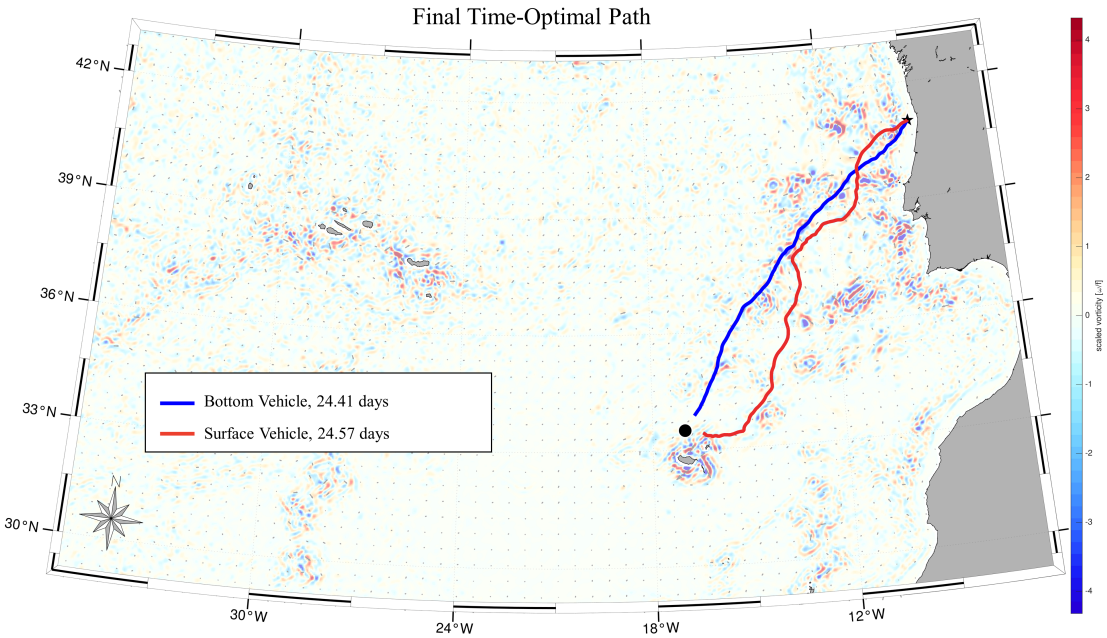

Figure 5-26: Final time-optimal paths for bottom vs surface craft, travelling from Madeira to Porto at 0.5 m/s. The plot background is the unitless bottom scaled vorticity. The magnitude of the vorticity shown in the colorbar.

As shown in the figure, the final time-optimal paths again differ between the vehicle travelling at the surface and the vehicle travelling on the ocean bottom, as it did for the previous example of this comparison. The bottom vehicle is more direct, while the surface vehicle path is more curved and varied. Both vehicles make use of favorable currents and eddies to propel the vehicle towards the fastest optimal path, and avoid currents and eddies that could slow them down, but the direct path of the bottom vehicle indicates the reduced currents near the ocean floor. Overall, the final time to destination for the bottom AUV is 24.41 days, which is only 3.84 *hours* slower than surface vehicle, which takes 24.57 days. Even though both vehicles have the same input operating speed, the surface vehicle may have encountered unavoidable, unfavorable currents that reduced its net velocity through the velocity flow field, and increased the total time to reach its destination. This is a great example of how the

velocity flow-field can either speed up or slow down the journey.

5.8 Interceptions

The interception, or “rendezvous”, problem has received increased attention in recent years, being the subject of previous theoretical studies in pursuit evasion [100, 101], and has been applied during AUV operations in several regions, including the southern littoral of Massachusetts [71, 23] and the northern Arabian Sea [51]. For this case, the time-optimal path is planned for two surface vehicles that intercept each other, or “rendezvous”. This type of case is an important next level up from the direct, point-to-point cases that use one vehicle. This case is more challenging, as computing the optimal path to a moving target is a much more complex task.

Possible applications for this case would be vessel interception, search and rescue operations, inspections of ships’ hulls, law enforcement, scientific studies, naval operations, or any other mission where two or more vehicles must intercept each other and meet up. This application is also useful for coordinating the pickup of an AUV by its "mothership" or mission control station.

For this case, we solved a complicated dynamic Model Predictive Control (MPC) problem to find time-optimal paths to moving destinations in dynamic environments. For this case, a vehicle travelling from Madeira will intercept a vehicle as it travels from Lisbon toward the Azores. The intercepted vehicle will be on a time-optimal path to its destination, and the intercepting vehicle will rendezvous with the vehicle in the fastest time possible. The first step of this is to determine the final time-optimal route of the target vehicle that will be intercepted. This used the same method of the point-to-pint cases, with evolving level sets and backtracking to compute the final time-optimal path shown in Figures 5-27 and 5-28.

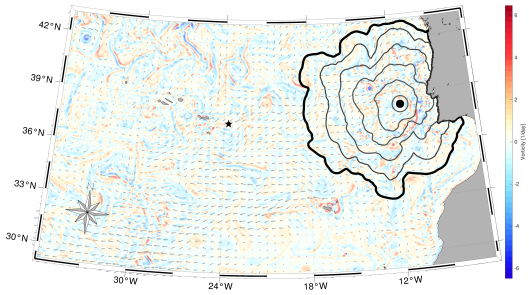

Figure 5-27: Level Sets for time-optimal path outline for target vehicle (vehicle 1). The plot background is the unitless surface scaled vorticity. The magnitude of the vorticity shown in the colorbar.

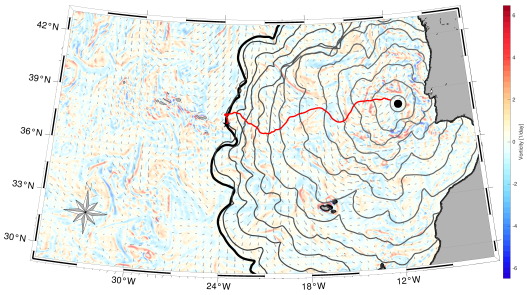

Figure 5-28: Final backtracking for target vehicle (vehicle 1). The plot background is the unitless surface scaled vorticity. The magnitude of the vorticity shown in the colorbar.

This final time-optimal path yielded from this computation for the first vehicle is shown in Figure 5-29 and 5-30. The time-optimal path is shown by the dashed line, and the green line along it shows the progress of the vehicle as it executes this path. The second vehicle, the interceptor, must intercept the vehicle somewhere along this path.

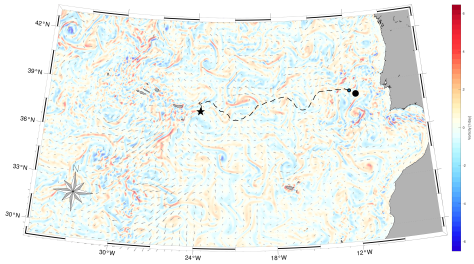

Figure 5-29: Final time-optimal path outline for vehicle 1.

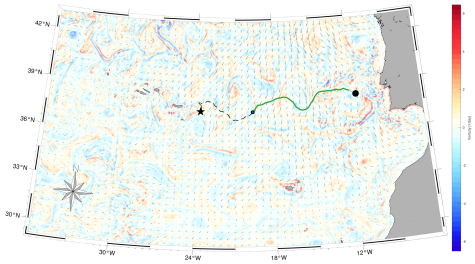

Figure 5-30: Vehicle 1 halfway through executing time-optimal path.

To determine the intercepting path of the second vehicle, the level sets will evolve from the starting point Madeira, as shown in Figures 5-31 and 5-32, propagating towards the first vehicle along its time-optimal path.

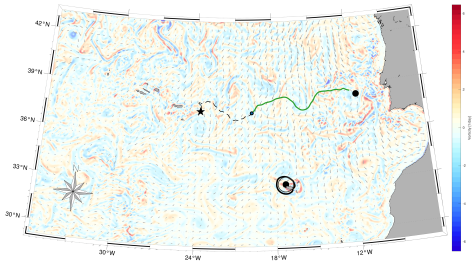

Figure 5-31: Vehicle 2 level sets begin. The plot background is the unitless surface scaled vorticity. The magnitude of the vorticity shown in the colorbar.

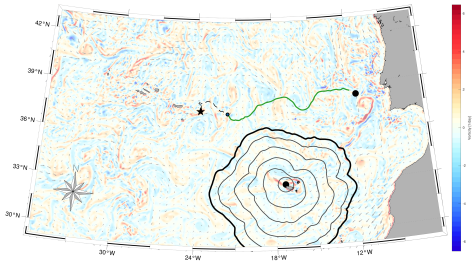

Figure 5-32: Vehicle 2 level sets continue. The plot background is the unitless surface scaled vorticity. The magnitude of the vorticity shown in the colorbar.

In Figure 5-33, the level sets of the second vehicle intercept the first vehicle, and the second vehicle path computation will now backtrack to get the final time-optimal path, shown in Figure 5-34.

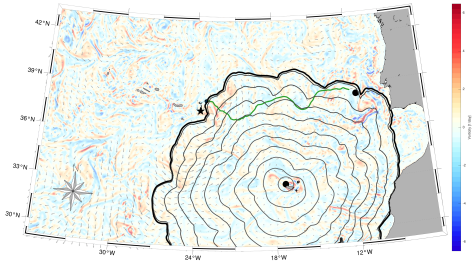

Figure 5-33: Vehicle 2 level sets end when they intercepted vehicle 1 travelling along its time-optimal path. The plot background is the unitless surface scaled vorticity. The magnitude of the vorticity shown in the colorbar.

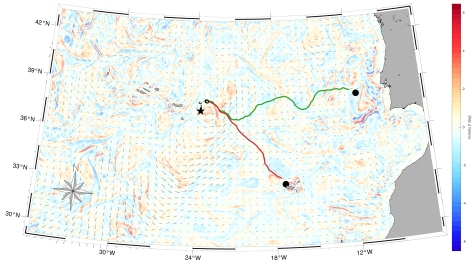

Figure 5-34: Final time-optimal interception paths for vehicle 1 and 2. The plot background is the unitless surface scaled vorticity. The magnitude of the vorticity shown in the colorbar.

This method allowed us to find the fastest interception route for the second vehicle. Since this second vehicle was set to travel at a faster speed (1 m/s) than the first vehicle (0.5 m/s), it was able to intercept it before it reached its destination, taking 9.1 days to intercept. This method shows an example of time-optimal path planning being used for a dynamic destination instead of a static one. Since this interception happened with two vehicles that travelled from areas a far distance from each other, the effects of vessel interaction at close quarters were not used in this calculation.

Past MSEAS research has studied these interactions between vehicles for close quarter interception, including a Kelvin wedge wake model to include the effect of ship wakes [71].

5.9 Arrival Time Fields

For this case, we simulated a prediction of all the arrival times for an AUV traveling around and through a field of islands. We selected the Azores archipelago islands domain due to the various islands within it.

This type of case is relevant for a time-optimal path planning study, because it uses the level set reachability front to show where a vehicle can travel to within each day. Since this field contains many land masses (islands), this shows the interaction of velocity flow-fields and unnavigable areas (land) in determining the optimal path.

The arrival time field mission case has been used before in past MSEAS research. The minimum arrival time, or "first arrival time", was computed for a field of underwater gliders operating through landmasses in complex and realistic ocean flow-fields in the Sulu Archipelago in the Philippines [67]. These landmasses were treated as obstacles that will block vehicles and currents when computing the minimum arrival times for a vehicle travelling through the Sulu Archipelago [61]. The minimum arrival time calculations yields time-to-reach maps, that show the reachable set of points that can be travelled to within each time amount, and avoiding hitting obstacles that could result in catastrophic failure [21],

Possible applications for this case would be scientific studies, security, communication, monitoring, or any application where a vehicle is released in an area with many land masses, and the user would need to know where the AUV can travel to in a set amount of time. For example, if an AUV is released that has a 24-hour power supply, this would predict where it could travel to in that time set before it needed to be retrieved and recharged.

We predicted minimum arrival times for all surface points in the Azores island region, as illustrated in Figure 5-35 below that shows the arrival time field for a

vehicle starting offshore of the São Miguel Island and travelling at 0.5 m/s.

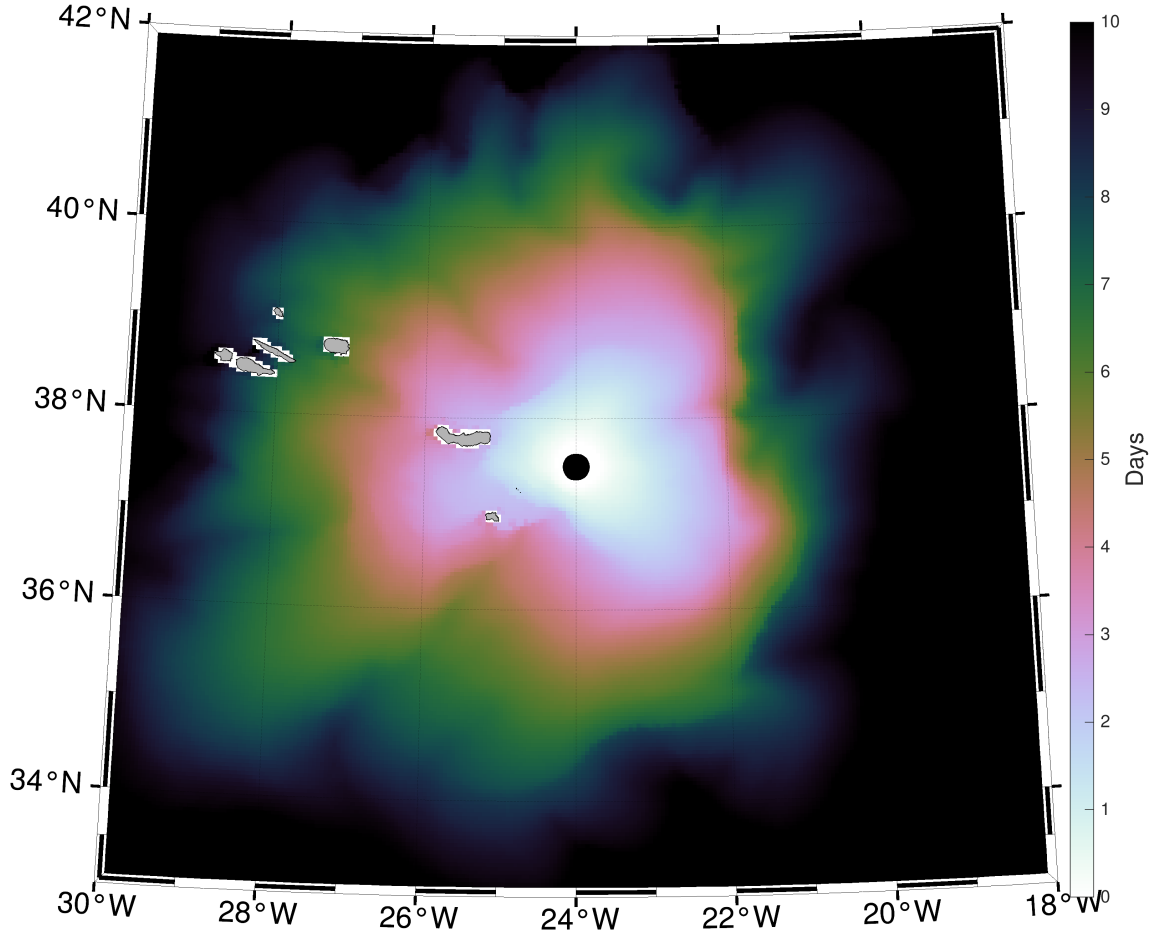

Figure 5-35: All reachable points within time gradient from 0 to 10 days, for a vehicle travelling at 0.5 m/s from São Miguel Island. The plot background is reachable area, measured in days.

The results from this figure confirm that several locations have strong gradients in the arrival time fields, indicating that there are multiple paths to arrive in very similar locations but with very different times. Overall, this arrival time field shows how optimal times and paths are modified by currents, land masses (i.e. islands which can be avoided in two ways), and tides and currents near islands.

In Figure 5-36 below, there are four pairs of points, all of which are reached at the same time. Two of them are near the high gradient diverging contour and two pairs are near the converging part of the front. The minimum-time paths are set against the minimal arrival time gradient, showing that each of these paths will take the same

amount of time

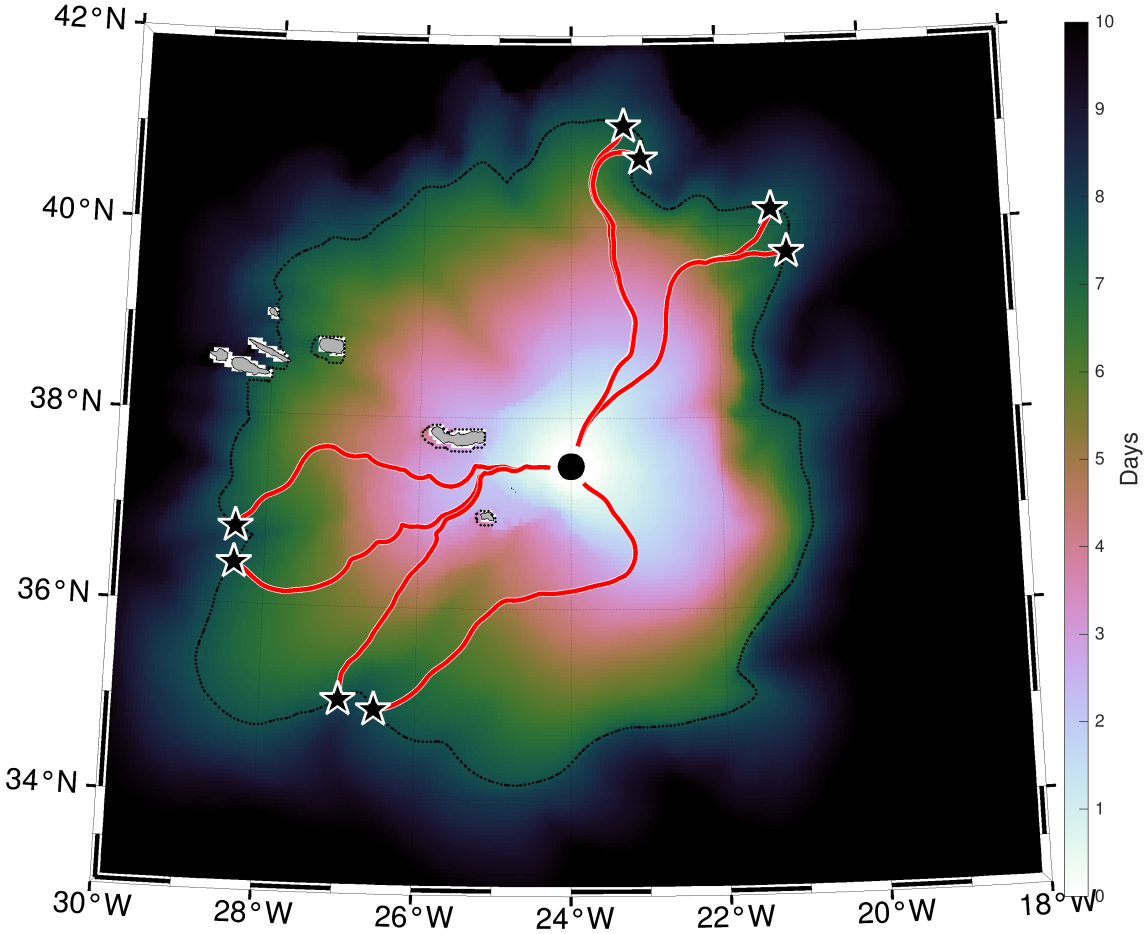

Figure 5-36: Final time-optimal paths to similar points for vehicles travelling at 0.5 m/s from São Miguel Island. The plot background is reachable area, measured in days.

As illustrated in the figure, the two path pairs that travel north will have very similar paths, and the two path pairs that travel south have very different paths. These diverging characteristics are created due to land masses in the way, as well as opposing currents. This shows that nearby points can have significantly different or similar optimal paths, depending on local characteristics and discontinuities of the time-to-reach fields, such as locally convex vs. concave reachability front.

Since each of these landmasses contain points where the vehicle cannot travel, as they are ocean vehicles and not hybrid land vehicles, these are not included in the reachable set of points. Therefore, the reachability front will wrap *around* these islands [61]. Within the level set, the amount of discontinuities will be proportional

to the amount of landmasses. This will split the reachability front, and there will be at least two optimal routes with the same arrival time through the discontinuity point. This results in several time-optimal paths between islands [71].

Chapter 6

Conclusion and Future work

In this final chapter, we summarize the contributions and key results of this thesis. We then discuss further applications for future work.

The main contribution in this thesis was a study of the sensitivity of time-optimal path planning in the Portugal ocean region that encompassed the Azores islands, Madeira, and a large section of the North Atlantic off of the Iberian coast. We utilized the MIT-MSEAS exact PDE-based planning theory and level set methods to optimize the path of ocean vehicles in the Portuguese ocean region. Such optimization yields cost savings, longer operational time, and environmental protection. It allows longer-range missions and endurance operations throughout the extensive Portuguese ocean region, within given time, range, and power budgets.

In this study, we reviewed the local ocean circulation and oceanography in the region, and the MSEAS ocean modeling and data assimilation system used. In addition to the ocean dynamics, this work also discussed the many applications of autonomous marine vehicles in the Portuguese region, with some of their past uses as well as potential future applications. We then described our implementation and validation of the multi-resolution 4D ocean modeling and forecasting in the region. We discussed the application of the MSEAS exact PDE-based planning theory and schemes, and data-driven ocean modeling methodology to create time-optimal paths between start and end points in five major locations in the region. We utilized this theory and methodology for surface and bottom autonomous vehicles, and compared

results based on vehicle speed, travel direction, and start time. We delineated effects of the dynamic ocean currents on the AUV's navigation for different vehicle journeys, including the sensitivity to different point-to-point travels, multiple start points and a common end point, and multiple end points and a common start point. We also compared these paths to the direct, zero-flow paths. We illustrated more complex path planning applications, including the fastest interception courses between two vehicles, as well as computing minimum arrival times for all surface points in a dynamic flow field containing islands in the Azores archipelago. Overall, our studies showcased many applications of path planning in the Portuguese ocean region. Our results were aligned with the goals of the MIT Portugal project, which supported this work, in their research area of "Earth Systems: Oceans to Near Space" [72].

Our work provides many opportunities for future work. First, the application of real-time sea trials with autonomous underwater vehicles deployed in this region would give concrete feedback on the application and capabilities of these methods in this region. Real-time sea trials such as this have then used in past MIT-MSEAS research, such as with the REMUS 600 AUVs in the Buzzards Bay and Vineyard Sound regions [97]. Second, a study of varying the input AUV speed during its path would allow for conserving energy. This is because the vehicle could reduce its speed as favorable currents propelled it towards its destination, or increase its speed if adverse currents impeded its travel or caused it to remain stationary. Such theory and schemes have been developed by the MSEAS group in past studies [53, 96, 95, 22], including accounting for uncertainties in the ocean forecasts and minimizing risks [53, 98, 99].

In conclusion, this thesis has simulated many possible applications of time-optimal path planning and control integrated with ocean modeling in the Portuguese ocean region. As AUVs use is becoming prevalent in scientific, commercial, and security applications, such quantitative path planning sensitivity studies are critical to increase efficiency and reduce risks for future ocean autonomy applications.

Bibliography

[1] A. Agarwal and P. F. J. Lermusiaux. Statistical field estimation for complex coastal regions and archipelagos. *Ocean Modelling*, 40(2):164–189, 2011.

[2] Alberto Alvarez, Andrea Caiti, and Reiner Onken. Evolutionary path planning for autonomous underwater vehicles in a variable ocean. *IEEE Journal of Oceanic Engineering*, 29(2):418–429, 2004.

[3] Alexander Bahr, John J Leonard, and Maurice F Fallon. Cooperative localization for autonomous underwater vehicles. *The International Journal of Robotics Research*, 28(6):714–728, 2009.

[4] E.D. Barton. Canary And Portugal Currents. In *Encyclopedia of Ocean Sciences*, pages 380–389. Elsevier, 2001.

[5] Ş. T. Beşiktepe, P. F. J. Lermusiaux, and A. R. Robinson. Coupled physical and biogeochemical data-driven simulations of Massachusetts Bay in late summer: Real-time and post-cruise data assimilation. *Journal of Marine Systems*, 40–41:171–212, 2003.

[6] J.H. Bettencourt and C. Guedes Soares. Surface circulation in the Eastern Central North Atlantic. In *Developments in Maritime Technology and Engineering*, pages 785–790. CRC Press, London, 1 edition, July 2021.

[7] Manmeet S. Bhabra, Manan Doshi, Benjamin C. Koenig, Patrick J. Haley, Jr., C. Mirabito, Pierre F. J. Lermusiaux, C. A. Goudey, J. Curcio, D. Manganelli, and H. Goudey. Optimal harvesting with autonomous tow vessels for offshore macroalgae farming. In *OCEANS 2020 IEEE/MTS*, pages 1–10. IEEE, October 2020.

[8] Manmeet Singh Bhabra. Harvest-time optimal path planning in dynamic flows. Master's thesis, Massachusetts Institute of Technology, Department of Mechanical Engineering and Computational Science & Engineering, Cambridge, Massachusetts, September 2021.

[9] Barbie Bischof, Arthur J. Mariano, and Edward H. Ryan. The Portugal current system, May 2022.

[10] Rui M. A. Caldeira and Jesus C. Reis. The Azores Confluence Zone. *Frontiers in Marine Science*, 4, February 2017.

[11] John Canny. *The complexity of robot motion planning*. Number 1987 in ACM doctoral dissertation awards. MIT Press, Cambridge, Mass, 1988.

[12] David Caress, Hans Thomas, William Kirkwood, Rob McEwen, Richard Henthorn, David Clague, C. Paull, Jennifer Paduan, and Katherine Maier. High-resolution multibeam, sidescan, and subbottom surveys using the MBARI AUV D. Allan B. *Marine Habitat Mapping Technology for Alaska*, January 2008.

[13] H.S Coelho, R.J.J Neves, M White, P.C Leitão, and A.J Santos. A model for ocean circulation on the Iberian coast. *Journal of Marine Systems*, 32(1-3):153–179, April 2002.

[14] M. E. G. D. Colin, T. F. Duda, L. A. te Raa, T. van Zon, P. J. Haley, Jr., P. F. J. Lermusiaux, W. G. Leslie, C. Mirabito, F. P. A. Lam, A. E. Newhall, Y.-T. Lin, and J. F. Lynch. Time-evolving acoustic propagation modeling in a complex ocean environment. In *OCEANS - Bergen, 2013 MTS/IEEE*, pages 1–9, 2013.

[15] Nuno A. Cruz and Anibal C. Matos. The MARES AUV, a Modular Autonomous Robot for Environment Sampling. In *OCEANS 2008*, pages 1–6, September 2008. ISSN: 0197-7385.

[16] James A. Cummings and Ole Martin Smedstad. *Variational Data Assimilation for the Global Ocean*, pages 303–343. Springer Berlin Heidelberg, Berlin, Heidelberg, 2013.

[17] Benoit Cushman-Roisin and Jean-Marie Beckers. *Introduction to Geophysical Fluid Dynamics - Physical and Numerical Aspects*, volume 101 of *International Geophysics*. Elsevier, 2011.

[18] Russ E. Davis, Naomi E. Leonard, and David M. Fratantoni. Routing strategies for underwater gliders. *Deep Sea Research Part II: Topical Studies in Oceanography*, 56(3-5):173–187, February 2009.

[19] J Borges de Sousa and G Gonçalves. Mixed Initiative Control of Unmanned Air and Ocean Going Vehicles: Models, Tools and Experimentation. In *Proceeding of RTO AVT-146 Symposium Platform Innovations and System Integration for Unmanned Air, Land and Sea Vehicles*, volume 9, pages 1–14, Florence, 2007.

[20] Manan Doshi. Energy-time optimal path planning in strong dynamic flows. Master's thesis, Massachusetts Institute of Technology, Center for Computational Science and Engineering, Cambridge, Massachusetts, February 2021.

[21] Manan Doshi, Manmeet Bhabra, Marius Wiggert, Claire J. Tomlin, and Pierre F. J. Lermusiaux. Hamilton–Jacobi multi-time reachability. In *IEEE CDC 2022 Cancún*, pages 1–8, December 2022. Sub-judice.

[22] Manan M. Doshi, Manmeet S. Bhabra, and Pierre F. J. Lermusiaux. Energy-time optimal path planning in dynamic flows: Theory and schemes. *Computer Methods in Applied Mechanics and Engineering*, 2022. Sub-judice.

[23] J. Edwards, J. Smith, A. Girard, D. Wickman, D. N. Subramani, C. S. Kulkarni, P. J. Haley, Jr., C. Mirabito, S. Jana, and P. F. J. Lermusiaux. Data-driven learning and modeling of AUV operational characteristics for optimal path planning. In *Oceans '17 MTS/IEEE Conference*, Aberdeen, June 2017.

[24] Gary D. Egbert and Svetlana Y. Erofeeva. Efficient inverse modeling of barotropic ocean tides. *Journal of Atmospheric and Oceanic Technology*, 19(2):183–204, 2002.

[25] Maurizio Falcone, La Sapienza, and Hasnaa Zidani. Numerical method for HJB equations. Optimal control problems and differential games (lecture 3/3). Lecture slides, 2012.

[26] Avijit Gangopadhyay, Pierre F.J. Lermusiaux, Leslie Rosenfeld, Allan R. Robinson, Leandro Calado, Hyun Sook Kim, Wayne G. Leslie, and Patrick J. Haley, Jr. The California Current system: A multiscale overview and the development of a feature-oriented regional modeling system (FORMS). *Dynamics of Atmospheres and Oceans*, 52(1–2):131–169, September 2011. Special issue of Dynamics of Atmospheres and Oceans in honor of Prof. A. R. Robinson.

[27] Abhinav Gupta, Patrick J. Haley, Deepak N. Subramani, and Pierre F. J. Lermusiaux. Fish modeling and Bayesian learning for the Lakshadweep Islands. In *OCEANS 2019 MTS/IEEE SEATTLE*, pages 1–10, Seattle, October 2019. IEEE.

[28] P. J. Haley, Jr., A. Agarwal, and P. F. J. Lermusiaux. Optimizing velocities and transports for complex coastal regions and archipelagos. *Ocean Modeling*, 89:1–28, 2015.

[29] P. J. Haley, Jr., P. F. J. Lermusiaux, A. R. Robinson, W. G. Leslie, O. Logoutov, G. Cossarini, X. S. Liang, P. Moreno, S. R. Ramp, J. D. Doyle, J. Bellingham, F. Chavez, and S. Johnston. Forecasting and reanalysis in the Monterey Bay/California Current region for the Autonomous Ocean Sampling Network-II experiment. *Deep Sea Research Part II: Topical Studies in Oceanography*, 56(3–5):127–148, February 2009.

[30] Patrick J. Haley, Jr. and Pierre F. J. Lermusiaux. Multiscale two-way embedding schemes for free-surface primitive equations in the "Multidisciplinary Simulation, Estimation and Assimilation System". *Ocean Dynamics*, 60(6):1497–1537, December 2010.

[31] Patrick J. Haley, Jr. and Pierre F. J. Lermusiaux. Limiters for Shapiro filtering with primitive-equation ocean models. MSEAS Report, Department of Mechanical Engineering, Massachusetts Institute of Technology, Cambridge, MA, 2016.

[32] Woods Hole Oceanographic Institute. REMUS 600 – Oceanographic Systems Lab.

[33] Josep Isern, Daniel Hernández-Sosa, Enrique Fernández Perdomo, Jorge Cabrera, Antonio Domínguez Brito, and Prieto-Marañón Víctor. Obstacle avoidance in underwater glider path planning. *Journal of Physical Agents*, 6:11–20, 01 2012.

[34] Eirik Keilegavlen and Jarle Berntsen. Non-hydrostatic pressure in σ-coordinate ocean models. *Ocean Modelling*, 28(4):240–249, 2009.

[35] Sven Koenig, Craig Tovey, and Yuri Smirnov. Performance bounds for planning in unknown terrain. *Artificial Intelligence*, 147(1-2):253–279, 2003.

[36] C. S. Kulkarni, P. J. Haley, Jr., P. F. J. Lermusiaux, A. Dutt, A. Gupta, C. Mirabito, D. N. Subramani, S. Jana, W. H. Ali, T. Peacock, C. M. Royo, A. Rzeznik, and R. Supekar. Real-time sediment plume modeling in the Southern California Bight. In *OCEANS Conference 2018*, Charleston, SC, October 2018. IEEE.

[37] Chinmay S. Kulkarni and Pierre F. J. Lermusiaux. Advection without compounding errors through flow map composition. *Journal of Computational Physics*, 398:108859, December 2019.

[38] Chinmay S. Kulkarni and Pierre F. J. Lermusiaux. Three-dimensional time-optimal path planning in the ocean. *Ocean Modelling*, 152, August 2020.

[39] Jean-Claude Latombe. *Robot motion planning*. Number SECS 124 in The Kluwer international series in engineering and computer science ; Robotics. Kluwer Academic Publishers, Boston, 1991.

[40] Steven M LaValle. *Planning algorithms*. Cambridge university press, 2006.

[41] Steven M. Lavalle et al. Rapidly-exploring random trees: A new tool for path planning. Technical report, Iowa State University, 1998.

[42] Phillip J. LeBas. *Maximizing AUV slow speed performance*. Massachusetts Institute of Technology and Woods Hole Oceanographic Institution, Woods Hole, MA, 1997.

[43] N.E. Leonard and E. Fiorelli. Virtual leaders, artificial potentials and coordinated control of groups. In *Proceedings of the 40th IEEE Conference on Decision and Control (Cat. No.01CH37228)*, volume 3, pages 2968–2973, Orlando, FL, USA, 2001. IEEE.

[44] P. F. J. Lermusiaux. Data assimilation via Error Subspace Statistical Estimation, part II: Mid-Atlantic Bight shelfbreak front simulations, and ESSE validation. *Monthly Weather Review*, 127(7):1408–1432, July 1999.

[45] P. F. J. Lermusiaux. Estimation and study of mesoscale variability in the Strait of Sicily. *Dynamics of Atmospheres and Oceans*, 29(2):255–303, 1999.

[46] P. F. J. Lermusiaux. Evolving the subspace of the three-dimensional multiscale ocean variability: Massachusetts Bay. *Journal of Marine Systems*, 29(1):385–422, 2001.

[47] P. F. J Lermusiaux. Adaptive modeling, adaptive data assimilation and adaptive sampling. *Physica D: Nonlinear Phenomena*, 230(1):172–196, 2007.

[48] P. F. J. Lermusiaux and C.-S. Chiu. Four-dimensional data assimilation for coupled physical-acoustical fields. In N. G. Pace and F. B. Jensen, editors, *Acoustic Variability, 2002*, pages 417–424, Saclantcen, 2002. Kluwer Academic Press.

[49] P. F. J. Lermusiaux, C.-S. Chiu, and A. R. Robinson. Modeling uncertainties in the prediction of the acoustic wavefield in a shelfbreak environment. In E.-C. Shang, Q. Li, and T. F. Gao, editors, *Proceedings of the 5th International conference on theoretical and computational acoustics*, pages 191–200. World Scientific Publishing Co., May 21-25 2002. Refereed invited manuscript.

[50] P. F. J. Lermusiaux, P. J. Haley, W. G. Leslie, A. Agarwal, O. Logutov, and L. J. Burton. Multiscale physical and biological dynamics in the Philippine Archipelago: Predictions and processes. *Oceanography*, 24(1):70–89, 2011. Special Issue on the Philippine Straits Dynamics Experiment.

[51] P. F. J. Lermusiaux, P. J. Haley, Jr., S. Jana, A. Gupta, C. S. Kulkarni, C. Mirabito, W. H. Ali, D. N. Subramani, A. Dutt, J. Lin, A. Shcherbina, C. Lee, and A. Gangopadhyay. Optimal planning and sampling predictions for autonomous and Lagrangian platforms and sensors in the northern Arabian Sea. *Oceanography*, 30(2):172–185, June 2017. Special issue on Autonomous and Lagrangian Platforms and Sensors (ALPS).

[52] P. F. J Lermusiaux, P. J. Haley, Jr, and N. K. Yilmaz. Environmental prediction, path planning and adaptive sampling: sensing and modeling for efficient ocean monitoring, management and pollution control. *Sea Technology*, 48(9):35–38, 2007.

[53] P. F. J. Lermusiaux, T. Lolla, P. J. Haley, Jr., K. Yigit, M. P. Ueckermann, T. Sondergaard, and W. G. Leslie. Science of autonomy: Time-optimal path planning and adaptive sampling for swarms of ocean vehicles. In Tom Curtin, editor, *Springer Handbook of Ocean Engineering: Autonomous Ocean Vehicles, Subsystems and Control*, chapter 21, pages 481–498. Springer, 2016.

[54] P. F. J. Lermusiaux, D. N. Subramani, J. Lin, C. S. Kulkarni, A. Gupta, A. Dutt, T. Lolla, P. J. Haley, Jr., W. H. Ali, C. Mirabito, and S. Jana. A future for intelligent autonomous ocean observing systems. *Journal of Marine*

Research, 75(6):765–813, November 2017. The Sea. Volume 17, The Science of Ocean Prediction, Part 2.

[55] Pierre F. J. Lermusiaux, Matt P. Ueckermann, C. Mirabito, Patrick J. Haley, Jr., and J. Aoussou. High Order Hybridizable Discontinuous Galerkin Projection Schemes for Incompressible Navier-Stokes and Ocean Primitive Equations: Derivation Details. MSEAS Report 22, Department of Mechanical Engineering, Massachusetts Institute of Technology, Cambridge, Massachusetts, USA, August 2014.

[56] W. G. Leslie, A. R. Robinson, P. J. Haley, Jr, O. Logutov, P. A. Moreno, P. F. J. Lermusiaux, and E. Coelho. Verification and training of real-time forecasting of multi-scale ocean dynamics for maritime rapid environmental assessment. *Journal of Marine Systems*, 69(1):3–16, 2008.

[57] O. G. Logutov and P. F. J. Lermusiaux. Inverse barotropic tidal estimation for regional ocean applications. *Ocean Modelling*, 25(1–2):17–34, 2008.

[58] Sri Venkata Tapovan Lolla. Path planning in time dependent flows using level set methods. Master's thesis, Massachusetts Institute of Technology, Department of Mechanical Engineering, Cambridge, Massachusetts, September 2012.

[59] Sri Venkata Tapovan Lolla. *Path Planning and Adaptive Sampling in the Coastal Ocean*. PhD thesis, Massachusetts Institute of Technology, Department of Mechanical Engineering, Cambridge, Massachusetts, February 2016.

[60] T. Lolla, P. J. Haley, Jr., and P. F. J. Lermusiaux. Time-optimal path planning in dynamic flows using level set equations: Realistic applications. *Ocean Dynamics*, 64(10):1399–1417, 2014.

[61] T. Lolla, P. J. Haley, Jr., and P. F. J. Lermusiaux. Path planning in multiscale ocean flows: Coordination and dynamic obstacles. *Ocean Modelling*, 94:46–66, 2015.

[62] T. Lolla and P. F. J. Lermusiaux. A Gaussian mixture model smoother for continuous nonlinear stochastic dynamical systems: Applications. *Monthly Weather Review*, 145:2763–2790, July 2017.

[63] T. Lolla and P. F. J. Lermusiaux. A Gaussian mixture model smoother for continuous nonlinear stochastic dynamical systems: Theory and scheme. *Monthly Weather Review*, 145:2743–2761, July 2017.

[64] T. Lolla and P. F. J. Lermusiaux. A forward reachability equation for minimum-time path planning in strong dynamic flows. *SIAM Journal on Control and Optimization*, 2020. Sub-judice.

[65] T. Lolla, P. F. J. Lermusiaux, M. P. Ueckermann, and P. J. Haley, Jr. Modified level set approaches for the planning of time-optimal paths for swarms

of ocean vehicles. MSEAS Report 15, Department of Mechanical Engineering, Massachusetts Institute of Technology, Cambridge, MA, USA, 2014.

[66] T. Lolla, P. F. J. Lermusiaux, M. P. Ueckermann, and P. J. Haley, Jr. Time-optimal path planning in dynamic flows using level set equations: Theory and schemes. *Ocean Dynamics*, 64(10):1373–1397, 2014.

[67] T. Lolla and Pierre F. J. Lermusiaux. A forward reachability equation for minimum-time path planning in strong dynamic flows. MSEAS Report 27, Department of Mechanical Engineering, Massachusetts Institute of Technology, Cambridge, MA, USA, 2017.

[68] Tapovan Lolla, Mattheus P. Ueckermann, Konur Yiğit, Patrick J. Haley, Jr., and Pierre F. J. Lermusiaux. Path planning in time dependent flow fields using level set methods. In *IEEE International Conference on Robotics and Automation (ICRA), 14-18 May 2012*, pages 166–173, 2012.

[69] Gianandrea Mannarini, Deepak N. Subramani, Pierre F. J. Lermusiaux, and Nadia Pinardi. Graph-search and differential equations for time-optimal vessel route planning in dynamic ocean waves. *IEEE Transactions on Intelligent Transportation Systems*, 21(6):1–13, June 2020.

[70] C. Sena Martins, M. Hamann, and A. F. G. Fiúza. Surface circulation in the eastern North Atlantic, from drifters and altimetry: SURFACE CIRCULATION ON THE EASTERN NORTH ATLANTIC. *Journal of Geophysical Research: Oceans*, 107(C12):10–1–10–22, December 2002.

[71] C. Mirabito, D. N. Subramani, T. Lolla, P. J. Haley, Jr., A. Jain, P. F. J. Lermusiaux, C. Li, D. K. P. Yue, Y. Liu, F. S. Hover, N. Pulsone, J. Edwards, K. E. Railey, and G. Shaw. Autonomy for surface ship interception. In *Oceans '17 MTS/IEEE Conference*, Aberdeen, June 2017.

[72] MIT Portugal Program. Earth Systems: Oceans to Near Space – MIT Portugal.

[73] Monterey Bay Aquarium Research Institute (MBARI). Seafloor mapping AUV, December 2015.

[74] MSEAS Group. Intelligent observing and multiscale modeling for ocean exploration and sustainable utilization, 2022. MIT Portugal Partnership (MPP2030) Research Seed Fund Program.

[75] National Centers for Environmental Prediction (NCEP). North American Mesoscale Forecast System (NAM), September 2019.

[76] Navionics. Navionics chartviewer, May 2022.

[77] Reiner Onken, Alberto Álvarez, Vicente Fernández, Guillermo Vizoso, Gotzon Basterretxea, Joaquín Tintoré, Patrick Haley, Jr., and Elvio Nacini. A forecast experiment in the Balearic Sea. *Journal of Marine Systems*, 71(1-2):79–98, 2008.

[78] D.A. Paley, F. Zhang, and N.E. Leonard. Cooperative Control for Ocean Sampling: The Glider Coordinated Control System. *IEEE Transactions on Control Systems Technology*, 16(4):735–744, July 2008.

[79] Yulin Pan, Patrick J. Haley, Jr., and Pierre F. J. Lermusiaux. Interactions of internal tides with a heterogeneous and rotational ocean. *Journal of Fluid Mechanics*, 920:A18, August 2021.

[80] Madhusmita Panda, Bikramaditya Das, Bidyadhar Subudhi, and Bibhuti Bhusan Pati. A comprehensive review of path planning algorithms for autonomous underwater vehicles. *International Journal of Automation and Computing*, 17(3):321–352, 2020.

[81] Álvaro Peliz, Jesús Dubert, A. Miguel P. Santos, Paulo B. Oliveira, and Bernard Le Cann. Winter upper ocean circulation in the Western Iberian Basin—Fronts, Eddies and Poleward Flows: an overview. *Deep Sea Research Part I: Oceanographic Research Papers*, 52(4):621–646, April 2005.

[82] Roland Philippsen and Roland Siegwart. An interpolated dynamic navigation function. In *Proceedings of the 2005 IEEE International Conference on Robotics and Automation*, pages 3782–3789. IEEE, 2005.

[83] Kanna Rajan, Fernando Aguado, Pierre Lermusiaux, João Borges de Sousa, Ajit Subramaniam, and Joaquin Tintore. METEOR: A Mobile (portable) ocEan roboTic obsErvatORy. *Marine Technology Society Journal*, 55(3):74–75, May 2021.

[84] P. Ramos, N. Cruz, A. Matos, M.V. Neves, and F.L. Pereira. Monitoring an ocean outfall using an AUV. In *MTS/IEEE Oceans 2001. An Ocean Odyssey. Conference Proceedings (IEEE Cat. No.01CH37295)*, volume 3, pages 2009–2014, Honolulu, HI, USA, 2001. Marine Technol. Soc.

[85] Steven R. Ramp, Pierre F. J. Lermusiaux, Igor Shulman, Yi Chao, Rebecca E. Wolf, and Frederick L. Bahr. Oceanographic and atmospheric conditions on the continental shelf north of the Monterey Bay during August 2006. *Dynamics of Atmospheres and Oceans*, 52(1–2):192–223, September 2011. Special issue of Dynamics of Atmospheres and Oceans in honor of Prof. A. R. Robinson.

[86] Dushyant Rao and Stefan B Williams. Large-scale path planning for underwater gliders in ocean currents. In *Australasian conference on robotics and automation (ACRA)*, pages 2–4. Citeseer, 2009.

[87] Blane Rhoads, Igor Mezić, and Andrew C Poje. Minimum time heading control of underpowered vehicles in time-varying ocean currents. *Ocean Engineering*, 66:12–31, 2013.

[88] A. R. Robinson and P. F. J. Lermusiaux. Data assimilation (physical/interdisciplinary). In J. H. Steele, S. Thorpe, and K. Turekian, editors, *Encyclopedia of Ocean Sciences*, pages 302–308. Academic Press, London, 2001.

[89] A. R. Robinson and P. F. J. Lermusiaux. Prediction systems with data assimilation for coupled ocean science and ocean acoustics. In A. Tolstoy et al, editor, *Proceedings of the Sixth International Conference on Theoretical and Computational Acoustics*, pages 325–342. World Scientific Publishing, 2004. Refereed invited Keynote Manuscript.

[90] A. R. Robinson, P. F. J. Lermusiaux, and N. Q. Sloan III. Data assimilation. In Kenneth H. Brink and Allan R. Robinson, editors, *The Global Coastal Ocean-Processes and Methods*, volume 10 of *The Sea*, chapter 20, pages 541–594. John Wiley and Sons, New York, 1998.

[91] Allan R. Robinson and Pierre F. J. Lermusiaux. Data assimilation for modeling and predicting coupled physical–biological interactions in the sea. In Allan R. Robinson, James J. McCarthy, and Brian J. Rothschild, editors, *Biological-Physical Interactions in the Sea*, volume 12 of *The Sea*, chapter 12, pages 475–536. John Wiley and Sons, New York, 2002.

[92] T. Sondergaard and P. F. J. Lermusiaux. Data assimilation with Gaussian Mixture Models using the Dynamically Orthogonal field equations. Part I: Theory and scheme. *Monthly Weather Review*, 141(6):1737–1760, 2013.

[93] T. Sondergaard and P. F. J. Lermusiaux. Data assimilation with Gaussian Mixture Models using the Dynamically Orthogonal field equations. Part II: Applications. *Monthly Weather Review*, 141(6):1761–1785, 2013.

[94] Anthony Stentz. Optimal and efficient path planning for partially known environments. In *Intelligent unmanned ground vehicles*, pages 203–220. Springer, 1997.

[95] D. N. Subramani, P. J. Haley, Jr., and P. F. J. Lermusiaux. Energy-optimal path planning in the coastal ocean. *Journal of Geophysical Research: Oceans*, 122:3981–4003, 2017.

[96] D. N. Subramani and P. F. J. Lermusiaux. Energy-optimal path planning by stochastic dynamically orthogonal level-set optimization. *Ocean Modeling*, 100:57–77, 2016.

[97] D. N. Subramani, P. F. J. Lermusiaux, P. J. Haley, Jr., C. Mirabito, S. Jana, C. S. Kulkarni, A. Girard, D. Wickman, J. Edwards, and J. Smith. Time-optimal path planning: Real-time sea exercises. In *Oceans '17 MTS/IEEE Conference*, Aberdeen, June 2017.

[98] D. N. Subramani, Q. J. Wei, and P. F. J. Lermusiaux. Stochastic time-optimal path-planning in uncertain, strong, and dynamic flows. *Computer Methods in Applied Mechanics and Engineering*, 333:218–237, 2018.

[99] Deepak N. Subramani and Pierre F. J. Lermusiaux. Risk-optimal path planning in stochastic dynamic environments. *Computer Methods in Applied Mechanics and Engineering*, 353:391–415, August 2019.

[100] W. Sun, P. Tsiotras, T. Lolla, D. N. Subramani, and P. F. J. Lermusiaux. Pursuit-evasion games in dynamic flow fields via reachability set analysis. In *2017 American Control Conference (ACC)*, pages 4595–4600, Seattle, 2017.

[101] Wei Sun, Panagiotis Tsiotras, Tapovan Lolla, Deepak N. Subramani, and Pierre F. J. Lermusiaux. Multiple-pursuer-one-evader pursuit evasion game in dynamic flow fields. *Journal of Guidance, Control and Dynamics*, 40(7), April 2017.

[102] Chiew Seon Tan, Robert Sutton, and John Chudley. Quasi-random, manoeuvre-based motion planning algorithm for autonomous underwater vehicles. *IFAC Proceedings Volumes*, 38(1):103–108, 2005.

[103] M. P. Ueckermann and P. F. J. Lermusiaux. 2.29 Finite Volume MATLAB Framework Documentation. MSEAS Report 14, Department of Mechanical Engineering, Massachusetts Institute of Technology, Cambridge, MA, 2012.

[104] M. P. Ueckermann and P. F. J. Lermusiaux. Hybridizable discontinuous Galerkin projection methods for Navier–Stokes and Boussinesq equations. *Journal of Computational Physics*, 306:390–421, 2016.

[105] Jonas Witt and Matthew Dunbabin. Go with the flow: Optimal auv path planning in coastal environments. *Proceedings of the ACRA 2008*, 01 2008.

[106] Weizhong Zhang, Tamer Inanc, Sina Ober-Blobaum, and Jerrold E Marsden. Optimal trajectory generation for a glider in time-varying 2D ocean flows B-spline model. In *2008 IEEE International Conference on Robotics and Automation*, pages 1083–1088. IEEE, 2008.